Interaction of equatorially trapped waves and a background shear: Numerical and theoretical issues

by

Maryam Namazi
B.Sc., University of Isfahan, 2003
M.Sc., University of Tehran, 2005

A Dissertation Submitted in Partial Fulfillment of the
Requirements for the Degree of

DOCTOR OF PHILOSOPHY

in the Department of Mathematics and Statistics

Interaction of equatorially trapped waves and a background shear: Numerical and theoretical issues

by

Maryam Namazi
B.Sc., University of Isfahan, 2003
M.Sc., University of Tehran, 2005

Supervisory Committee

Dr. B. Khouider, Supervisor
(Department of Mathematics and Statistics)

Dr. M. Agueh, Departmental Member
(Department of Mathematics and Statisticse)

Dr. A. Quas, Departmental Member
(Department of Mathematics and Statistics)

Dr. A. Monahan, Outside Member
(Department of Earth and Ocean Science)

Supervisory Committee

Dr. B. Khouider, Supervisor
(Department of Mathematics and Statistics)

Dr. M. Agueh, Departmental Member
(Department of Mathematics and Statisticse)

Dr. A. Quas, Departmental Member
(Department of Mathematics and Statistics)

Dr. A. Monahan, Outside Member
(Department of Earth and Ocean Science)

ABSTRACT

The equatorial atmosphere harbours a large spectrum of waves that are trapped near and travel along the equator. These equatorially trapped waves interact non-linearly with each other, with the extra-tropics and with the planetary-barotropic waves. Here, we consider advected shallow water equations that represent interactions of these equatorial waves, associated with the first baroclinic mode, with prescribed meridional-barotropic shears. We present three well-known numerical schemes for handling this system and discuss the risk of applying them crudely to equatorial waves. We study the properties of these waves, such as their phase speed and their trapping around the equator, using two approaches: linear analysis and the time evolutions of the system derived by meridional projection of the barotropic-first baroclinic system. We show that in the sheared environment the symmetric (anti-symmetric) equatorial waves excite other symmetric (anti-symmetric) equatorial waves of the same wavenumber and of different strengths.

Contents

List of Tables

List of Figures

ACKNOWLEDGEMENTS

I would like to thank my supervisor, Dr. Boualem Khouider, for his support, encouragement, patience and guidance he provided throughout my PhD studies. He was actively involved in the work. From him, I have broadened my perspective about applied mathematics and developed my understanding of science. I thank Drs. George Kiladis and Adam Monahan for their constructive and helpful comments, providing precious advices and their helpful insight for this dissertation. I would also like to thank my great friends Angus Argyle, Fatemeh Eslami, Kseniya Garaschuk, Ying Han, Reinel Sospedra and Mike Waite for their support and encouragement. I owe my deepest gratitude to my family for their support throughout my life and work. Finally, I am heartily grateful of my wonderful husband, Mohammad Amin, whose love and support carried me through the roughest times.

Chapter 1

Introduction

Most of the Earth's energy intake from the sun is absorbed within the tropical belt and then redistributed to the rest of the globe through various atmospheric and oceanic flow patterns. The organized deep convection is a major source of the energy for tropical circulations derived by latent heat associated with the phase change of water in the tropics. There is a strong interaction among cumulus convection and mesoscale and large-scale circulations; this interaction is of a primary importance for understanding tropical motion systems. Therefore, tropical dynamics has been a topic of interest for the past few decades because it is important for understanding the climate system and for improving climate and weather prediction models not only for the tropics but also for mid-latitudes. Tropical monsoons, Walker circulation, El Nino, tropical cyclones and the equatorial intra-seasonal oscillation known as the Madden-Julian oscillation (MJO) are just a few examples of the tropical phenomena that are known to affect the midlatitude weather and climate [9].

However, the general circulation models (GCM's), which are used to predict weather and climate, can not resolve some of these interactions and phenomena such as the MJO and the convectively coupled equatorial waves. These equatorial waves are trapped near the equator and travel along it and they interact nonlinearly with each other, with the extratropical waves and with the background flow. Therefore, it is necessary to develop simplified and idealized models to understand the interactions between these equatorial waves and the extra-tropics to capture the main features of their dynamics. However, there are no exact solutions to these nonlinear coupled complex partial differential equations (PDEs). So, climate modellers should borrow different numerical schemes, usually with conservation properties, of applied mathe-

matics to validate these models in terms of convergence and stability features.

There are various studies using theoretical analysis and/or observational evidence that the tropical dynamics is influenced by midlatitude activities and vice versa. A few examples of these studies are [40, 39, 43, 22] in which they essentially look at the effect of a shear on the equatorial waves. Webster and Holton in [40], considered a non-linear model based on Mercator coordinates to study the propagation of the equatorial waves across the equatorial region in the presence of zonally varying basic state zonal winds, $\bar{u}(x)$. These basic states were obtained through a specification of a mass source-sink which varies in longitude and latitude. It was shown in the westerly zonal winds, the waves with zonal scale smaller than the zonal scale of the basic state would propagate from one hemisphere to the other hemisphere. Webster and Chang in [39] addressed the impact of the zonally varying basic state on the equatorial energy accumulation and emanation regions, by improving the work in [40]. They provided evidence that a zonal stretching deformation of the basic flow of the tropics produces local convergence of energy to the east of the equatorial westerlies which nevertheless is a remote energy source for the extra-tropics.

The purpose of the study in [44] was to investigate the effect of the non-homogeneous mean zonal flow on equatorial perturbations when they are laterally forced. The authors developed a linear theory of a model similar to the shallow water equations [43] but with Rayleigh frictions and the Newtonian cooling. The properties of the equatorial waves such as their amplitudes and the propagation properties were discussed. The main results are that the westward phase speed of the Rossby waves are slower and that the Kelvin waves propagate eastward faster and the MRG waves change direction and move eastward. In addition, they showed that in mean westerlies, the Rossby waves and MRG waves are stronger than in the mean easterlies but, conversely, the Kelvin waves exhibit larger amplitude in mean easterlies than in the mean westerlies. Finally, in [22] simplified asymptotic equations were derived from the barotropic-first baroclinic interacting systems. The model included the non-linear energy exchange between barotropic Rossby waves and baroclinic equatorial Rossby waves through pure wave-wave coupling in the presence of horizontally and vertically sheared zonal mean flows. The linear theory was investigated for various combinations of the barotropic and the baroclinic zonal mean shear. However, they showed that the waves are never unstable. In addition, a non-linear interaction

was performed which justifies the transient exchange of energy between midlatitude barotropic Rossby waves and equatorial baroclinic Rossby waves.

It is shown in recent works, both in observational [41] and in theoretical [12, 13, 14, 15, 16] studies, that the convectively coupled equatorial waves are associated with the first baroclinic equatorial waves of Matsuno [24] but propagate at slower speed than that of their free counterparts obtained by linear theory. This is shown to be due to the moisture effects in the tropics [6, 12, 14]. In addition, there are also some differences in the structures of these equatorial waves with their free theoretical counterparts. In this dissertation, we study the interactions of the the equatorial waves in background shear environment. We are interested in the properties of the equatorial waves such as their phase speed, their trapping around the equator and possibly excitation of other equatorial waves by the waves in a shear background. One of the goals of this work is to find a plausible explanation for the non-zero meridional, south-north, velocity of the Kelvin waves seen in the observation. The theoretical Kelvin waves have no meridional velocity and we show in chapter 4 that in the imposed shear environment the shear-forced Kevin waves possess a weak but non-zero meridional velocity. We use the two mode model, representing the interactions between the barotropic (vertically averaged) mode and the first baroclinic mode, obtained by Galerkin projection of the non-hydrostatic beta-plane primitive equations [22].

In chapter 2, we present the derivation of the fully coupled barotropic-baroclinic model equations. We review the equatorially trapped waves obtained by linear shallow water equations and their properties. Then, we present the imposed barotropic shears: an equatorial easterly and an equatorial westerly wind mimicking the zonal wind in winter at 200 mb over the western Pacific ocean and eastern Pacific ocean, respectively [43].

In chapter 3, we present three numerical schemes to solve these advected shallow water equations: two types of finite volume schemes, the f-wave algorithm of Bale et al. [1] and the second order central scheme of Nessyahu and Tadmor [27] on non-staggered grids, and finally a Galerkin projection in the meridional direction introduced by Khouider and Majda [23]. In chapter 4, we introduce two new variables representing the geostrophic imbalance of the Kelvin waves and rewrite the advected shallow water equations in terms of these variables. This way, we highlight the effect

of a barotropic shear on the equatorial waves, especially Kelvin waves. By using any conservative method, the meridional geostrophic balance is truly preserved for the free Kelvin waves. Then, we present the poor performance of the central scheme. We give the reason for this great distortion of the structure of the Kelvin waves and equatorial waves, in general.

In chapter 5, we do a linear analysis of the meridionally projected system obtained by using parabolic cylinder functions as the basis functions. We assume wavelike solutions that travel along the equator in the zonal direction and compare the frequencies and the meridional structures of the shear-forced waves with their free analogues. In addition, we evolve this one dimensional advected system in time by using the second order central scheme to capture the dynamical interaction of the equatorial waves with the imposed barotropic shears. The shear-forced waves have the same frequencies and meridional structures as those obtained by the linear analysis. Furthermore, we demonstrate that each symmetric (anti-symmetric) equatorial wave excites other symmetric (anti-symmetric) equatorial waves with the same wavenumber. We mainly consider the two cases of the Kelvin and Rossby waves. We show that in the westerly shear the waves become unstable.

Finally in chapter 6, we propose the linear interaction between an imposed shear flow and an equatorial Rossby wave in the case of simple dry dynamics as a simple test case for climate models. This interaction develops a systematic turbulent-like cascade of energy toward small scales when integrated for a long enough time. We compare the performance of the f-wave algorithm and the Galerkin projection methods for this interaction and show that these numerical schemes handle this interaction differently.

Chapter 2

The governing equations

We consider the hydrostatic primitive equations on the equatorial β-plane using the Boussinesq approximation [21]:

$$\begin{aligned} \frac{D\mathbf{V}_H}{Dt} + \beta y \mathbf{V}_H^{\perp} + \nabla_H P &= S_v \\ \frac{\partial P}{\partial z} &= g\frac{\Theta}{\theta_0} \\ \frac{D\Theta}{Dt} + \frac{N^2\theta_0}{g} W &= S_\theta \\ \mathrm{div}_H \mathbf{V}_H + W_z &= 0 \end{aligned} \tag{2.1}$$

where $\mathbf{V}_H = (U(x,y,z,t), V(x,y,z,t))$ is the horizontal velocity with $\mathbf{V}_H^{\perp} = (-V, U)$, W is the vertical velocity, $P = P(x,y,z,t)$ is the rescaled pressure, pressure divided by the constant density ρ_0, and $\Theta(x,y,z,t)$ is the potential temperature. Here, $\mathbf{V}, P$ and Θ represent the deviation of these variables from a steady state mean background. S_v and S_θ represent sources and sinks of momentum and heat respectively, e.g, Rayleigh friction and convective heating and/or radiative cooling. These forcing terms are set to zero in the remainder of this work. Here, $N = 0.01\mathrm{s}^{-1}$ is the Brunt-Vaisala buoyancy frequency, $g = 9.80\ \mathrm{ms}^{-2}$ is the gravitational acceleration, θ_0= 300 K is the constant background potential temperature and $\beta = 2.2804 \times 10^{-11}\ \mathrm{s}^{-1}\mathrm{m}^{-1}$ is the meridional gradient of the Coriolis force at the equator. In addition,

$$\frac{D}{Dt} \equiv \frac{\partial}{\partial t} + U\frac{\partial}{\partial x} + V\frac{\partial}{\partial y} + W\frac{\partial}{\partial z}$$

is the material derivative, div_H and ∇_H are the horizontal divergence and horizontal gradient respectively. In the Boussinesq approximation the density is replaced by a constant mean density, everywhere except in the buoyancy term of the vertical momentum equation. We assume the rigid boundary conditions, i.e.,

$$W(x,y,z,t)|_{z=0,H_T} = 0 \tag{2.2}$$

where $z = 0$ and $z = H_T$ correspond to the surface of the Earth and the height of the troposphere which is 16 km.

2.1 Shallow Water Equations and the Equatorial Waves

In order to address the non-linear system (2.1), we first study the solutions to its simplified linear system by eliminating the nonlinear terms. This theory is well known and is studied in many texts [7, 28, 21]. Our analysis to derive these solutions follows closely the work in Majda's book [21]. We decompose each variable into a vertically averaged (so-called barotropic) component, denoted with overbars, and vertically varying (so-called baroclinic) components [21]

$$\begin{pmatrix} \mathbf{V} \\ P \end{pmatrix}(x,y,z,t) = \begin{pmatrix} \bar{\mathbf{v}} \\ \bar{p} \end{pmatrix}(x,y,t) + \sum_{q=1}^{+\infty} \begin{pmatrix} \mathbf{v^q} \\ p^q \end{pmatrix}(x,y,t) G^q(z) \tag{2.3}$$

$$\begin{pmatrix} W \\ \Theta \end{pmatrix} = \sum_{q=1}^{+\infty} \begin{pmatrix} w^q \\ \theta^q \end{pmatrix}(x,y,t) \frac{dG^q(z)}{dz} \tag{2.4}$$

where $G^q(z)$'s are to be determined. Note that the barotropic components of the vertical velocity and potential temperature vanish under rigid boundary and hydrostatic assumptions. If we ignore the barotropic components and plug in equations

(2.3)-(2.4) into the linearized system of (2.1), we obtain:

$$\begin{aligned} \frac{\partial \mathbf{v}^q}{\partial t} + \beta y \mathbf{v}^{q\perp} + \nabla p^q &= 0 \\ p^q &= \frac{g}{\theta_0}\theta^q \\ \frac{\partial \theta^q}{\partial t} + \frac{N^2\theta_0}{g} w^q &= 0 \\ \mathrm{div}\mathbf{v^q} G^q(z) + w^q \frac{d^2}{dz^2} G^q(z) &= 0. \end{aligned} \tag{2.5}$$

By some manipulations, we obtain

$$\mathrm{div}\ \mathbf{v^q} G^q(z) - \frac{1}{N^2}\frac{\partial p^q}{\partial t}\frac{d^2}{dz^2}G^q(z) = 0 \tag{2.6}$$

which is the well-known Sturm-Liouville problem where the solutions exist if and only if

$$\frac{d^2 G^q}{dz^2} = -\lambda_q^2 G^q. \tag{2.7}$$

Using rigid boundary conditions gives

$$\frac{dG^q}{dz} = 0, \text{at } z = 0 \text{ and } H_T \quad \text{for} \quad q = 1, 2, \ldots$$

which implies the following solutions

$$G^q(z) = \cos(\lambda_q z) \quad \text{where } \lambda_q = \frac{q\pi}{H_T}. \tag{2.8}$$

Therefore, we rewrite system (2.5) by plugging in (2.8), as follow:

$$\begin{aligned} \frac{\partial u}{\partial t} - \beta y v + c_q \frac{\partial p}{\partial x} &= 0 \\ \frac{\partial v}{\partial t} + \beta y u + c_q \frac{\partial p}{\partial y} &= 0 \\ \frac{\partial p}{\partial t} + c_q \frac{\partial u}{\partial x} + c_q \frac{\partial v}{\partial y} &= 0 \end{aligned} \tag{2.9}$$

where $p = \frac{p^q}{c_q}$, $c_q = \frac{N}{\lambda_q}, q = 1, 2, \ldots$ and the subscript q is dropped. This implies that the primitive equations decouple into an infinite number of shallow water equations in $x - y$ direction associated with each vertical mode q and with the characteristic

speed c_q.

2.1.1 Free equatorially trapped waves

The theoretical or so-called free equatorial waves are obtained from equations (3.1). By introducing the Riemann invariant variables

$$q = \frac{1}{\sqrt{2}}(p+u) \quad \text{and} \quad r = \frac{1}{\sqrt{2}}(p-u), \tag{2.10}$$

we can rewrite this system as

$$\begin{aligned} \frac{\partial q}{\partial t} + c_q\frac{\partial q}{\partial x} + \frac{c_q}{\sqrt{2}}(\frac{\partial v}{\partial y} - \frac{\beta}{c_q}yv) &= 0 \\ \frac{\partial r}{\partial t} - c_q\frac{\partial r}{\partial x} + \frac{c_q}{\sqrt{2}}(\frac{\partial v}{\partial y} + \frac{\beta}{c_q}yv) &= 0 \\ \frac{\partial v}{\partial t} + \frac{c_q}{\sqrt{2}}(\frac{\partial q}{\partial y} + \frac{\beta}{c_q}yq) + \frac{c_q}{\sqrt{2}}(\frac{\partial r}{\partial y} - \frac{\beta}{c_q}yr) &= 0 \end{aligned} \tag{2.11}$$

We look for wave-like solutions which decay exponentially as y goes to $\pm\infty$. Therefore, we write the solutions in series expansions and use the parabolic cylinder functions as the orthonormal basis:

$$\begin{pmatrix} q \\ r \\ v \end{pmatrix}(x,y,z,t) = \sum_{m=0}^{+\infty} \begin{pmatrix} \bar{q}_m \\ \bar{r}_m \\ \bar{v}_m \end{pmatrix}(x,t)\phi_m^q(y). \tag{2.12}$$

ϕ_m^q's are the normalized parabolic cylinder functions

$$\phi_m^q = \left(m!\sqrt{\pi c_q/\beta}\right)^{-\frac{1}{2}} 2^{-\frac{m}{2}} H_m((\frac{\beta}{c_q})^{\frac{1}{2}}y)e^{-(\frac{\beta}{c_q})\frac{y^2}{2}} \tag{2.13}$$

where the Hermite polynomials, H_m, are the well-known solutions of the harmonic oscillator

$$f''(\eta) + \frac{1}{2}(2m+1-\frac{\eta^2}{2})f(\eta) = 0.$$

We derive three systems by using the parabolic cylinder function properties explained thoroughly in section 3 of chapter 3:

- a single PDE for $\bar{q}_0$

$$\frac{\partial \bar{q}_0}{\partial t} + c_q\frac{\partial \bar{q}_0}{\partial x} = 0 \tag{2.14}$$

- a 2×2 system coupling $\bar{v_0}$ and $\bar{q_1}$

$$\begin{aligned} \frac{\partial \bar{v}_0}{\partial t} + (\beta c_q)^{\frac{1}{2}} \bar{q}_1 &= 0 \\ \frac{\partial \bar{q}_1}{\partial t} + c_q \frac{\partial \bar{q}_1}{\partial x} - (\beta c_q)^{\frac{1}{2}} \bar{v}_0 &= 0 \end{aligned} \tag{2.15}$$

- a system of coupling $\bar{r}_{m-2}$, $\bar{v}_{m-1}$ and $\bar{q}_m$ for $m \geq 2$

$$\begin{aligned} \frac{\partial \bar{q}_m}{\partial t} + c_q \frac{\partial \bar{q}_m}{\partial x} - (m\beta c_q)^{\frac{1}{2}} \bar{v}_{m-1} &= 0 \\ \frac{\partial \bar{r}_{m-2}}{\partial t} - c_q \frac{\partial \bar{r}_{m-2}}{\partial x} + ((m-1)\beta c_q)^{\frac{1}{2}} \bar{v}_{m-1} &= 0 \\ \frac{\partial \bar{v}_{m-1}}{\partial t} + (\beta c_q m)^{\frac{1}{2}} \bar{q}_m - ((m-1)\beta c_q)^{\frac{1}{2}} \bar{r}_{m-2} &= 0. \end{aligned} \tag{2.16}$$

By assuming the plane wave solutions in the form

$$\begin{pmatrix} \bar{q}_m(x,t) \\ \bar{r}_m(x,t) \\ \bar{v}_m(x,t) \end{pmatrix} = (\mathrm{Re} \begin{pmatrix} q_m \\ r_m \\ v_m \end{pmatrix} e^{i(kx-\omega t)}), \tag{2.17}$$

we get the free equatorially trapped wave solutions and their dispersion relations as follows, note that $p = \frac{p_q}{c_q}$:

1. **Kelvin Waves** which are the solution of equation (2.14) with dispersion relation

$$\omega = c_q k, \tag{2.18}$$

in form

$$\begin{pmatrix} p \\ u \\ v \end{pmatrix} (x,y,t) = f \begin{pmatrix} 1 \\ 1 \\ 0 \end{pmatrix} \cos(k(x - c_q t)) \phi_0^q(y). \tag{2.19}$$

2. **Mixed Rossby-gravity waves (MRG)** , also known as Yannai waves, are obtained from system (2.15) with dispersion relation

$$\omega_{\pm} = \frac{1}{2} c_q k \pm \frac{1}{2} \sqrt{(c_q k)^2 + 4\beta c_q} \tag{2.20}$$

and the solutions

$$\begin{pmatrix} p \\ u \\ v \end{pmatrix}(x,y,t) = \begin{pmatrix} \frac{1}{\sqrt{2}}\cos(kx-\omega_{\pm}t)\phi_1^q(y) \\ \frac{1}{\sqrt{2}}\cos(kx-\omega_{\pm}t)\phi_1^q(y) \\ ((\beta c_q)^{\frac{1}{2}}/\omega_{\pm})\sin(kx-\omega_{\pm}t)\phi_0^q(y). \end{pmatrix} \tag{2.21}$$

3. Equatorial Rossby and gravity waves which are the solutions to triad system (2.16) with characteristic equation

$$\omega(\omega^2 - c_q^2k^2) - \beta c_q((2m-1)\omega + c_qk) = 0,\ m \geq 2 \tag{2.22}$$

and the solutions

$$q_m = i\frac{(m\beta c_q)^{\frac{1}{2}}}{\omega - c_qk}v_{m-1}, \quad r_{m-2} = -i\frac{((m-1)\beta c_q)^{\frac{1}{2}}}{\omega + c_qk}v_{m-1},\ m \geq 2. \tag{2.23}$$

The characteristic equation can be written as

$$(\frac{\omega}{c_q})^2 - k^2 - \frac{\beta}{w}k = \frac{\beta}{c_q}(2M+1),\ \text{where } M = m-1 \geq 1 \tag{2.24}$$

This equation has three distinct solutions. If $\frac{w}{c_q}$ is small, the solution is

$$\omega_0(k) \approx -\frac{\beta k}{\frac{\beta}{c_q}(2M+1) + k^2},\ M \geq 1$$

corresponding to a Rossby wave and if $\frac{\beta}{c_q}k$ is small, then

$$\omega_{\pm}(k) \approx \pm\sqrt{c_q^2k^2 + c_q\beta(2M+1)},\ M \geq 1$$

which corresponds to the equatorial gravity waves.

Note that the parabolic cylinder functions, ϕ_m's, are even (odd) functions if m is an even (odd) integers. Those equatorial waves composed of even (odd) modes, basis functions, for the zonal velocity,u, and potential temperature, θ, for their meridional structures are called symmetric (anti-symmetric) equatorial waves. The physical interpretation of the symmetric/anti-symmetric waves is that the flow field, the pressure

and the potential temperature are all symmetric/anti-symmetric with respect to the equator. In Figure 2.1, we plot the dispersion relation for the theoretical equatorially trapped waves. This figure shows that Kelvin waves are non-dispersive waves, gravity waves travel faster compared to other waves and Rossby waves are the slowest. In Figure 2.2, we present the structure of a Kelvin wave, two MRG waves, a symmetric Rossby, a symmetric eastward gravity and a symmetric westward gravity waves of the first baroclinic mode. The contours represent the potential temperature, θ, and the arrows represent the horizontal velocity field.

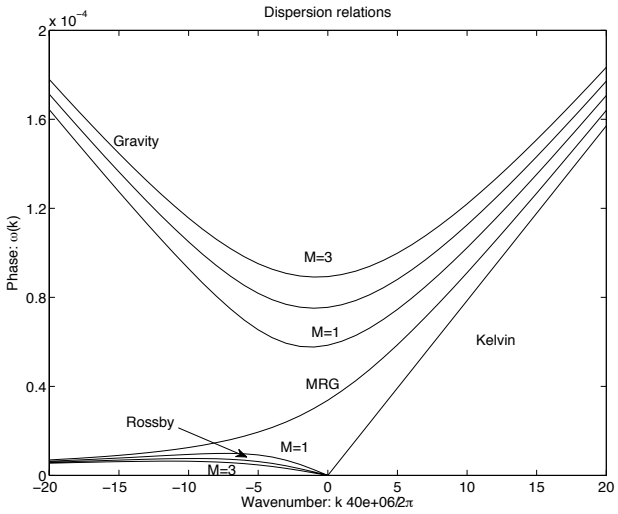

Figure 2.1: Phase versus the wavenumber normalized by the wavenumber 1 for the first baroclinic mode with $c_1 = 50$ ms^{-1}

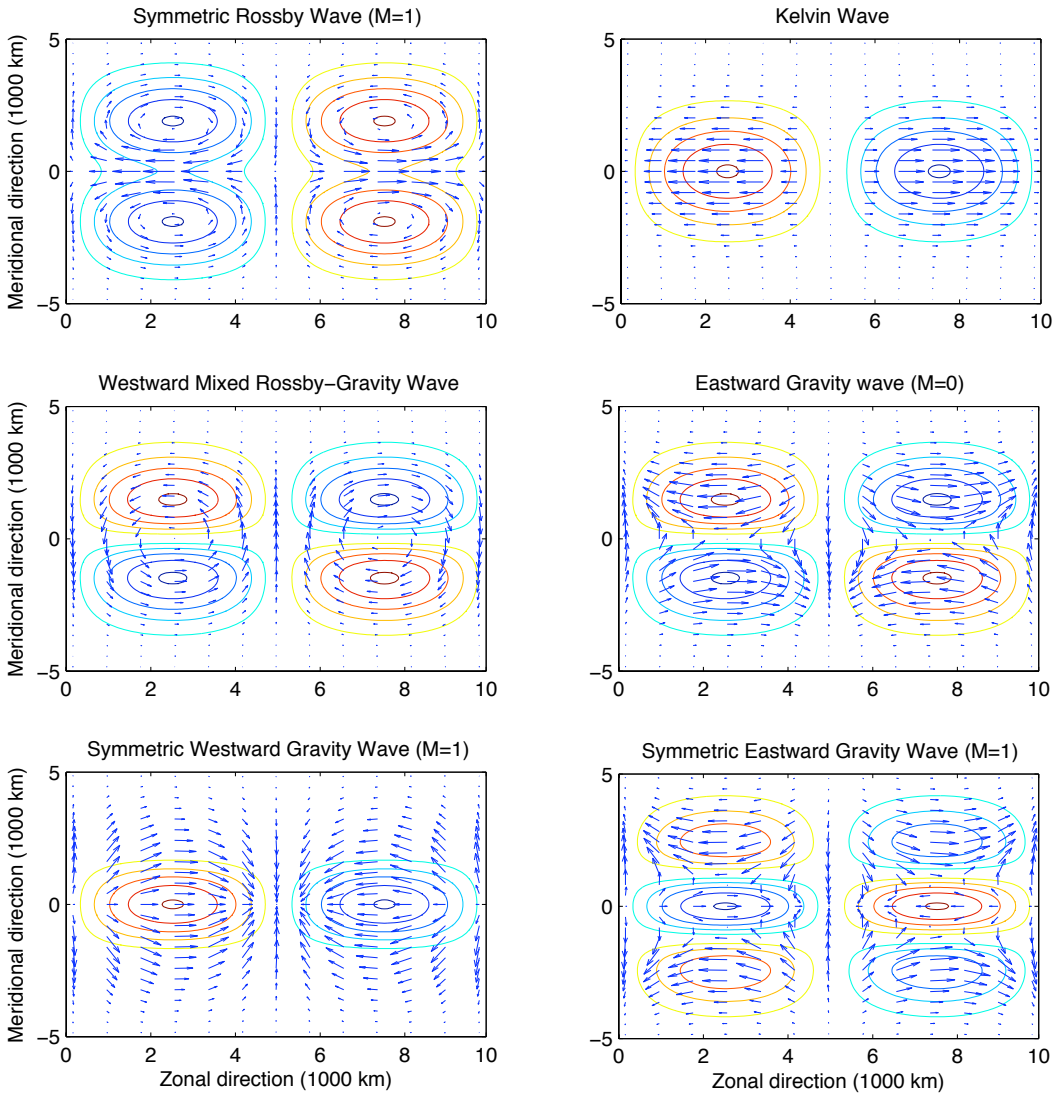

Figure 2.2: Flow velocity field overlaid on the contours of the potential temperature, θ for the free equatorial waves associated with the first baroclinic mode.

2.2 The model

It is shown in [22] that a model which involves a barotropic mode and a first baroclinic mode can capture important nonlinear equatorial interactions . Therefore, we consider the crude vertical approximation

$$\begin{pmatrix} \mathbf{V}_H \\ P \end{pmatrix}(x,y,z,t) \approx \begin{pmatrix} \bar{\mathbf{v}} \\ \bar{p} \end{pmatrix}(x,y,t) + \begin{pmatrix} \mathbf{v} \\ p \end{pmatrix}(x,y,t)\cos(\frac{\pi z}{H_T})$$
$$\begin{pmatrix} W \\ \Theta \end{pmatrix}(x,y,z,t) \approx \begin{pmatrix} w \\ \theta \end{pmatrix}(x,y,t)\sin(\frac{\pi z}{H_T}). \tag{2.25}$$

The barotropic-first baroclinic systems are obtained by applying the Galerkin projection of the primitive equations (2.1) on the barotropic and first baroclinic modes. The projection on the first baroclinic mode is derived by

$$\langle f,g\rangle = \frac{1}{H_T}\int_0^{H_T} f(z)g(z)dz,$$

where $g(z)=\cos(\frac{\pi z}{H_T})$ for the horizontal velocity, $\mathbf{V}_H$, and the pressure, P and $g(z)=\sin(\frac{\pi z}{H_T})$ for the potential temperature, Θ, and the vertical velocity, W. However, the projection on the barotropic mode is obtained in the same way with $g(z)=1$ for $\mathbf{V}_H$ and P. Moreover, in the remaining of the thesis, the equations are non-dimensionalized using $c=\frac{NH_T}{\pi}\approx 50\text{ms}^{-1}$ as velocity scale, $L=(c\beta^{-1})^{1/2}\approx 1500\text{km}$ as the length scale, $T=\frac{L}{c}\approx 8\text{h}$ as the time scale and $\bar{\alpha}=\frac{H_T N^2\theta_0}{\pi g}\approx 15\text{K}$ as the temperature scale, so that in this non-dimensional units the Coriolis parameter and the buoyancy frequency are set to $\beta=1$ and $N^2=1$. Therefore, the barotropic-first baroclinic interacting systems in non-dimensional units, are given:

$$\begin{aligned} &\frac{\partial\bar{\mathbf{v}}}{\partial} + \bar{\mathbf{v}}.\nabla\bar{\mathbf{v}} + y\bar{\mathbf{v}} + \nabla\bar{p} = -\frac{1}{2}(\mathbf{v}.\nabla\mathbf{v} + \mathbf{v}\text{div}\mathbf{v}) \\ &\text{div}\bar{\mathbf{v}} = 0 \end{aligned} \tag{2.26}$$

and

$$\begin{aligned} &\frac{\partial\mathbf{v}}{\partial t} + \bar{\mathbf{v}}.\nabla\mathbf{v} - \nabla\theta + y\mathbf{v}^{\perp} = -\mathbf{v}.\nabla\bar{\mathbf{v}} \\ &\frac{\partial\theta}{\partial t} + \bar{\mathbf{v}}.\nabla\theta - \text{div}\mathbf{v} = \mathbf{0} \end{aligned} \tag{2.27}$$

respectively. The readers should note the changes in the sign of basis function for W and Θ, $\sin(\lambda_q z)$, used in (2.4) and (2.25). We assume that the feedback of the associated baroclinic response in (2.26) is negligible; this is accurate to the first order approximation if this response is smaller than the imposed barotropic flow. Therefore, in order to investigate the interactions of equatorially trapped waves in a background barotropic flow, we only consider system (2.27) forced by equatorial barotropic shears.

2.2.1 Imposed barotropic Shear background

We prescribe two purely zonal barotropic shears $\bar{\mathbf{v}} = (\bar{u}(y), 0)$ where $\bar{u}(y)$ mimics the extratropical jet stream: an equatorial easterly shear with magnitude of -10 ms^{-1} at the equator and 40 ms^{-1} in mid-latitudes which is a typical meridional distribution of the zonal wind at 200 mb over the western Pacific ocean and an equatorial westerly shear with magnitude 10 ms^{-1} at the equator and 30 ms^{-1} in mid-latitudes which resembles the zonal wind over eastern Pacific ocean in winter at 200 mb Zhang and Webster (1989). Note that since the barotropic wind is non-divergent their zonal components depend on y only. The two zonal winds, in dimensional units, are formulated by

$$\begin{aligned}
\bar{u}_e(y) &= \bar{u}_0(\frac{3}{4}y^2 - 1)\exp(-y^2/16) \\
\bar{u}_w(y) &= \bar{u}_0(\frac{5}{12}y^2 + 1)\exp(-y^2/16)
\end{aligned}$$

where $\bar{u}_0$, the strength of the wind at the equator, is fixed to 10 ms^{-1}. The meridional distribution of these prescribed shears are shown in figure (2.3). We show the shears in dimensional units to ease the visualisation of their strengths and meridional distributions for the readers. By considering these barotropic shears, system (2.27) simplifies to

$$\begin{aligned}
&\frac{\partial u}{\partial t} + \bar{u}(y)\frac{\partial u}{\partial x} - yv - \frac{\partial \theta}{\partial x} = -v\frac{\partial \bar{u}}{\partial y}(y) \\
&\frac{\partial v}{\partial t} + \bar{u}(y)\frac{\partial v}{\partial x} + yu - \frac{\partial \theta}{\partial y} = 0 \\
&\frac{\partial \theta}{\partial t} + \bar{u}(y)\frac{\partial \theta}{\partial x} - (\frac{\partial u}{\partial x} + \frac{\partial v}{\partial y}) = 0.
\end{aligned} \tag{2.28}$$

which are advected shallow water equations forced by the barotropic shears.

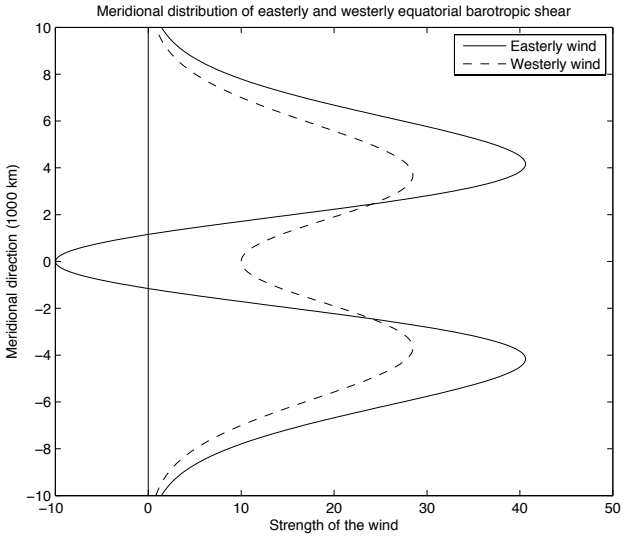

Figure 2.3: Structure of equatorially easterly barotropic shear $\bar{u}_e(y)$ and equatorially westerly barotropic shear $\bar{u}_w(y)$.

2.2.2 Energy source and energy sink

Here, we consider a narrow channel-like periodic stripe centred around the equator and is 40,000 km long and about 10,000 km wide where x denotes the east-west or zonal coordinate, y is the north-south or meridional coordinate, and t is time. The kinetic energy associated with the first baroclinic mode is

$$E_c(t) = \frac{1}{2}\int_{-Y_0}^{Y_0}\int_{0}^{X}(u^2 + v^2 + \theta^2)dxdy. \tag{2.29}$$

The energy tendency is given by

$$\frac{d}{dt}E_c(t) = -2(\int_{0}^{X} v\theta\Big|_{Y_0} dx + \int_{0}^{Y_0}\int_{0}^{X} uv\frac{\partial\bar{u}}{\partial y}dxdy) \tag{2.30}$$

using the fact that the barotropic flow is non-divergent and periodic boundary conditions in the zonal direction. This shows that the energy tendency depends on the interaction between u, v and the gradient of the barotropic wind (interaction energy tendency) and also depends on the structure of the wave at the channel walls (boundary energy tendency). This kinetic energy is conserved if the barotropic wind is uniform (constant), with respect to a fixed coordinate, which makes the second in-

tegral equal to zero and if the waves are sufficiently trapped around the equator, i.e., $u = v = \theta \approx 0$. We assume the Dirichlet boundary conditions for meridional direction which is reasonable as long as the forced waves are trapped around the equator.

2.3 Shallow water equations of Matsuno, effect of the baroclinicity of the background shear

Another model widely used to study the equatorial dynamics in the atmospheric modelling is the shallow water equations of Matsuno (1966) on the beta-plane. These linear, inviscid, shallow water equations are given by

$$\begin{aligned} &\frac{\partial u}{\partial t} + \bar{u}(y)\frac{\partial u}{\partial x} - yv - \frac{\partial \theta}{\partial x} + v\frac{\partial \bar{u}}{\partial y} = 0, \\ &\frac{\partial v}{\partial t} + \bar{u}(y)\frac{\partial v}{\partial x} + yu - \frac{\partial \theta}{\partial y} = 0, \\ &\frac{\partial \theta}{\partial t} + \bar{u}(y)\frac{\partial \theta}{\partial x} + y\bar{u}(y)v - (\frac{\partial u}{\partial x} + \frac{\partial v}{\partial y}) = 0. \end{aligned} \tag{2.31}$$

This system is similar to the shallow water equation derived by projecting the primitive equations onto the barotropic-first baroclinic mode, system (2.27), except for the extra term $y\bar{u}(y)v$ in the potential temperature, θ, equation. This system is used by Zhang and Webster in [43] to study imposed background flows through linear analysis. A system of PDE in y, meridional direction, and t, time, was derived by assuming wavelike solutions in the zonal direction. The eigenvectors of the PDE was expressed in terms of the first few free equatorially trapped waves of Matsuno (1966).

We can derive a similar system if we assume that the background shear consists of two components: a barotropic component and a vertical component which is associated with the first baroclinic mode, $\bar{U} = \bar{u} + \bar{u}_1(y)\cos(\frac{\pi z}{H_T})$. By applying the thermal wind equation and the projection scheme to the primitive equations, we get:

$$\begin{aligned}
&\frac{\partial u}{\partial t} + \bar{u}(y)\frac{\partial u}{\partial x} - yv - \frac{\partial \theta}{\partial x} + v\frac{\partial \bar{u}}{\partial y} = 0,\\
&\frac{\partial v}{\partial t} + \bar{u}(y)\frac{\partial v}{\partial x} + yu - \frac{\partial \theta}{\partial y} = 0,\\
&\frac{\partial \theta}{\partial t} + \bar{u}(y)\frac{\partial \theta}{\partial x} + y\bar{u}_1(y)v - (\frac{\partial u}{\partial x} + \frac{\partial v}{\partial y}) = 0.
\end{aligned} \tag{2.32}$$

Note that by comparing this obtained system with the one in (2.31), we see that each component of the background shear, the barotropic and the baroclinic modes, acts differently on the system. The extension of the model to the one including both barotropic and the first baroclinic background is the topic of a future work. Here, We compare some of the results we obtain by using the projected shallow water equations (2.27) with the results of [43] in chapter 5.

In this dissertation, we only consider and investigate the effect of the barotropic shear background on the equatorial waves. Here, the methodology is extended by using a more general and simpler treatment where each variable of the solutions are projected meridionally onto the first few parabolic cylinder functions. In addition to the standard linear theory, we perform direct integrations in time from an initial state consistent with a given wave-mode solution by using the high-order numerical scheme. This way, the dynamical interactions between the barotropic modes and these equatorial waves can be captured.

Chapter 3

Methodology

In this section, we briefly present the three numerical methods we use to approximate system (2.27). Complete discussions can be found in the cited literatures.

3.1 The f-wave algorithm

The f-wave algorithm is a finite volume method for conservation laws with varying flux functions introduced by Bale et al. [1]. We rewrite the System (2.28) in the form of conservation laws,

$$\begin{aligned} &\frac{\partial u}{\partial t} + \frac{\partial}{\partial x}(\bar{u}u - \theta) = yv - v\frac{\partial \bar{u}}{\partial y} \\ &\frac{\partial v}{\partial t} + \frac{\partial}{\partial x}(\bar{u}v) - \frac{\partial \theta}{\partial y} = -yu \\ &\frac{\partial \theta}{\partial t} + \frac{\partial}{\partial x}(\bar{u}\theta - u) - \frac{\partial v}{\partial y} = 0 \end{aligned} \tag{3.1}$$

by using the fact that the barotropic wind is divergence free. It is more convenient to implement the f-wave method for one-dimensional systems. So, we use the dimensional splitting strategy following [12] and rewrite System (3.1) as the superposition of the following two one-dimensional balance laws:

$$\begin{aligned} &\frac{\partial u}{\partial t} + \frac{\partial}{\partial x}(\bar{u}u - \theta) = yv - v\frac{\partial \bar{u}}{\partial y} \\ &\frac{\partial \theta}{\partial t} + \frac{\partial}{\partial x}(\bar{u}\theta - u) = 0 \\ &\frac{\partial v}{\partial t} + \frac{\partial}{\partial x}(\bar{u}v) = 0 \end{aligned} \tag{3.2}$$

and

$$\begin{aligned} &\frac{\partial v}{\partial t} - \frac{\partial \theta}{\partial y} + yu = 0 \\ &\frac{\partial \theta}{\partial t} - \frac{\partial v}{\partial y} = 0 \\ &\frac{\partial u}{\partial t} = 0. \end{aligned} \tag{3.3}$$

To guarantee second order accuracy, we apply the Strang-splitting methodology when evolving Systems (3.2) and (3.3) alternatively at each time step. The f-wave method is an improvement of the wave propagation algorithm of Leveque [18] where instead of the solution increments, the flux increments are decomposed directly into wave components. In the following subsection, we describe the wave propagation algorithm for the sake of completeness.

3.1.1 The wave propagation algorithm for conservation laws

Consider a scalar conservation law,

$$u_t + (f(u))_x = 0 \tag{3.4}$$

where its finite-volume approximation over the control cell $[t^n, t^{n+1}] \times [x_{j-\frac{1}{2}}, x_{j+\frac{1}{2}}]$ is given by

$$U_i^{n+1} = U_i^n - \frac{\Delta t}{\Delta x}\left[F(U^*_{i+\frac{1}{2}}) - F(U^*_{i-\frac{1}{2}})\right]. \tag{3.5}$$

Here, $U^*_{i+\frac{1}{2}}$ is the solution of the Riemann problem at the interface $i+\frac{1}{2}$ with the left and right states $U_l = U_i$ and $U_r = U_{i+1}$ and $F(U)$ is the numerical flux. For a hyperbolic system, the jumps $U_i - U_{i-1}$ can be decomposed onto M waves, $W^p_{i-\frac{1}{2}}$, with propagation speeds $\lambda^p_{i-\frac{1}{2}}$'s for $p = 1, \ldots, M$ where M is the dimension of the system. $\lambda^p_{i-\frac{1}{2}}$ and $W^p_{i-\frac{1}{2}}$ are respectively the eigenvalues and the projection onto the associated eigenvectors, $R^p_{i-\frac{1}{2}}$, of the Jacobian matrix $\frac{\partial}{\partial U}F(U)$ [18]. Therefore,

$$U_i - U_{i-1} = \sum_{p=1}^{M} W^p_{i-\frac{1}{2}} \tag{3.6}$$

and consequently

$$F(U_i) - F(U_{i-1}) = \sum_{p=1}^{M} \lambda^p_{i-\frac{1}{2}} W^p_{i-\frac{1}{2}}. \tag{3.7}$$

The flux increment can be decomposed onto left going and right going waves as follows

$$\begin{aligned} F(U_i) - F(U_{i-1}) \quad &= \sum_{p=1}^{M} (\lambda^p_{i-\frac{1}{2}})^+ W^p_{i-\frac{1}{2}} + \sum_{p=1}^{M} (\lambda^p_{i-\frac{1}{2}})^- W^p_{i-\frac{1}{2}} \\ &= A^+(\Delta U_{i-\frac{1}{2}}) + A^-(\Delta U_{i-\frac{1}{2}}) \end{aligned}$$

where $\lambda^+ = \max(\lambda, 0)$, $\lambda^- = \min(\lambda, 0)$ and

$$\begin{aligned} A^-(\Delta U_{i-\frac{1}{2}}) &= \sum_{p=1}^{M} (\lambda^p_{i-\frac{1}{2}})^- W^p_{i-\frac{1}{2}} \\ A^+(\Delta U_{i-\frac{1}{2}}) &= \sum_{p=1}^{M} (\lambda^p_{i-\frac{1}{2}})^+ W^p_{i-\frac{1}{2}}. \end{aligned}$$

Therefore, (3.5) becomes

$$U_i^{n+1} = U_i^n - \frac{\Delta t}{\Delta x}[A^+(\Delta u_{i-\frac{1}{2}}) + A^-(\Delta U_{i+\frac{1}{2}})]. \tag{3.8}$$

In order to achieve a second order approximation, a flux correction is added to this equation [18]. Therefore, we obtain the following numerical scheme for (3.4)

$$U_i^{n+1} = U_i^n - \frac{\Delta t}{\Delta x}[A^+(\Delta u_{i-\frac{1}{2}}) + A^-(\Delta U_{i+\frac{1}{2}})] - \frac{\Delta t}{\Delta x}(\tilde{F}_{i+\frac{1}{2}} - \tilde{F}_{i-\frac{1}{2}}), \tag{3.9}$$

where the correction is formulated by

$$\tilde{F}_{i-\frac{1}{2}} = \frac{1}{2} \sum_{p=1}^{M} |\lambda^p_{i-\frac{1}{2}}| \left(1 - \frac{\Delta t}{\Delta x} |\lambda^p_{i-\frac{1}{2}}|\right) \tilde{W}^p_{i-\frac{1}{2}} \tag{3.10}$$

with

$$\tilde{W}^p_{i-\frac{1}{2}} = limiter(W^p_{i-\frac{1}{2}}, W^p_{l-\frac{1}{2}}), \quad l = \begin{cases} i-1 & \text{if } \lambda^p_{i-\frac{1}{2}} > 0 \\ i+1 & \text{if } \lambda^p_{i-\frac{1}{2}} < 0. \end{cases} \tag{3.11}$$

Here, *limiter* refers to the usual flux a limiting function used to guarantee a non-oscillatory scheme [18].

3.1.2 The f-wave algorithm

The f-wave algorithm is an extension of the wave propagating method. The main idea is to directly decompose the flux increment onto waves, instead of decomposing the solution increments; since ultimately the flux increments rather than the solution increments are needed in order to update the solution at the next time step. This makes the f-wave method somewhat more straightforward and efficient. The flux increments are projected onto the eigenvectors of the Jacobian matrix at the cell edge $i - \frac{1}{2}$.

$$F(U_i) - F(U_{i-1}) = \sum_{p=1}^{M} \beta_p R_p = \sum_{p=1}^{M} \mathcal{Z}^p_{i-\frac{1}{2}} \tag{3.12}$$

with the second order flux corrections given by

$$\tilde{F}_{i-\frac{1}{2}} = \frac{1}{2} \sum_{p=1}^{M} \left(1 - \frac{\Delta t}{\Delta x} |\lambda^p_{i-\frac{1}{2}}|\right) \text{sign}(\lambda^p_{i-\frac{1}{2}}) \mathcal{Z}^p_{i-\frac{1}{2}}. \tag{3.13}$$

3.1.3 The f-wave algorithm for a balanced law

The f-wave algorithm is easily generalized for non-homogeneous conservation laws, i.e balance laws. Consider the balance law

$$u_t + F_x(u) + B(u) = 0. \tag{3.14}$$

We redistribute the forcing term as a delta function on the cell interface and then decompose the sum of the flux increment and the forcing term onto waves, i.e.,

$$F(U_{i+1}) - F(U_i) + \Delta x B(U_{i+\frac{1}{2}}) = \sum_{p=1}^{M} \mathcal{Z}^p_{i+\frac{1}{2}} \tag{3.15}$$

where $B(U_{i+\frac{1}{2}})$ is the approximation of the forcing at the edges $i + \frac{1}{2}$. In this work, we use the nearest neighbours average, $B(U_{i+\frac{1}{2}}) = (B(U_i) + B(U_{i+1}))/2$. Moreover,

$$\frac{(\Delta t)^2}{2\Delta x} \frac{\partial B(U_i)}{\partial U} \sum_{p=1}^{M} \frac{\mathcal{Z}^p_{i+\frac{1}{2}} + \mathcal{Z}^p_{i-\frac{1}{2}}}{2}$$

is added to the correction terms to achieve a second order approximation for the forcing term. We note that this feature is exploited in [12, 13] to guarantee a good

approximation of small or no deviations from geostrophic balance between the potential temperature gradient and the Coriolis force in equatorially trapped waves.

3.2 The Central scheme

The central scheme of Nessyahu and Tadmor (NT) [27] is an extension of the Lax-Friedrichs scheme which uses a high order polynomial instead of piecewise constant function to reconstruct the solution within the grid cells for each time step to achieve high order convergence in smooth regions. We use the second order central scheme to evolve (2.28) in time. The second order NT scheme on a non-staggered grid for a balance law in one dimension

$$\frac{\partial u}{\partial t} + \frac{\partial f}{\partial x} = g(u) \tag{3.16}$$

can be derived through the following two steps.

1. Given the cell average of the solution u_j^n, we construct a piecewise linear function on each grid cell $x_j \leq x \leq x_{j+2}$ by the given data at time t^n,

$$L_{j+1}(x, t^n) = u_{j+1}^n + (x - x_{j+1})\frac{1}{2\Delta x}u'_{j+1} \tag{3.17}$$

   where $\frac{1}{2\Delta x}u'_{j+1}$ is a certain approximation of the slope of u within the grid cell, chosen in such a way to preserve stability of the scheme.

2. We perform a finite volume integration on the control cell $[t^n, t^{n+1}] \times [x_{j-1}, x_{j+1}]$ to avoid the Riemann problem at the cell edges, which yields the cell averages of the solution u_j^{n+1} at time $t + \Delta t$ and at each grid cell.

Therefore, the approximation for u at time $t + \Delta t$ is formulated by

$$\bar{u}_j(t + \Delta t) = \frac{1}{2}[u_{j-1}(t) + u_{j+1}(t)] + \frac{1}{4}[u'_{j-1} - u'_{j+1}] - \frac{\Delta t}{\Delta x}[f(u(x_{j+1}, t + \frac{\Delta t}{2})) - f(u(x_{j-1}, t + \frac{\Delta t}{2}))] + \frac{1}{2\Delta x}I_g \tag{3.18}$$

where

$$I_g = \int_{x_{j-1}}^{x_{j+1}} \int_{t^n}^{t^{n+1}} g(u(x))dtdx. \tag{3.19}$$

I_g can be approximated using any explicit or implicit quadrature formula, [27, 30].

3.3 The Galerkin projection method

In this section, we present the semi-Galerkin method to solve (2.28) which consists of projecting the governing equations in the y-direction onto the first few parabolic cylinder functions [23]. This gives a system of PDEs in one spatial dimension, x. Then, we evolve this meridionally projected system from an initial state consisting of an equatorially trapped wave solution by a direct integration using non-oscillatory numerical scheme for conservation laws namely the second order central scheme. Note that although the Galerkin truncation is performed only in the y-direction, we still refer to this method as Galerkin method.

3.3.1 The Galerkin projection in the meridional direction

Here, we present the parabolic cylinder functions and some of their properties which are used to design the projection method following [23]. Unlike [23], where the projected equations are used only for the linear analysis of the unforced system, here we apply the Galerkin projection method for the first time to make a systematic integration in time for the simple case of the advected equatorial shallow water system (2.28) which nevertheless provides an important test case with fairly complex dynamics. A detailed discussion of the Galerkin truncation using the parabolic cylinder functions can be found in [23]. Its major steps are discussed below and then applied to the forced shallow water system (2.28).

To begin, we introduce the parabolic cylinder functions as

$$D_m(\eta) = 2^{-m/2} H_m(\frac{\eta}{\sqrt{2}}) e^{-\eta^2/4} \tag{3.20}$$

where $H_m(\xi)$ are the Hermite polynomials, given by

$$H_m(\xi) = (-1)^m e^{\xi^2} \frac{d^m e^{-\xi^2}}{d\xi^m} \quad \text{for} \quad m = 0, 1, \ldots.$$

We recall that the Hermite polynomials satisfy the following recursive formula

$$H_{j+1}(\xi) - 2\xi H_j(\xi) + 2j H_{j-1}(\xi) = 0, \quad H_0(\xi) = 1, \; H_1(\xi) = 2\xi.$$

Consequently, the normalized parabolic cylinder functions, $\phi_N(y) = (N!\sqrt{\pi})^{-\frac{1}{2}} D_N(\sqrt{2}y)$,

form an orthonormal basis for the square integrable functions, i.e.,

$$(\phi_N, \phi_M) = \int_{-\infty}^{\infty} \phi_N(y)\phi_M(y)d(y) = \delta_{N,M}. \tag{3.21}$$

Therefore, any given function $f \in L^2(\mathbb{R}^2)$ can be projected onto the discrete space spanned by the orthonormal basis, i.e,

$$P_N f(y) = \sum_{l=0}^{N-1} \tilde{f}_l \phi_l(y), \tag{3.22}$$

where

$$\tilde{f}_l = \langle f, \phi_l \rangle_N = \sum_{j=1}^{N} f(y_j)\phi_l(y_j)\mathrm{H}_j e^{y_j^2}, \quad l = 0, \ldots, N-1 \tag{3.23}$$

and $y_j, j = 1, 2, \ldots, N$ are the N zeros of the Hermite polynomial H_N for a given N while the H_j's are the standard Hermite-Gauss quadrature coefficient given by

$$\mathrm{H}_j = \frac{2^{N-1}N!\sqrt{\pi}}{N^2(H_{N-1}(y_j))^2}.$$

This approximation is exact, $P_N f = f$, if f is in the form $p_{N-1}(y)e^{-y^2/2}$ [23], where p_{N-1} is polynomial of order $N-1$. Moreover, we have

$$\begin{aligned} L_-\phi_N(y) &= -(2(N+1))^{1/2}\phi_{N+1}(y), \\ L_+\phi_N(y) &= (2N)^{1/2}\phi_{N-1}(y). \end{aligned}$$

where $L_\pm = \frac{d}{dy} \pm y$ are the lowering and raising operators of quantum mechanics. By using the above identities and properties, we get an explicit formula for $P_N \frac{\partial}{\partial y} P_N u$,

$$P_N \frac{\partial}{\partial y} P_N u = \sum_{l=0}^{N-1} \frac{1}{\sqrt{2}} (\tilde{u}_{l+1}(l+1)^{1/2} - \tilde{u}_{l-1} l^{1/2})\phi_l(y) \tag{3.24}$$

and similarly,

$$P_N y P_N u(y) = \sum_{l=0}^{N-1} \frac{1}{\sqrt{2}} (\tilde{u}_{l+1}(l+1)^{\frac{1}{2}} + \tilde{u}_{l-1} l^{\frac{1}{2}})\phi_l(y) \tag{3.25}$$

where we used the relations $P_N\phi_l = \phi_l$ for $l = 0, \ldots, N-1$, $P_N\phi_N \equiv 0$ and the

convention $\tilde{u}_{-1} = \tilde{u}_N \equiv 0$. By applying this meridional projection for advected shallow water equations (2.28), we obtain a one-dimensional advection system

$$\frac{\partial \tilde{W}}{\partial t} + A\frac{\partial \tilde{W}}{\partial x} + (B+C)\tilde{W} = 0 \tag{3.26}$$

for $\tilde{W} = (\tilde{u}_0, \ldots, \tilde{u}_{N-1}, \tilde{v}_0, \ldots, \tilde{v}_{N-1}, \tilde{\theta}_0, \ldots, \tilde{\theta}_{N-1})'$ and the constant coefficient matrices $A, B, C \in M_{3N\times 3N}$ are given by

$$A = \begin{pmatrix} A_1 & 0 & -I_N \\ 0 & A_1 & 0 \\ -I_N & 0 & A_1 \end{pmatrix},\ B = -\frac{1}{\sqrt{2}}\begin{pmatrix} 0 & B_1 & 0 \\ -B_1 & 0 & B_2 \\ 0 & B_2 & 0 \end{pmatrix},\ C = \begin{pmatrix} 0 & C_1 & 0 \\ 0 & 0 & 0 \\ 0 & 0 & 0 \end{pmatrix}$$

where

$$A_1 = \begin{pmatrix} \bar{u}_{0,0} & \bar{u}_{0,1} & \cdots & \bar{u}_{0,N-1} \\ \bar{u}_{1,0} & \bar{u}_{1,1} & \cdots & \bar{u}_{1,N-1} \\ \vdots & & & \\ \bar{u}_{N-1,0} & \bar{u}_{N-1,1} & \cdots & \bar{u}_{N-1,N-1} \end{pmatrix},\ I_N = \begin{pmatrix} 1 & 0 & \cdots & 0 \\ 0 & 1 & \cdots & 0 \\ \vdots & & \ddots & \\ 0 & 0 & \cdots & 1 \end{pmatrix},$$

$$B_1 = \begin{pmatrix} 0 & 1 & 0 & & 0 \\ 1 & 0 & \sqrt{2} & & \\ & \sqrt{2} & \ddots & \ddots & \\ & & \ddots & 0 & \sqrt{N-1} \\ 0 & & \sqrt{N-1} & & 0 \end{pmatrix},\ B_2 = \begin{pmatrix} 0 & 1 & 0 & & 0 \\ -1 & 0 & \sqrt{2} & & \\ & -\sqrt{2} & \ddots & \ddots & \\ & & \ddots & 0 & \sqrt{N-1} \\ 0 & & -\sqrt{N-1} & & 0 \end{pmatrix}$$

and

$$C_1 = \begin{pmatrix} \hat{u}_{0,0} & \hat{u}_{0,1} & \cdots & \hat{u}_{0,N-1} \\ \hat{u}_{1,0} & \hat{u}_{1,1} & \cdots & \hat{u}_{1,N-1} \\ \vdots & & & \\ \hat{u}_{N-1,0} & \hat{u}_{N-1,1} & \cdots & \hat{u}_{N-1,N-1} \end{pmatrix}.$$

Here

$$\bar{u}_{m,l} = \sum_{j=1}^{N} \bar{u}(y_j)\phi_m(y_j)\phi_l(y_j)\mathrm{H}_j e^{y_j^2},$$

and

$$\hat{u}_{m,l} = \sum_{j=1}^{N} \bar{u}_y(y_j)\phi_m(y_j)\phi_l(y_j)\mathrm{H}_j e^{y_j^2}.$$

Radiation condition

In order to avoid spurious waves introduced by numerical approximation, we need to impose the following radiation conditions [23, 17].

$$\tilde{v}_{N-1} = 0, \tilde{\theta}_{N-1} = -\tilde{u}_{N-1}, \tilde{\theta}_{N-2} = -\tilde{u}_{N-2}. \tag{3.27}$$

If we neglect the barotropic terms in System (3.26), we have

$$\frac{\partial \tilde{u}_k}{\partial t} - \frac{\partial \tilde{\theta}_k}{\partial x} - \frac{1}{\sqrt{2}}(\tilde{v}_{k+1}(k+1)^{1/2} + \tilde{v}_{k-1}(k)^{1/2}) = 0, \tag{3.28}$$

$$\frac{\partial \tilde{v}_k}{\partial t} - \frac{1}{\sqrt{2}}(\tilde{\theta}_{k+1}(k+1)^{1/2} - \tilde{\theta}_{k-1}(k)^{1/2}) + \frac{1}{\sqrt{2}}(\tilde{u}_{k+1}(k+1)^{1/2} + \tilde{u}_{k-1}(k)^{1/2}) = 0, \tag{3.29}$$

$$\frac{\partial \tilde{\theta}_k}{\partial t} - \frac{\partial \tilde{u}_k}{\partial x} - \frac{1}{\sqrt{2}}(\tilde{v}_{k+1}(k+1)^{1/2} - \tilde{v}_{k-1}(k)^{1/2}) = 0. \tag{3.30}$$

By using the radiation condition $\tilde{v}_{N-1} = 0$ and $\tilde{\theta}_{N-2} = -\tilde{u}_{N-2}$, Equation (3.29) for $k = N-1$ is spare and is omitted from (3.26). By using these radiation conditions for $k = N-2, N-3$, this equation becomes

$$\frac{\partial \tilde{v}_k}{\partial t} + \frac{2}{\sqrt{2}}\tilde{u}_{k+1}(k+1)^{1/2} + \frac{k^{1/2}}{\sqrt{2}}(\tilde{u}_{k-1} + \tilde{\theta}_{k-1}) = 0. \tag{3.31}$$

However, (3.28) and (3.30) give two conflicting equations

$$\begin{aligned} &\tfrac{\partial \tilde{u}_k}{\partial t} + \tfrac{\partial \tilde{u}_k}{\partial x} - \tfrac{1}{\sqrt{2}}(\tilde{v}_{k+1}(k+1)^{1/2} + \tilde{v}_{k-1}(k)^{1/2}) = 0, \\ &\tfrac{\partial \tilde{u}_k}{\partial t} + \tfrac{\partial \tilde{u}_k}{\partial x} + \tfrac{1}{\sqrt{2}}(\tilde{v}_{k+1}(k+1)^{1/2} - \tilde{v}_{k-1}(k)^{1/2}) = 0 \end{aligned}$$

for $k = N-2, N-1$ by using radiation condition $\tilde{\theta}_k = -\tilde{u}_k$. This is due to the fact that the nature of the forcing acts on u and θ differently so the results are sensitive to

the choice of one equation or the order. We handle this problem by averaging these equations to arrive at [17]

$$\frac{\partial \tilde{u}_k}{\partial t} + \frac{\partial \tilde{u}_k}{\partial x} - \frac{1}{\sqrt{2}} \tilde{v}_{k-1}(k)^{1/2} = 0. \tag{3.32}$$

The same averaging strategy holds for the forced case.

Chapter 4

Poor performance of the central scheme for equatorial waves

In this chapter, we study the evolution of a Kelvin wave in the meridional shear environment. Kelvin waves are the subject of many studies since they play an important role in organized tropical convective superclusters. The issue of the effect of a background shear on these waves has been the focus of many research papers during the past few decades [37, 38, 39, 44, 36]. However, it has been argued in most of these works (e.g. [39, 44]) that the effect of the background shear on Kelvin waves is negligible and past studies have been concentrated mostly on other equatorial waves such as mixed Rossby-gravity, Rossby, and westward gravity waves.

Unlike the theoretical Kelvin waves where the meridional velocity and meridional convergence are exactly zero, their observed counterparts are non-trivial [42, 29, 34]. The origin of this meridional wind deviation and its effect on the dynamics of the waves remain unexplored except for the study done by Dias and Pauluis [3]. Here, we demonstrate that such non-Kelvin aspects can be generated through the interactions of a Kelvin wave with the prescribed meridional barotropic shear.

4.1 An exactly balanced numerical scheme for Kelvin waves

Note that the shear-free Kelvin wave solutions, presented in Section 2.1, satisfy geostrophic balance in the meridional direction: $yu - \frac{\partial \theta}{\partial y} = 0$. Well balanced schemes

for conservation laws with forcing aim to capture with high accuracy any small deviations from steady state. The f-wave method in particular is designed so that the numerical steady states are exactly preserved to machine precision and therefore can be used to enforce an additional constraint on the governing equations such as the hydrostatic balance or the meridional geostrophic balance for the case of a Kelvin wave. However, unless some clever discretization for the flux term is utilized a steady state (or any other constraint such as the geostrophic balance in y) for the continuous equations is not necessarily preserved after discretization:

$$yu - \frac{\partial \theta}{\partial y} = 0 \nRightarrow yu - \hat{\partial}_y \theta = 0$$

where $\hat{\partial}_y$ stands for the numerical derivative of some sort. Nevertheless, the validation experiments conducted in [12] demonstrated that the induced deviation from meridional geostrophy and the resulting meridional velocity for the discretized Kelvin wave, remained reasonably small as the system is integrated over relatively long periods of time, perhaps all because of the good balanced properties of the f-wave scheme. However, since a weak meridional shear is expected to weakly distort the geostrophic balance for the Kelvin wave and therefore induce a weak but non-zero meridional wind, it is highly desirable to eliminate the deviation from geostrophy at the initial time that are due to discretization errors.

To do this, we introduce the following auxiliary variables that measure the geostrophic imbalance in the meridional direction and therefore the deviations from the Kelvin wave-background solution. Let

$$\xi = yu - \frac{\partial \theta}{\partial y} \text{ and } \nu = y\theta - \frac{\partial u}{\partial y}$$

Notice that both ξ and ν are zero in the case of a Kelvin wave solution. Therefore the baroclinic system (2.28) can be relaxed in terms of the new variables to the

five-equations system

$$\begin{aligned}
&\frac{\partial u}{\partial t}+\bar{u}\frac{\partial u}{\partial x}-\frac{\partial \theta}{\partial x}-yv=-v\frac{\partial \bar{u}}{\partial y}\\
&\frac{\partial v}{\partial t}+\bar{u}\frac{\partial v}{\partial x}+\xi=0\\
&\frac{\partial \theta}{\partial t}+\bar{u}\frac{\partial \theta}{\partial x}-\left(\frac{\partial u}{\partial x}+\frac{\partial v}{\partial y}\right)=0\\
&\frac{\partial \xi}{\partial t}+\bar{u}\frac{\partial \xi}{\partial x}-\frac{\partial \bar{u}}{\partial y}\frac{\partial \theta}{\partial x}-\frac{\partial \nu}{\partial x}=-\frac{\partial^2 v}{\partial y^2}+y^2v-yv\frac{\partial \bar{u}}{\partial y}\\
&\frac{\partial \nu}{\partial t}+\bar{u}\frac{\partial \nu}{\partial x}-\frac{\partial \bar{u}}{\partial y}\frac{\partial u}{\partial x}-\frac{\partial \xi}{\partial x}=-v+\frac{\partial v}{\partial y}\frac{\partial \bar{u}}{\partial y}+v\frac{\partial^2 \bar{u}}{\partial y^2}.
\end{aligned} \tag{4.1}$$

Note that if $\bar{u}(y)=0$, the relaxation system (4.1) reduces to

$$\begin{aligned}
&\frac{\partial u}{\partial t}-\frac{\partial \theta}{\partial x}-yv=0\\
&\frac{\partial v}{\partial t}+\xi=0\\
&\frac{\partial \theta}{\partial t}-\left(\frac{\partial u}{\partial x}+\frac{\partial v}{\partial y}\right)=0\\
&\frac{\partial \xi}{\partial t}-\frac{\partial \nu}{\partial x}=-\frac{\partial^2 v}{\partial y^2}+y^2v\\
&\frac{\partial \nu}{\partial t}-\frac{\partial \xi}{\partial x}=0
\end{aligned} \tag{4.2}$$

Clearly, in the absence of a background flow, if (4.2) is solved numerically with a conservative scheme, the geostrophic balance and the zero meridional velocity of the Kelvin wave are preserved exactly. At time $t=0$, $v=\xi=\nu=0$ and they will all remain so at all times, since their tendencies are zero at $t=0$.

From (4.1) it becomes transparent that in the presence of a non-zero shear, $\bar{u}(y)\neq 0$, the geostrophic balance and thus the zero-meridional velocity for the Kelvin wave are destroyed just after a few integration-time steps. This is through the build up of ν first, which feeds into ξ and then v because of the presence of the flux term $\frac{\partial \bar{u}}{\partial y}\frac{\partial u}{\partial x}$ in the ν equation that provides a non-zero flux at $t=0$ although initially we have $\xi=\nu=v=0$. Furthermore, the nature of this flux term suggests that higher-wavenumber waves and/or larger shear gradients will result in stronger deviations from meridional geostrophy and from the Kelvin wave-background solution.

4.2 Poor performance of the 2D central scheme

To discretize the relaxation system (4.1), we opt for the non-staggered second order central scheme because of its simplicity and its notoriety for handling easily and efficiently conservation laws with source terms [27, 31]. Consider

$$w_t + f(w)_x + g(w)_y = S(w).$$

Given a spatial and temporal discretization: $w(x_i, y_j, t_n) \approx w^n_{i,j}$, $x_i = i\Delta x$, $y_j = j\Delta y$, and $t_n = n\Delta t$ the non-staggered 2D central scheme for this generic balance law is given by

$$\begin{aligned} w^{n+1}_{i,j} &= \frac{1}{4}(w^n_{i-1,j-1} + w^n_{i+1,j-1} + w^n_{i-1,j+1} + w^n_{i+1,j+1}) \\ &+ \frac{1}{8}(w'^n_{i-1,j-1} - w'^n_{i+1,j-1} + w'^n_{i-1,j+1} - w'^n_{i+1,j+1}) \\ &+ \frac{1}{8}(\grave{w}^n_{i-1,j-1} - \grave{w}^n_{i-1,j+1} + \grave{w}^n_{i+1,j-1} - \grave{w}^n_{i+1,j+1}) \\ &- \frac{\lambda}{4}(f(w^{n+\frac{1}{2}}_{i+1,j-1}) - f(w^{n+\frac{1}{2}}_{i-1,j-1}) + f(w^{n+\frac{1}{2}}_{i+1,j+1}) - f(w^{n+\frac{1}{2}}_{i-1,j+1})) \\ &- \frac{\mu}{4}(g(w^{n+\frac{1}{2}}_{i-1,j+1}) - g(w^{n+\frac{1}{2}}_{i-1,j-1}) + g(w^{n+\frac{1}{2}}_{i+1,j+1}) - g(w^{n+\frac{1}{2}}_{i+1,j-1})) + \frac{1}{4\Delta x\Delta y} I_s(x_i, y_j) \end{aligned} \tag{4.3}$$

where $\lambda = \frac{\Delta t}{\Delta x}$ and $\mu = \frac{\Delta t}{\Delta y}$ and $\frac{1}{\Delta x}(.)'$ and $\frac{1}{\Delta y}(.)\grave{}$ represent the approximated numerical derivative in the x and y directions respectively which guarantee the Total Variation Diminishing (TVD) property, [27]. Here, we use the monotone centred limiter i.e.,

$$w'_{i+1,j} = MinMod\{2(w_{i+2,j} - w_{i+1,j}), \frac{1}{2}(w_{i+2,j} - w_{i,j}), 2(w_{i+1,j} - w_{i,j})\}.$$

For simplicity in exposition $w^n_{i,j}$ is used to represent both cell-averages and point wise values. The forcing term

$$I_s(x_i, y_j) = \int_{t^n}^{t^{n+1}} \int_{x_{i-1}}^{x_{i+1}} \int_{y_{j-1}}^{y_{j+1}} S(w(x, y, t))\, dydxdt \tag{4.4}$$

is handled by an explicit scheme of [31]. Recall that the mid-point values, $w^{n+\frac{1}{2}}_{i,j}$, are provided by the predictor step

$$w^{n+\frac{1}{2}}_{i,j} = w^n{}_{i,j} - \frac{\lambda}{2} f'^n_{i,j} - \frac{\mu}{2} \grave{g}^n_{i,j} + \frac{\Delta t}{2} S^n_{i,j}. \tag{4.5}$$

The derivatives are discretized by simple centred differences and incorporated into the source term. This does not seem to create any (unexpected) numerical instabilities. The resulting numerical scheme is tested for the shear-free Kelvin wave with wavenumber four, when the barotropic shear is zero. We use three different grid resolutions, 125×100, 250×200 and 500×400, on the periodic channel $[0, 10,000\text{km}] \times [-5000\text{km}, 5000\text{km}]$. Note that in order to reduce the computational cost and since the Kelvin wave is periodic with 4 period over the equator with length 40,000 km, we only use the [0,10,000 km] which is equivalent to one wave length of the wave. Up to two days integrating over time, the central scheme applied to the relaxation system behaves very nicely and, as expected, the zero meridional velocity and geostrophic balance were maintained exactly. It also displays a second order convergence, for the numerical error in u and θ, with respect to grid refinement shown in table 4.1.

Grids	u	v	θ
125×100	0.1560×10^{-2}	0.0000	0.1560×10^{-2}
250×200	0.3279×10^{-3}	0.0000	0.3279×10^{-3}
500×400	0.7725×10^{-4}	0.0000	0.7725×10^{-4}

Table 4.1: L_1-norm relative error between exact solution and the numerical solution obtained by the central scheme for relaxation system (4.2).

However, when the model is run for the long period of time of 50 days, the horizontal structure of the simulated 'Kelvin wave' solution (using the 2D-central scheme) for the relaxation system (4.2) is altered significantly. The associated contours of the zonal velocity u at time $t = 50$ days are shown on the right top panel in Figure 4.1 while the top left panel displays those of the exact solution. The difference is striking. After 50 days of integration time, the numerical solution adapts a heart-like shape topology. The bottom panels show the numerical solutions, at the same time and with the same resolution, obtained by the f-wave method (right) and the non-staggered 2D central scheme (left) applied to the original baroclinic equations (2.28), when the barotropic wind is zero. Recall that, due to discretization errors, both these schemes show some deviations from the meridional geostrophy and therefore develop a (weak but) non-zero meridional velocity, which potentially grows with time although not overwhelmingly with this resolution. The shape of the contours of u at 50 days is captured accurately with the f-wave method and the 2D central scheme, though, the

central scheme seems to suffer from a phase lag problem as it is noticed in [12].

Presented this way, the bad performance of the first simulation could be falsely attributed to the choice of the relaxation system but a close look at this system shows that with $v = q = r = 0$ and $\theta = -u$ at $t = 0$, it reduces to the two identical one-dimensional advection equations $u_t + u_x = 0$ and $\theta_t + \theta_x = 0$ whose numerical solution for u, displayed in Figure 4.1, is clearly not the expected one. Therefore, we conclude that this bad performance is due to the 2D central scheme. It is shown by a systematic analysis below that the 2D central scheme suffers from a severe distortion of the numerical propagation speed, in the zonal direction, for the Kelvin wave so that off equatorial parts of the wave move faster than the equatorial crest. It is interesting though to notice that the same central scheme applied to the original baroclinic equations (2.28) does not seem to have this problem. This is probably due to some sort of compensation from the "artificial" deviation from meridional geostrophy.

4.3 Analysis of poor dispersion properties of the 2D central scheme

Here, we explain the distortion of the Kelvin wave structure for a long period integration over time obtained by the 2D non-staggered central scheme. We consider the simple one-dimensional advection equation

$$u_t + au_x = 0, u(x, y, 0) = \cos(kx)\Gamma(y) \tag{4.6}$$

which for $\Gamma(y) = e^{-y^2/2}$ effectively represents the evolution of the Kelvin wave. Assume that the 2D non-staggered central scheme (4.3) is applied to this equation with the *minmod* limiter turned off. We approximate the xy slopes with their centred differences i.e., $\frac{1}{\Delta x}u'_{i,j} = \frac{1}{2\Delta x}(u_{i+1,j} - u_{i-1,j})$ and $\frac{1}{\Delta y}\grave{u}_{i,j} = \frac{1}{2\Delta y}(u_{i,j+1} - u_{i,j-1})$, respectively. Notice that this is a reasonable assumption since the solution is very smooth; there are no shocks. So, the 2D central scheme for the unidirectional advection equation

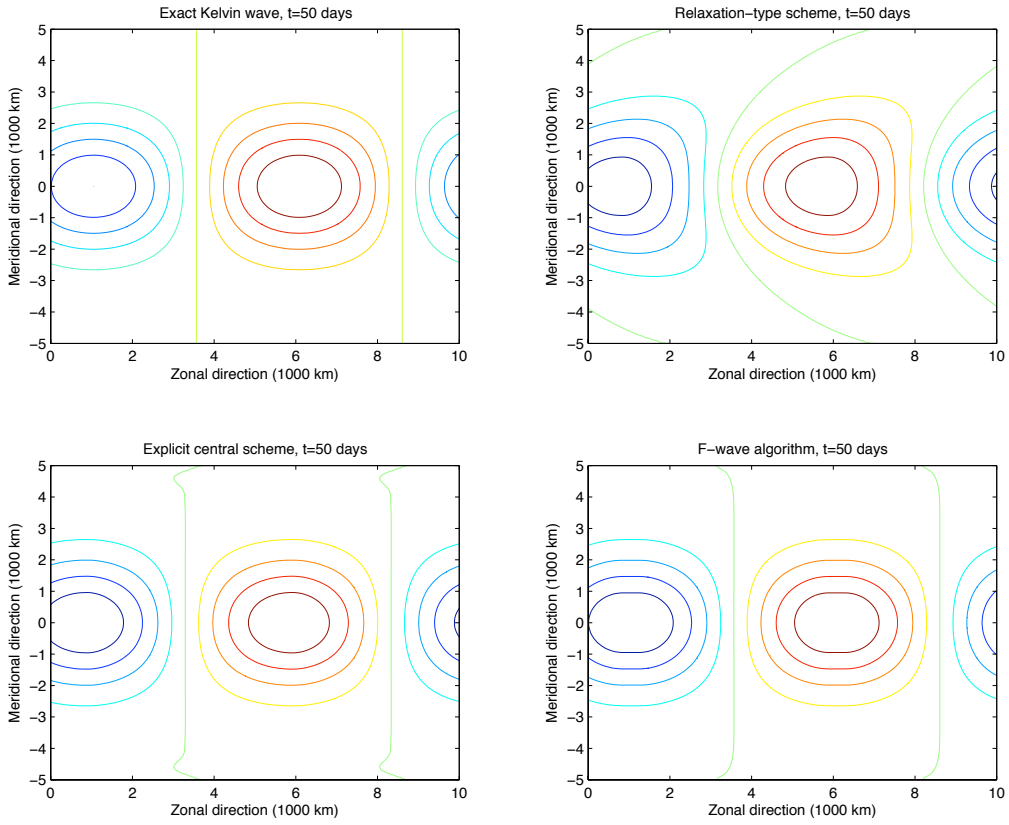

Figure 4.1: Contours of u at 50 days of the model run time for the Kelvin wave: Exact solution (top left), non-staggered 2D central scheme for the relaxation system (4.1) with $\bar{u} = 0$ (top right), f-wave method for the original baroclinic system (2.28) with $\bar{u} = \bar{v} = 0$ (bottom right), and non-staggered 2D central scheme for original baroclinic system (2.28) with $\bar{u} = \bar{v} = 0$ (bottom left). The grid resolution is 500×400 and a time step $\Delta t = 0.22$ hours. The axis labels are in 1000 km.

becomes

$$
\begin{aligned}
u_{i,j}^{n+1} = & \frac{1}{4}[u_{i-1,j-1}^n + u_{i-1,j+1}^n + u_{i+1,j-1}^n + u_{i+1,j+1}^n] \\
& -\frac{1}{16}[u_{i-2,j-1}^n - 2u_{i,j-1}^n + u_{i+2,j-1}^n + u_{i-2,j+1}^n - 2u_{i,j+1}^n + u_{i+2,j+1}^n \\
& + u_{i-1,j-2}^n - 2u_{i-1,j}^n + u_{i-1,j+2}^n + u_{i+1,j-2}^n - 2u_{i+1,j}^n + u_{i+1,j+2}^n] \\
& -\frac{a\lambda}{4}[u_{i+1,j-1}^n - u_{i-1,j-1}^n + u_{i+1,j+1}^n - u_{i-1,j+1}^n] \\
& +\frac{a^2\lambda^2}{16}[u_{i+2,j-1}^n - 2u_{i,j-1}^n + u_{i-2,j-1}^n + u_{i+2,j+1}^n - 2u_{i,j+1}^n + u_{i-2,j+1}^n].
\end{aligned}
\tag{4.7}
$$

Notice that the expression containing $a^2\lambda^2$ is derived by plugging the predictor step (4.5) into the corrector step (4.3) which gives the second order accuracy. We consider plane wave solution

$$u_{ij}^n = \rho^n e^{I(kx_i - \omega t_n)}\Gamma(y_j) \tag{4.8}$$

where $I^2 = -1$ and $\rho > 0$ is the wave amplitude, in the manner of von Neumann analysis [4]. Plugging in this ansatz into (4.7), yields

$$\begin{aligned}\rho[\cos(w_r\Delta t) - i\sin(w_r\Delta t)]\Gamma(y_j) &= \frac{1}{2}\cos(k\Delta x)[\Gamma(y_{j-1}) + \Gamma(y_{j+1})] \\ &+\frac{1}{8}[(1-\cos(2k\Delta x))[\Gamma(y_{j-1}) + \Gamma(y_{j+1})] - \cos(k\Delta x)[\Gamma(y_{j-2}) - 2\Gamma(y_j) + \Gamma(y_{j+2})]] \\ &-\frac{a\lambda}{2}i\sin(k\Delta x)[\Gamma(y_{j-1}) + \Gamma_(y_{j+1})] + \frac{a^2\lambda^2}{8}[(\cos(2k\Delta x) - 1)][\Gamma(y_{j-1}) + \Gamma(y_{j+1})].\end{aligned}$$

The advection velocity a is normalized to $a = 1$, for simplicity. Let $P(y_j) = \Gamma(y_{j-1}) + \Gamma(y_{j+1})$, $Q(y_j) = \Gamma(y_{j-2}) - 2\Gamma(y_j) + \Gamma(y_{j+2})$,

$$W(y_j) = \frac{1}{2}\cos(k\Delta x)[P(y_j) - \frac{1}{4}Q(y_j)] + \frac{1}{8}P(y_j)(1-\cos(2k\Delta x))(1-\lambda^2))$$

and

$$V(y_j) = \frac{\lambda}{2}\sin(k\Delta x)P(y_j).$$

Then, the phase speed and growth rates of the plane wave solution are given by

$$\frac{\omega}{k} = \frac{1}{k\Delta t}\arctan(\frac{V}{W}) \tag{4.9}$$

and

$$\rho = \frac{\sqrt{V^2 + W^2}}{|\Gamma(y_j)|}. \tag{4.10}$$

The y-structures of the phase speed and growth rate in (4.9) and (4.10) are plotted in Figure 4.2 for $\Gamma(y) = e^{-y^2/2}$ (top panels) and $\Gamma(y) = \sin(\pi y/5)$ (bottom panels). It is obvious from the figure that unlike the case where $\Gamma(y) = \sin(\pi y/5)$, when $\Gamma(y) = e^{-y^2/2}$ both the growth rate and the phase are highly dependent on y. From the top panels, we see that for the Kelvin wave, at least initially, the central scheme tends to damp slightly the solution at the equator and amplify it off the equator, at the inflection points of $e^{-y^2/2}$. Moreover, the wave structure moves at a faster speed off the equator and slower near the equator, below roughly the deformation-radius turning point. It is important to note that variations in the growth rate with latitude,

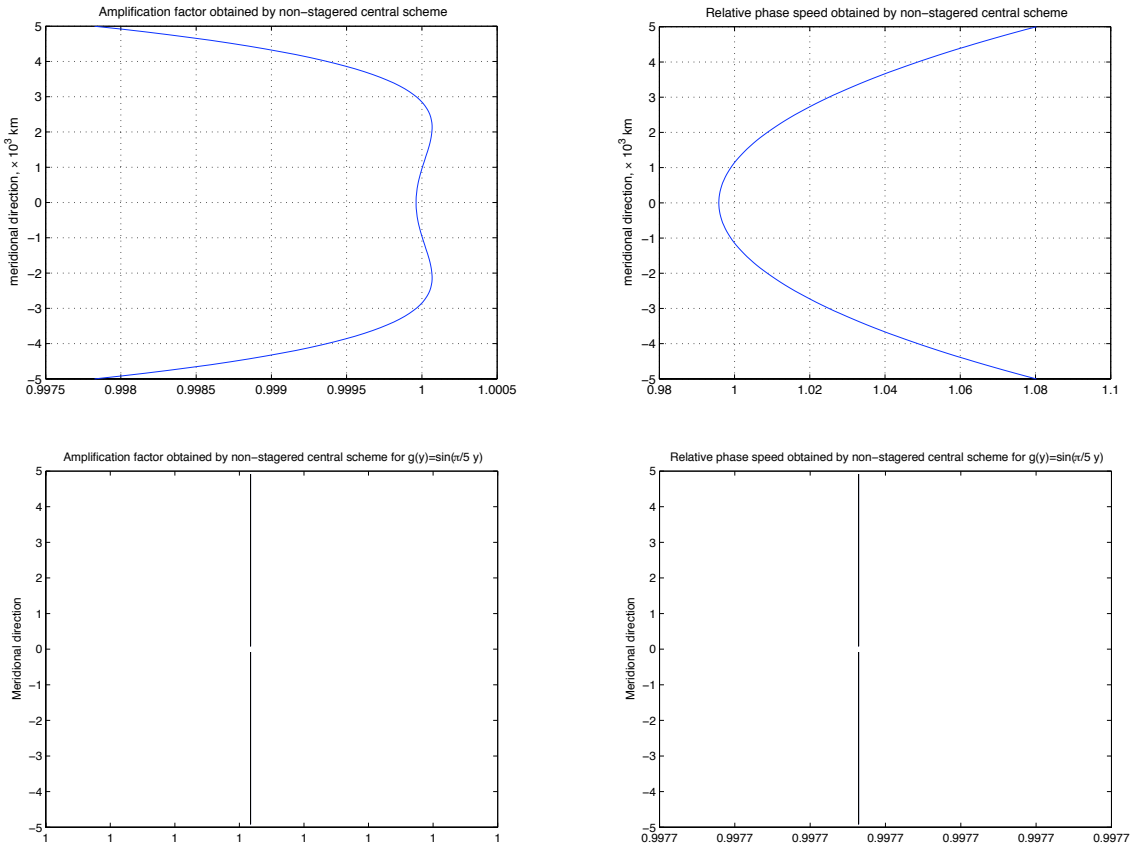

Figure 4.2: Phase speed (right) and growth rate (left) as functions of the distance from the equator, y, for the 2D central scheme applied to the uni-directional advection equation in (4.6) with $\Gamma(y) = e^{-y^2/2}$ (top) and $\Gamma(y) = \sin(\pi y/5)$ (bottom).

between -2000 km and 2000 km do not exceed 5/10,000, while variation in phase speed, over the same meridional span, is on the order of 2/100. Clearly, it is this y-dependence of the growth rate and especially the phase speed that is responsible for the distortion of the structure of the Kelvin wave solution in Figure 4.1.

In order to understand how the non-uniform phase speed and non-uniform growth rate distort the Kelvin wave structure, we attempt to reconstruct the numerical solution, associated with the scheme (4.7), from the plane wave ansatz in (4.8), with ρ and ω given explicitly by (4.9) and (4.10), respectively. However, since the y-structure of the numerical solution changes constantly with time this is a tricky game. Nevertheless, to appreciate the individual contribution from the phase speed and growth rate, separately, to this wave distortion, we evolve the plane wave solution upto $t_n = 50$ days, according to the iterative scheme

$$\begin{aligned} u_{n+1}(x,y) &= \cos\left(kx - \Delta t S_{n+1}(y)\right)\Gamma_{n+1}(y), n \geq 0 \\ S_{n+1}(y) = \sum_{l=0}^{n} \omega_n(y), &\quad \Gamma_{n+1}(y) = \Gamma_0(y)\prod_{l=0}^{n}\rho_l(y), \\ u_0(x,y) &= \cos(kx)\Gamma_0(y), \quad \Gamma_0(y) = e^{-y^2/2} \end{aligned} \tag{4.11}$$

with ω_l and ρ_l given by either

i) **Varying amplification factor alone:**
$\rho_l(y) = \rho_0(y)$ with $\rho_0(y)$ given by (4.10) and $\omega_l(y) = 1$, for all $l \geq 1$,

ii) **Varying phase speed alone:**
$\rho_l = 1$ and $\omega_l(y) = \omega_0(y)$ with $\omega_0(y)$ given by (4.9) for all $l \geq 1$,

iii) **Varying both phase speed and growth rate:**
$\omega_l(y) = \omega_0(y)$ and $\rho_l(y) = \rho_0(y)$ where $\omega_0(y)$ and $\rho_0(y)$ are given, respectively, by (4.9) and (4.10) for all $l \geq 1$.

The resulting solutions are plotted in Figure 4.3, with the top panel displaying the contours of $u_n(x,y)$ at $n\Delta t = 50$ days associated with the Case (i) of varying the amplification factor only, the middle one corresponds to (ii) where only the phase speed varies and the bottom panel is associated with Case (iii) where both ω and ρ are varied. Notice that with Choice (iii) the iterative scheme (4.11) mimics closely the difference scheme in (4.7). Clearly from this picture, the distortion effect is due

to a differential phase speed that is predominant which is the fact that off equator parts of the wave move relatively faster. However, the amplification factor variation with y merely expands the solution in the meridional direction due to the fact that the solution is damped at the equator, amplified off the equator upto $y = \pm 3$ and again damped afterwards.

A strategy to overcome the wave distortion caused by using the 2D central scheme for (2.28) or such wave problems is to use the one-dimensional central scheme compounded through dimensional splitting explained in section (3.1). This way, the advection in the x-direction does not include the averaging or dependency on y-direction which will avoid the problem. The numerical solution obtained by the dimensional splitting is presented in Figure 4.3 which shows the improvement of the wave deformation. However, with a close look you notice that the solution still has a phase lag which is an unavoidable feature of the central scheme as seen in [12].

4.4 Interactions of Kelvin waves and easterly barotropic shear

We showed that the 2D second order central scheme is not an appropriate scheme to be used for the equatorial waves. Thus, we apply the f-wave algorithm to study Kelvin waves in the equatorial easterly shear background. We initialize the state variables in (2.28) to the Kelvin wave solution at time $t = 0$ and integrate the system numerically in time. The grid size is 250×200 for the periodic channel and the time step is set to $\Delta t = 0.5 \min(\Delta x, \Delta y)$ to satisfy the CFL condition.

The numerical solutions are shown in Figure 4.5. In this experiment, the length of the domain is fixed to 4000 km corresponding to Kelvin wave with wavenumber $k = 10$. The solution is shown at one day intervals during the first 5 days of simulation. From these results, we see clearly that the interactions of the Kelvin wave with this shear induces non-trivial and interesting dynamics. Both the shape of θ and u contours and also the flow itself undergo some complicated changes with an apparent oscillation. This can not be explained by the advection effects alone. An important aspect, relevant for convectively coupled waves, is the emergence of a non-zero meridional velocity which enforces the zonal convergence and the upward motion as a consequence.

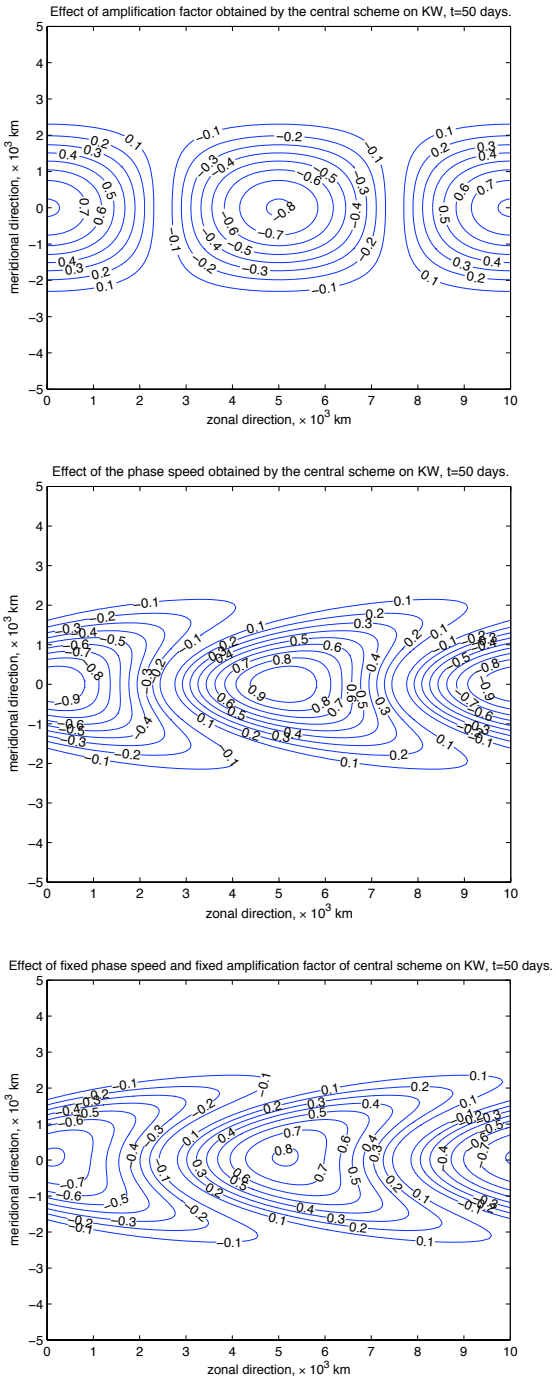

Figure 4.3: Contours of the wave solution $u_n(x, y)$ obtained by the iterative process (4.11) with $n = 5400$ and $\Delta t = 0.22$ hours corresponding to the solution at $t = 50$ days as in Figure 4.1. Top: effect of varying amplification factor alone, middle: effect of varying phase speed alone, bottom: varying amplification factor and varying phase speed combined (see text for details).

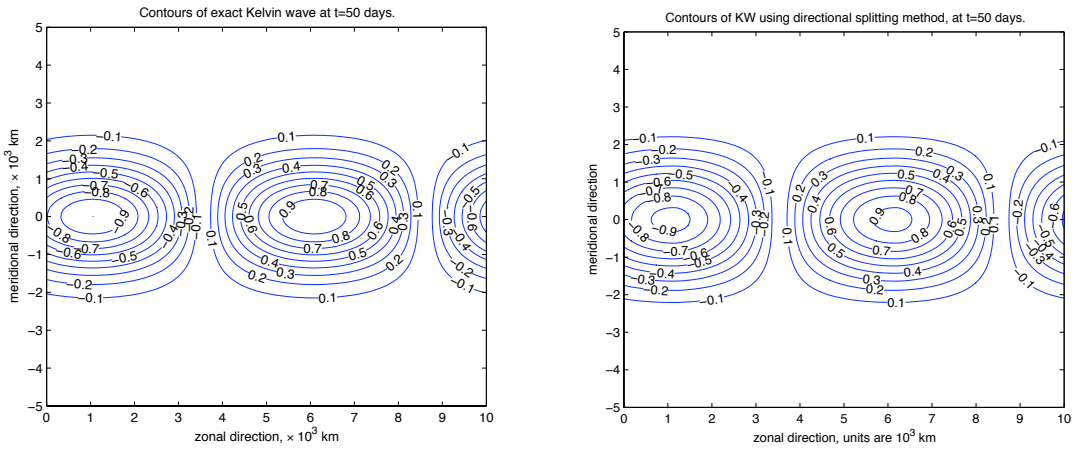

Figure 4.4: Contours of u at 50 days of the model run time for the Kelvin wave: exact solution (left), approximated solution obtained by dimensional splitting and non-staggered central scheme of the relaxation system (4.1) for with $\bar{u} = 0$ (right). The grid resolution is 500×400 and the time step $\Delta t = 0.22$ hours. The axis labels are in 1000 km.

As it is anticipated from the relaxation system (4.1), the build up of the meridional velocity is due to the meridional shear, $\bar{u}_y(y)$, and the zonal gradient of the waves $u_x(x, y, t)$ which are the wavenumbers. In Figure 4.6, we show the flow structures for three different wavelengths, namely different wavenumbers, $k = 1, k = 4$ and $k = 10$ at $t = 2$ days. Consistent with the intuition, the deformation is greater at larger wavenumbers.

In Figure 4.7 the time series of the relative meridional wind (left panels) and relative meridional convergence $\max(-v_y(x, y))/\max(-u_x(x, y) - v_y(x, y))$ (right panel) are plotted for these different wavenumbers for time period of 50 days. Interestingly, while the meridional velocity seems to increase significantly with increasing wavenumber, the strength of the meridional convergence exhibits roughly the same range of oscillations, between 10 % to 40%. Nevertheless, the period and strength of these oscillations change quite a lot with the wavenumber. For $k = 1$ and $k = 4$, we have a clear cut between low frequency oscillations of about 7 to 10 days period, superimposed on top of higher frequency modes oscillating rapidly with a period of about 1 day or so. The high frequency oscillations seem to amplify greatly as the wavenumber is increased, at $k = 10$, the low-frequency mode gets blurred and becomes somewhat

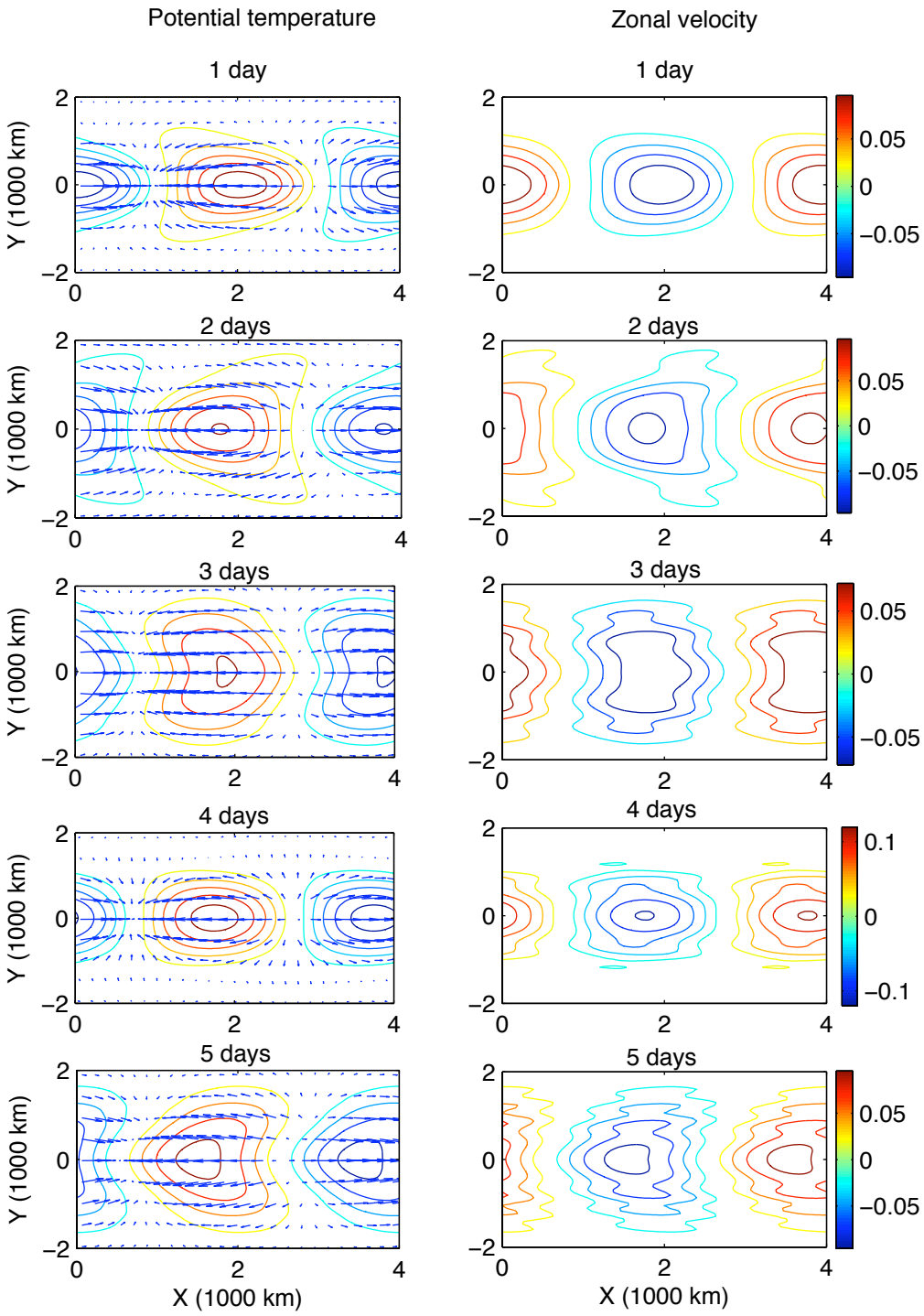

Figure 4.5: Flow velocity field overlaid on the contours of the potential temperature, θ, (left) and contours of zonal velocity, u, (right) for the Kelvin wave forced by the easterly barotropic shear. The wave wavelength (domain size) is 4000 km and the solution is shown at times $t = 1$ day, $t = 2$ days, $t = 3$ days, $t = 4$ days and $t = 5$ days (from top to bottom).

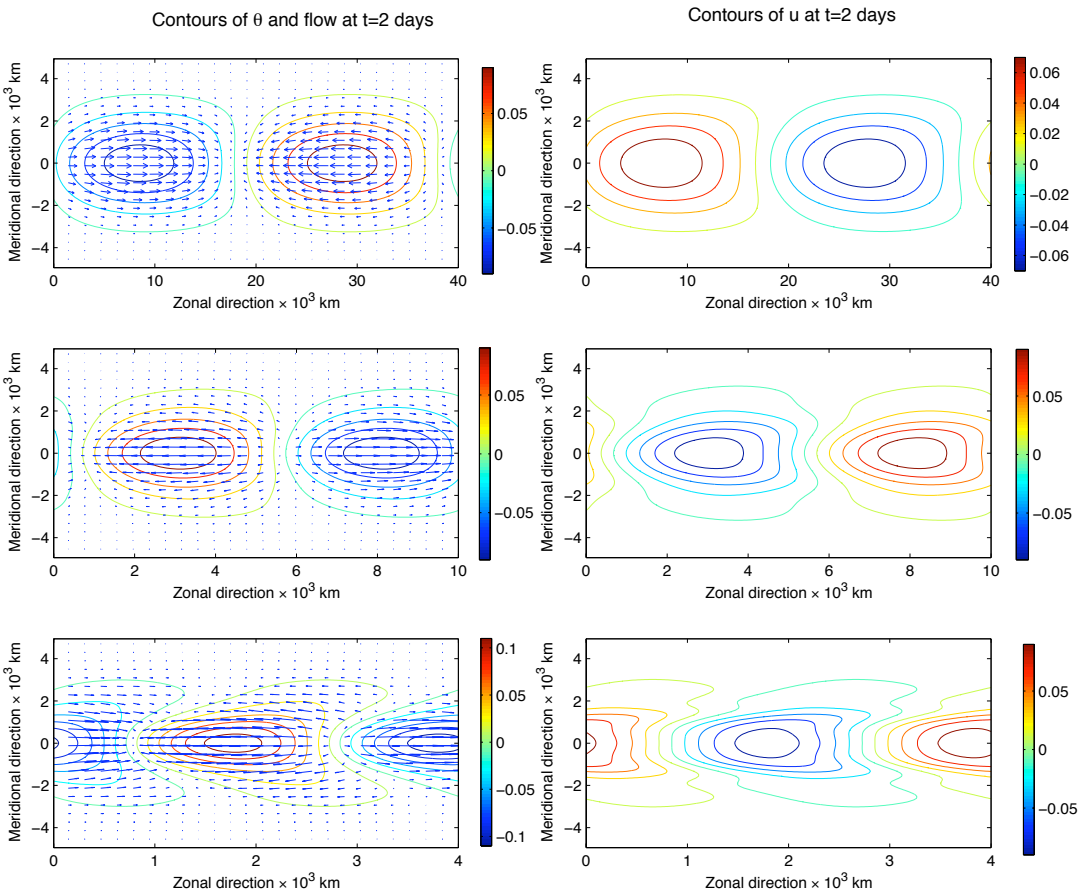

Figure 4.6: Flow velocity field overlaid on the contours of the potential temperature, θ, (left) and contours of zonal velocity, u, (right) for the forced Kelvin wave by the easterly shear at time $t = 2$ days and for different wavelengths: 40,000 km (top), 10,000 km (middle), and 4000 km (bottom).

indistinguishable.

An interesting question to ask is what kind of physical mechanisms are responsible for the oscillations in Figures 4.6 and 4.7. According to previous work by Webster and others [39, 40], a meridional shear has very little effect on the Kelvin waves. Clearly what is happening here is not a simple matter of deformation by wind advection. We show further on, in chapter 6, that these strong oscillations are due to the excitement of other equatorially trapped waves of different strength through the interaction between the Kelvin wave and the shear flow. In addition detailed spectral

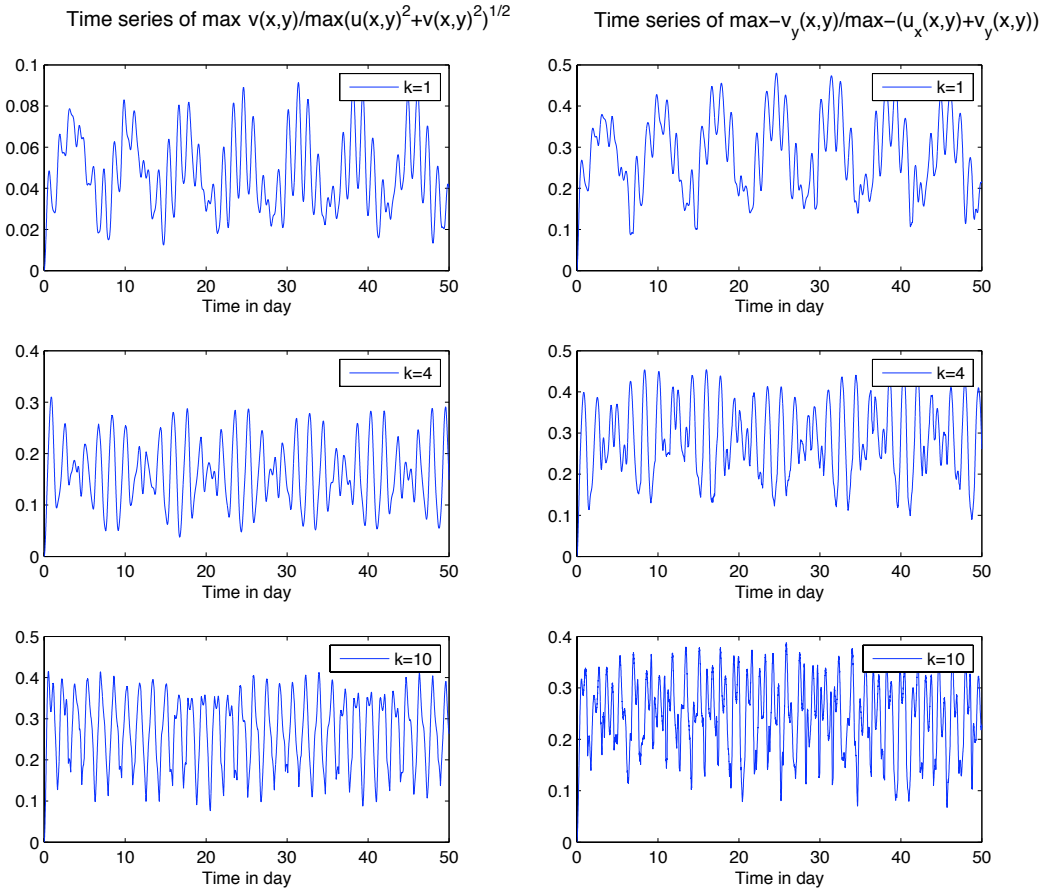

Figure 4.7: Time series of the relative meridional wind (left) and relative meridional convergence (right). Wavenumbers: $k = 1$ (top), $k = 4$ (middle), and $k = 10$ (bottom).

analysis which reveals the nature of such waves is demonstrated.

4.5 Summary

In this chapter, we studied the Kelvin waves in the presence of easterly shear which possess the zero meridional velocity and the meridional geostrophy, $\frac{\partial \theta}{\partial y} + yu$. However, we required a numerical scheme which preserves these quantities for the shear-free case and suppresses small deviations from steady state. To achieve this, we introduced the relaxation scheme for which any conservative schemes preserve the geostrophic balance and the zero meridional velocity of the Kelvin waves.

We applied the 2D second order central scheme to test the performance of the scheme for a shear-free Kelvin wave for a long run, 50 days. We showed that the central scheme distorts the structure of waves and we verified this deformation through a systematic analysis. Therefore, to present the interaction of the Kelvin waves with the shear we applied the f-wave algorithm to System (2.28). Note that it is difficult to perform the f-wave algorithm for the relaxation system therefore, we used it for System (2.28). We showed that the Kelvin wave exhibits a weak meridional velocity which nevertheless contributes to convergence and divergence regions. This effect is more significant for larger wavenumbers and/or stronger shear gradient.

Finally, we finish this chapter by emphasizing that extra caution should be taken when using the 2D central scheme for atmospheric modelling which may give inadequate results as seen for equatorially Kelvin waves. We anticipate that the danger persists especially if this scheme is used to advect a tracer in the direction that has a complex structure in the perpendicular direction, here $\exp(\frac{-y^2}{2})$. It can occur for example for moisture or liquid water fields that are associated with a convectively coupled equatorial wave, which propagate along and are trapped in the vicinity of the equator.

Chapter 5

Equatorially trapped waves in a background shear

In this chapter, we present the properties of equatorially trapped waves in a shear, consisting of both an equatorial easterly and an equatorial westerly wind, Figure 2.3. We apply Galerkin projection to System (3.26) in the meridional direction by using $N = 9$ parabolic cylinder functions. This allows us to study and compare the results for this advected system by using linear theory and also integrating over time to capture the dynamical interactions. The Galerkin projection is chosen for three advantages of this scheme over the two others. The first advantage is that we avoid artificial boundary conditions in the meridional direction since this projection leads to one dimensional advection equations in x, for which we use periodic boundary conditions in the zonal direction. It is also convenient for linear analysis where we can easily test the effect of different parameters such as, wavenumber, shear strength and so on. Moreover, compared to the f-wave algorithm and the 2-D central scheme, it is more efficient.

In the first section, we do a linear analysis of this system by assuming wavelike solutions that travel zonally along the equator. We compare the frequencies and the meridional structures of these waves with their shear-free analogues. In the second section, we evolve this one dimensional advected system in time by using the second order central scheme to capture the dynamical interaction of the equatorial waves with the imposed shears. In the third section, we consider the case of a Kelvin wave in an asymmetric shear, which shifts the convergence/divergence regions for

the Kelvin wave and also excites other symmetric and also anti-symmetric equatorial waves whose structures resemble observations.

5.1 Linear analysis of equatorial waves in a background flow

We consider the projected system (3.26):

$$\frac{\partial \tilde{W}}{\partial t} + A\frac{\partial \tilde{W}}{\partial x} + (B+C)\tilde{W} = 0$$

and since we are looking for wavelike solutions, we assume

$$\tilde{W}(x,t) = \hat{W}\exp(i(kx - \omega t)), \tag{5.1}$$

where $i^2 = -1$, k is the zonal wavenumber and ω is the frequency. This leads to solving

$$\big[(kA - i(B+C)) - \omega I\big]\hat{W} = 0, \tag{5.2}$$

which requires us to find the eigenvalues $\omega(k)$ and eigenvectors $\hat{W}$ for the matrix $D = kA - i(B+C)$. Since the barotropic shear is symmetric in meridional direction, we can decouple system (5.2) into a symmetric sub-system and an anti-symmetric sub-system, which helps identify the associated equatorial waves easily. Note that in the presence of a uniform wind, $\bar{u}(y) = \bar{u}_0$, the solutions of this system are the equatorially trapped waves but with Doppler-shifted frequencies $\hat{\omega} = \omega - k\bar{u}_0$ due to the imposed shear background.

5.1.1 Frequency

In addition to the real value frequencies, depending on the values of $\bar{u}_0$ and/or k, the matrix D may have complex eigenvalues. Let $\omega = \omega_r + i\omega_i$, then the wave solution in (5.1) becomes

$$\tilde{W}(x,t) = \hat{W}\exp(\omega_i t)\exp(i(kx - \omega_r t)), \tag{5.3}$$

where $\exp(\omega_i t)$ is the wave growth and ω_r is the wave phase. Therefore, the waves become unstable and grow if $\omega_i \geq 0$ or damp and vanish if $\omega_i \leq 0$. This will be discussed further later in this chapter. The real value of the eigenfrequencies of the

equatorial waves in the easterly flow (EE) and in the westerly flow (WE) are shown in Figures 5.1 and 5.2, respectively. These eigenfrequencies include the Doppler effect by the shear, because there is no obvious way to derive the relative frequencies explicitly in the moving frame.

For the Kelvin waves, the eigenfrequencies are larger in EW but smaller in EE compared to their shear-free analogues. For the eastward gravity waves in both shears, the frequencies increase for larger wavenumbers and decrease for smaller wavenumbers and the frequencies are highly dependent on the meridional index, M. However, for westward gravity waves the eigenfrequencies decrease independent of the wavenumbers and/or meridional index. The results for Rossby waves are striking. We will show in Chapter 6 that the Rossby waves are highly affected in the shear environment. This might be explained by the fact that Rossby waves are low-frequency waves and perhaps they become highly affected by a strong shear. Moreover, Zhang and Webster in [43] explained that the equatorial Rossby waves are much more susceptible to shear because they rely primarily on the potential vorticity gradient for their existence.

In the presence of EE, the Rossby waves for both symmetric and anti-symmetric cases are stable and have real eigenvalues; however, some waves propagate eastward rather than westward which is the propagation direction of the shear-free Rossby waves. In EW background, two symmetric and one anti-symmetric Rossby waves become unstable and their complex eigenfrequencies are conjugates of each other. In EE, the eigenfrequencies of the westward mixed Rossby-gravity waves (MRG) are smaller for $k \leq 7$ and are greater for larger wavenumbers compared to the eigenfrequencies of the shear-free cases. However, the westward MRGs become unstable in EW. These results are consistent with the fact that the properties of the eastward MRG waves resemble the properties of the eastward gravity waves while the properties of westward MRG waves resemble the properties of the Rossby waves.

In Figure 5.3, we present the frequencies of the equatorial waves in the easterly shear background with different strengths, $\bar{u}_0 = 1, 3$ and 5 m/s. This figure shows a smooth change of their frequencies toward the shear-free waves and also it shows the stronger the shears are, the more affected the equatorial waves are.

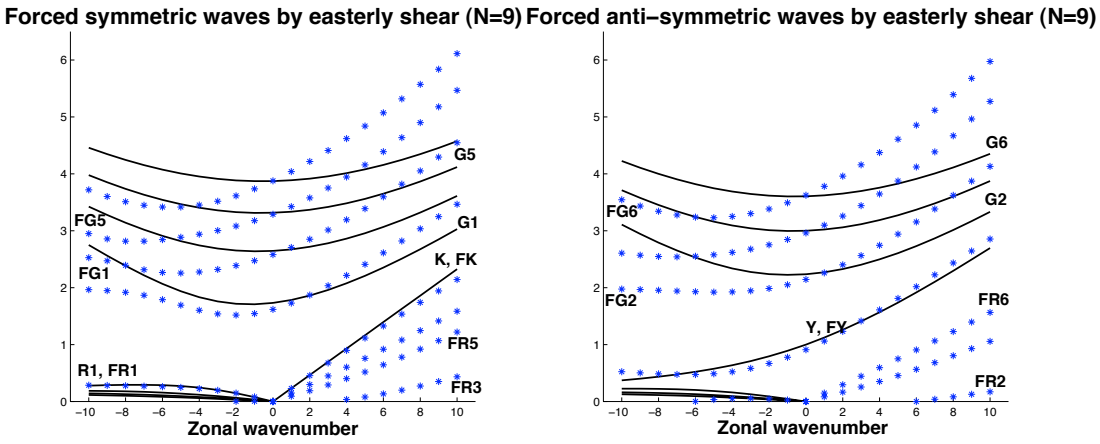

Figure 5.1: Eigenfrequencies of symmetric (left panel) and anti-symmetric (right panel) equatorial waves; in no flow (solid lines) and EE (stars) background.

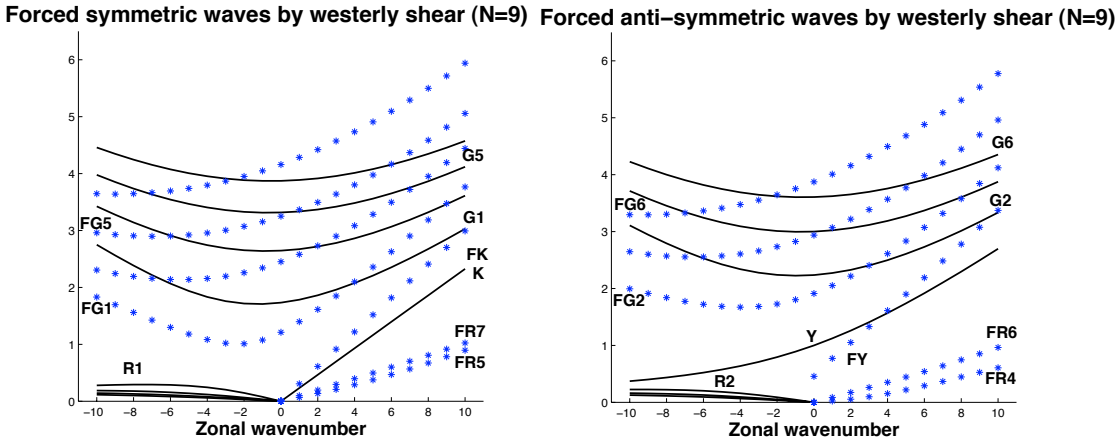

Figure 5.2: Eigenfrequencies of symmetric (left panel) and anti-symmetric (right panel) equatorial waves; in no flow (solid lines) and EW (stars) background.

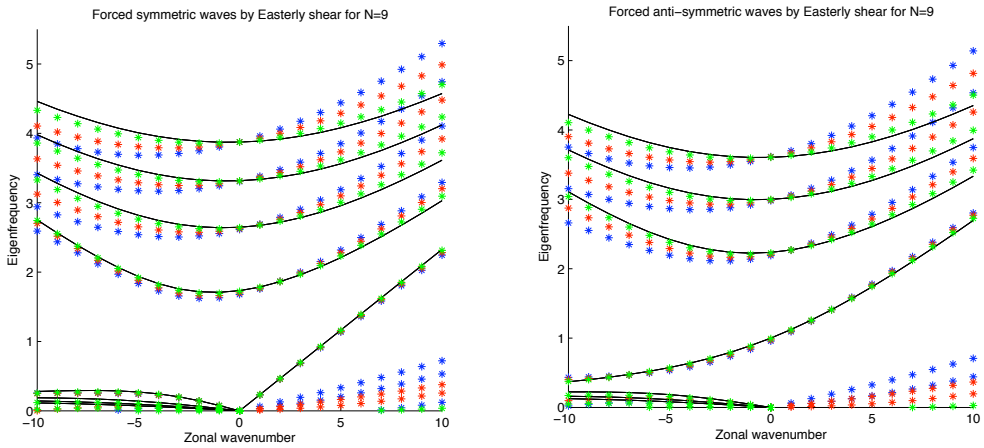

Figure 5.3: Eigenfrequencies of symmetric (left panel) and anti-symmetric (right panel) equatorial waves for different shear strength; no flow (solid lines), $\bar{u}_0 = 5$ m/s in blue, $\bar{u}_0 = 3$ m/s in red, and $\bar{u}_0 = 1$ m/s in green.

5.1.2 Unstable equatorial waves

Here, we characterize the unstable waves in the westerly background shear. The frequencies of the unstable waves are conjugates; therefore, from equation (5.3), one wave grows while the other one vanishes over time but they both propagate with the same phase speed. We show the phase and the growth of the unstable Rossby waves and westward MRG waves in this shear environment in Figure 5.4, which suggests that the growth factor initially increases up to a certain wavenumber and then decreases whereas the speed of propagation increases as the wavenumber increases.

Here, we show and emphasize the fact that the strength of the westerly shear and the wavenumber play important roles in the growth, phase speed and direction of propagation of these unstable waves. We present these dependencies in Figure 5.5, where we compare the phase speed and the growth of the symmetric waves, top panels, and the anti-symmetric waves, bottom panels, for different shear strengths. Both growth and phase speed increase with increasing shear strength and also the direction of propagation of the waves alters in strong shears, i.e., the initially westward waves propagates eastward, Figures 5.5 and 5.7.

We display the growth for a wider range of wavenumbers in different shear strengths in Figure 5.6. It is shown that as the wavenumber increases, the growth increases

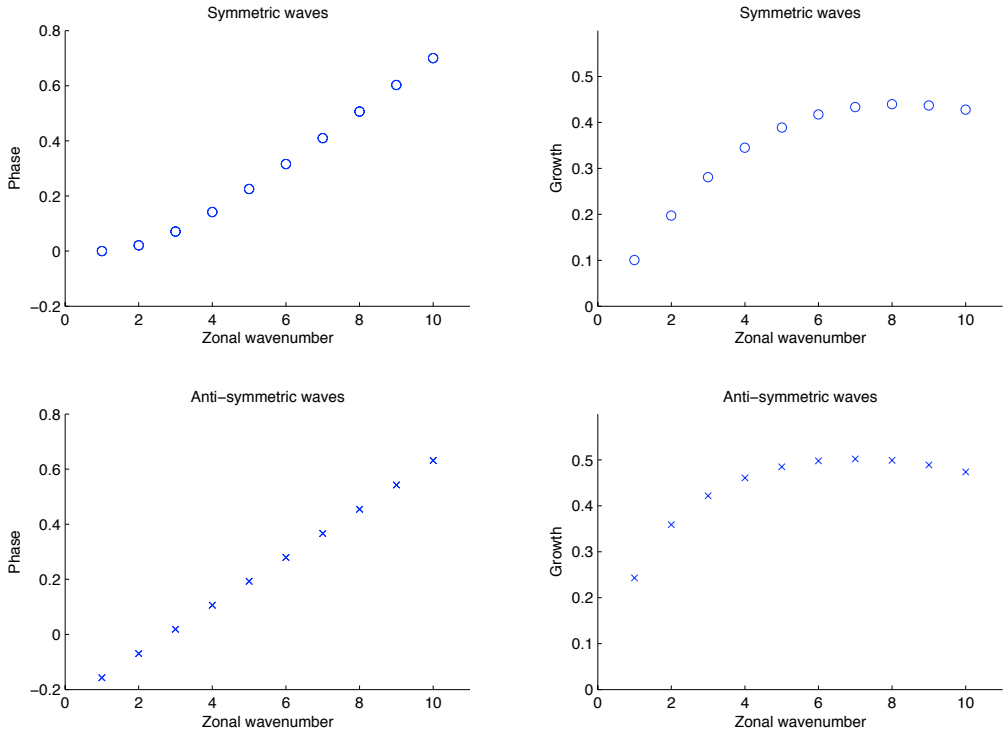

Figure 5.4: phase and growth factor for symmetric unstable waves, top panels, and for anti-symmetric waves, bottom panels, for different wavenumbers with $\bar{u}_0$=10 m/s.

up to a certain wavenumber after which it decreases. Moreover, as the wavenumber reaches a critical value, $17 \leq k \leq 20$ depending on the shear strength, the unstable waves become stable. However, for stronger shears, here $\bar{u}_0 = 8$ and 10, the waves become unstable again for much larger wavenumbers. We also plot the maximum growth of unstable waves for different wavenumbers in Figure 5.7, which implies that there is a linear relation between the shear strength and the maximum growth.

We compare the meridional structures of the stable waves with their shear-free counterparts. We do this for both stable and unstable waves, see Figures 5.8 and 5.9. This way we can identify the unstable waves because they are the ones missing from the waves. Note that M and N are used interchangeably for meridional mode numbers in the text and figure captions. In Figure 5.8, we present the meridional structures of the symmetric shear-free $M = 1, 3, 5$ and 7 Rossby waves with the obtained symmetric stable waves. The structures of the stable waves resemble the $M = 5$ and 7 Rossby waves but are more trapped. So, the unstable symmetric waves are Rossby waves of

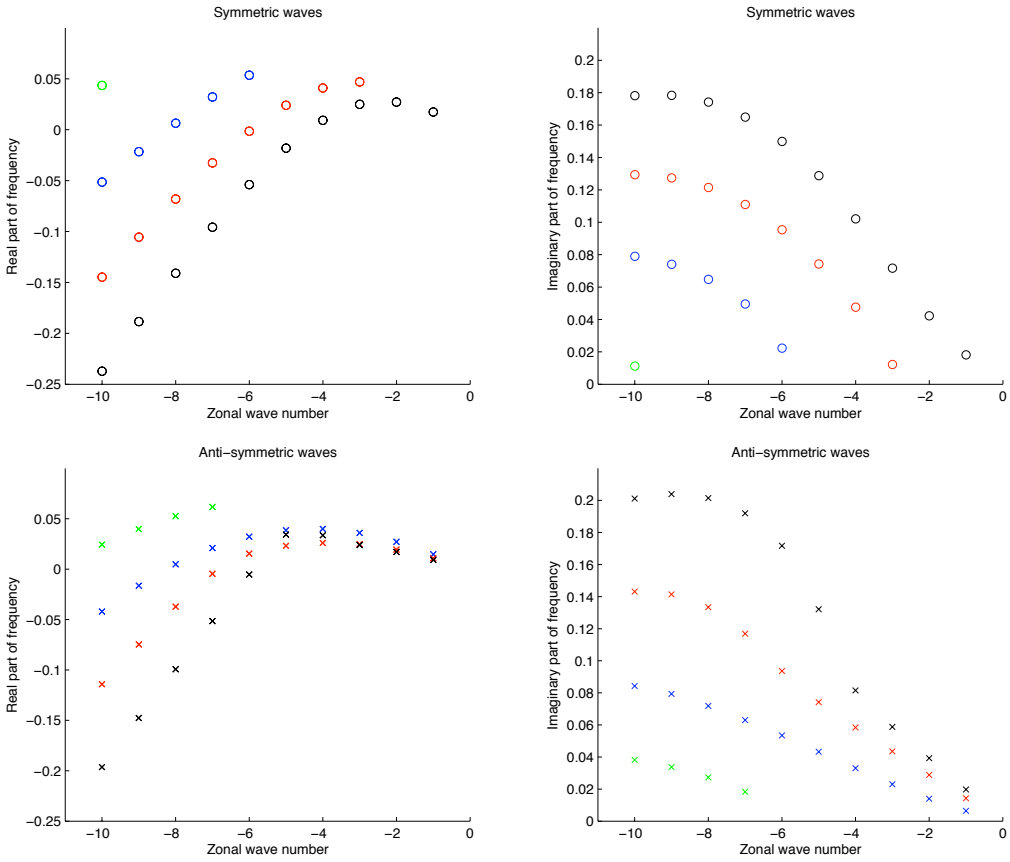

Figure 5.5: Growth and phase speed of unstable symmetric waves, top panel, and anti-symmetric waves, bottom panels, for different shear strength, green $\bar{u}_0 = 2$, blue $\bar{u}_0 = 3$, red $\bar{u}_0 = 4$ and black $\bar{u}_0 = 5$ the frequencies.

lower modes $M = 1$ and 3. By a similar comparison, the MRG waves and $M = 2$ Rossby waves are the unstable anti-symmetric waves in the westerly shear, Figure 5.9. Since the eigenvectors of conjugate pairs are equal we use the meridional structure of the waves to identify the unstable ones rather than using the eigenvectors.

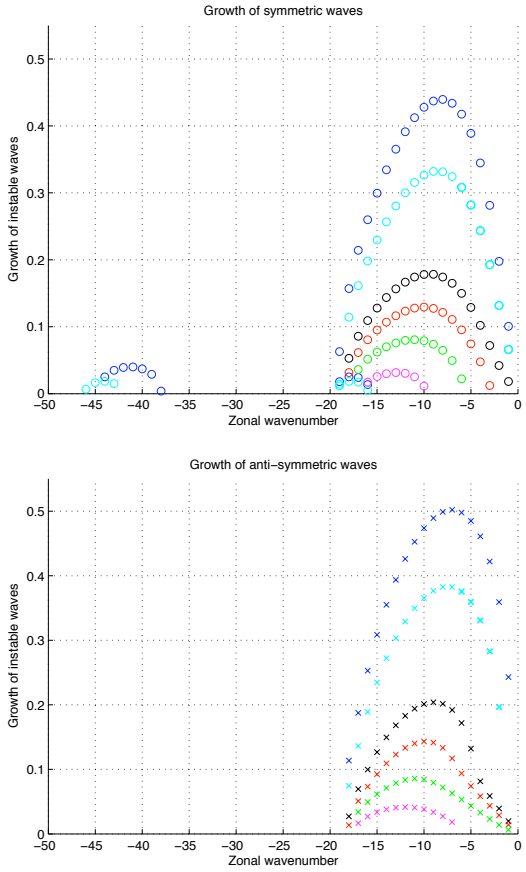

Figure 5.6: Growth of unstable waves, symmetric waves on the left panel and anti-symmetric waves on the right panel, for different shear strength, $\bar{u}_0 = 2$ in pink, $\bar{u}_0 = 3$ in green, $\bar{u}_0 = 4$ in red, $\bar{u}_0 = 5$ in black, $\bar{u}_0 = 8$ in cyan and $\bar{u}_0 = 10$ in blue for different wavenumbers.

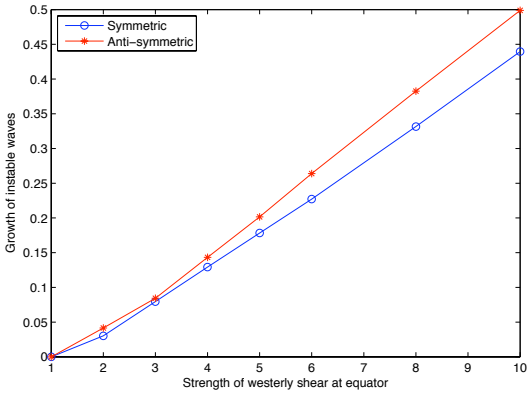

Figure 5.7: Maximum growth of unstable waves for different shear strength at equator.

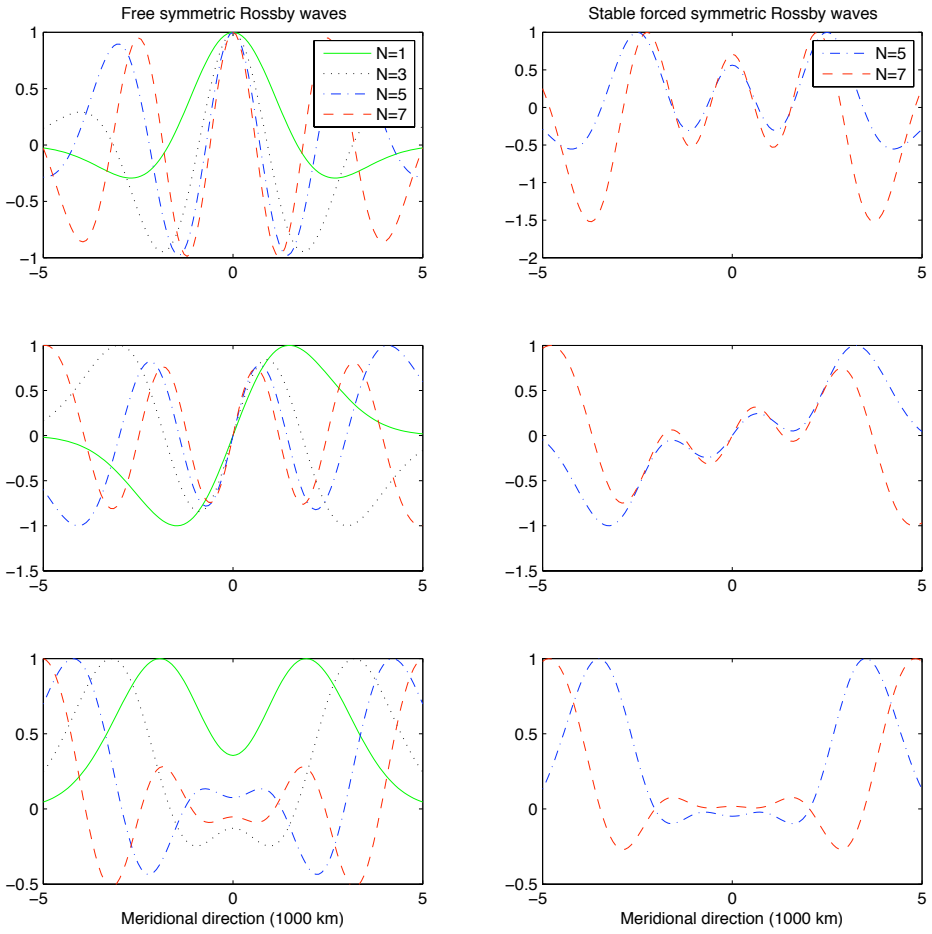

Figure 5.8: Meridional structures of shear-free symmetric Rossby waves with $M = 1, 3, 5$ and 7 on the left side and the stable Rossby waves in the westerly wind, the top panels are zonal velocities, u, middle ones are meridional velocities, v, and the bottom ones are potential temperatures, θ.

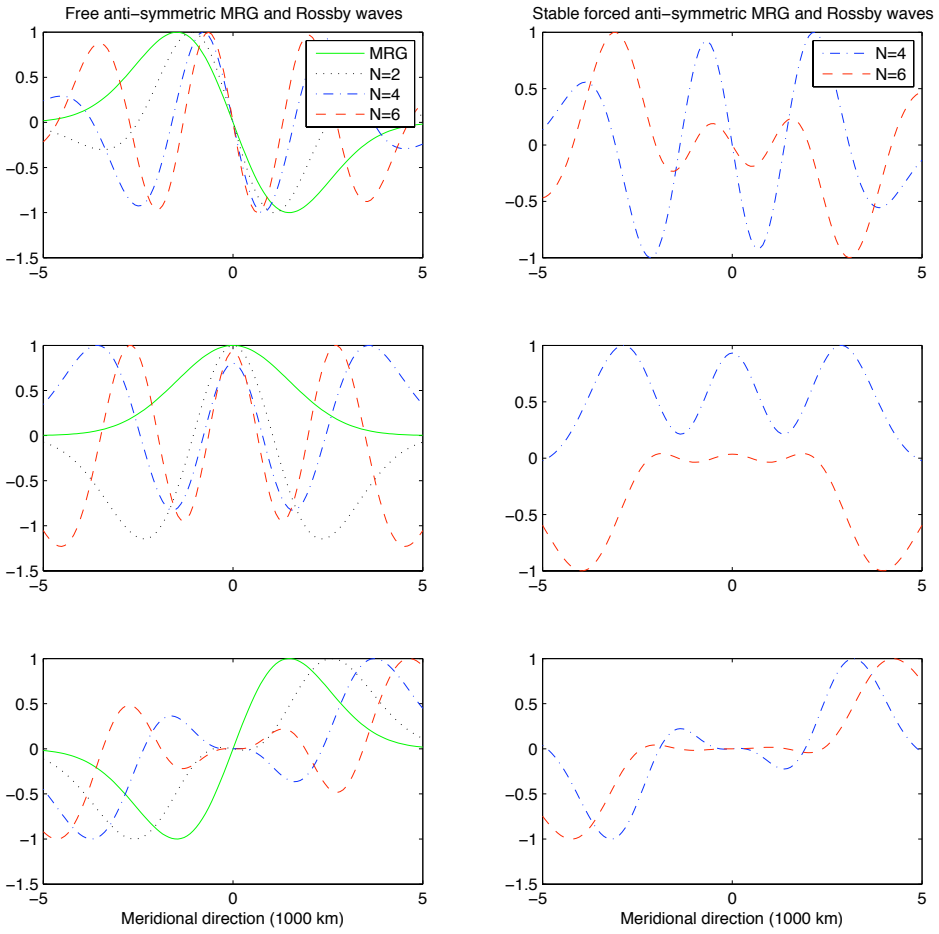

Figure 5.9: Meridional structures of shear-free anti-symmetric westward MRG wave and Rossby waves with $M = 2, 4$ and 6. on the left side and the stable Rossby waves in the westerly wind, the top panels are zonal velocities, u, middle ones are meridional velocities, v, and the bottom ones are potential temperatures, θ.

5.1.3 Physical structure of the equatorial waves in a background flow

Here, we study the changes in physical structure and trapping factor of the shear forced equatorial waves.

- Non-Kelvin aspect of Kelvin waves

  We provided analytic evidence for the generation of meridional velocity for Kelvin wave in the presence of a background shear in chapter 4. We demonstrate that the strength of this meridional velocity depends on the shear gradient and the wavenumber k through $\bar{u}_y \frac{\partial \theta}{\partial x}$. This wavenumber dependency is shown in Figure 5.10 as the relative strength of each components, u, v and θ obtained by $f_{\text{rel}} = \frac{\|f\|_2}{E_c}$ where

$$\|f\|_2^2 = \frac{1}{2} \int_0^X \int_{-\infty}^{\infty} f(x,y)^2 dy\, dx$$

  and

$$E_c^2 = \frac{1}{2} \int_0^X \int_{-\infty}^{\infty} (u^2 + v^2 + \theta^2) dy\, dx.$$

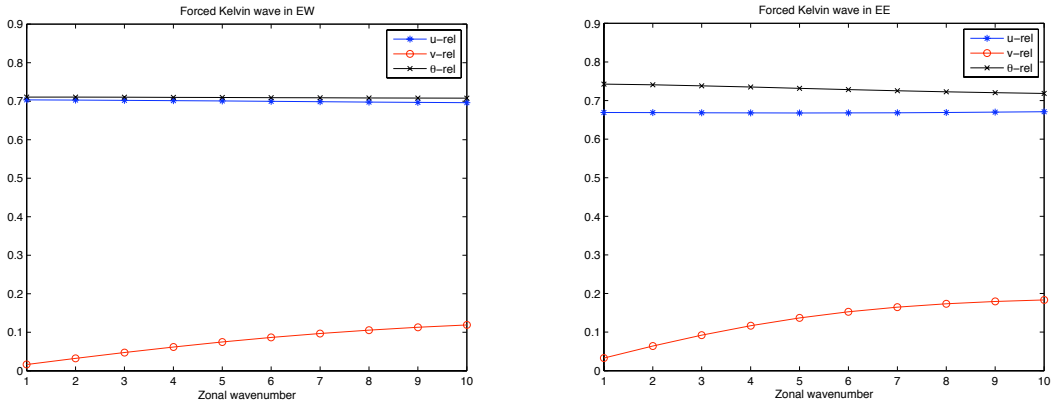

Figure 5.10: Contribution of zonal velocity, u, relative meridional velocity, v, and relative potential temperature, θ, to the total energy for different wavenumbers; in equatorial westerly (EW) and in easterly (EE).

  Note that this effect is more significant for the easterly shear where shear gradient is stronger compared to the westerly shear. Interestingly, this weak meridional velocity induces strong meridional convergence and/or divergence regions,

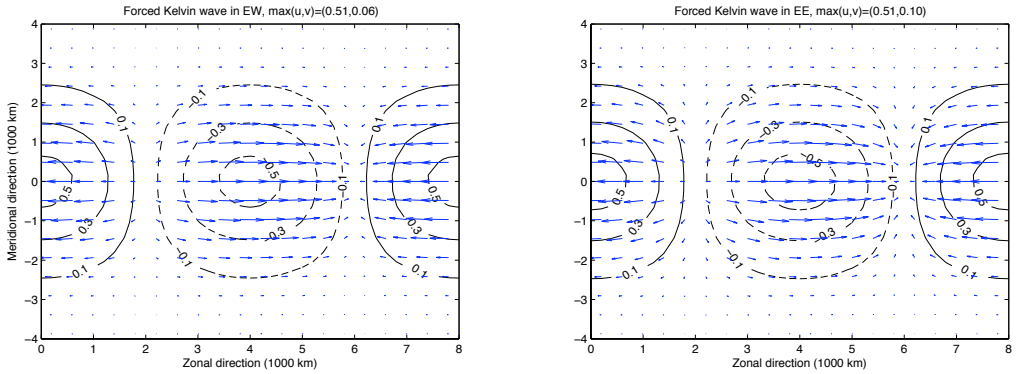

Figure 5.11: Contours of potential temperature and horizontal flow for Kelvin wave with $k = 5$ in EW on the left panel and in EE on the right panel.

compared to the horizontal convergence, shown in figure (5.11) with $k = 5$, which is consistent with the observation in [29, 34]. Furthermore, the normalized meridional structure of the Kelvin wave is shown in Figure 5.12 which shows that the Kelvin wave becomes slightly more trapped off the equator. Also the meridional velocity of the shear forced Kelvin wave is an anti-symmetric function which is like the velocities of the symmetric equatorial waves. This is consistent with the seminal work of Zhang and Webster (1989) but curiously they didnt report about the meridional wind which presumably they assumed zero.

- Gravity waves

  The linear results for trapping of gravity waves are shown in (5.13). The westward gravity waves are highly affected by both shears and their trapping is much weaker compared to the their shear-free counterparts. The effect is more considerable in the easterly background, EE. However, in the presence of EW and EE the eastward gravity waves are generally more trapped except for the zonal velocity in EE which becomes less trapped and deformed compared to their shear-free cases.

- Mixed Rossby gravity wave also known as $M = 0$ gravity

  As we discussed, the westward MRG becomes unstable in EW. However, the EE effect is negligible. The meridional structures of u and θ for the eastward MRG, $M = 0$ gravity, waves are not affected in a shear environment but v is

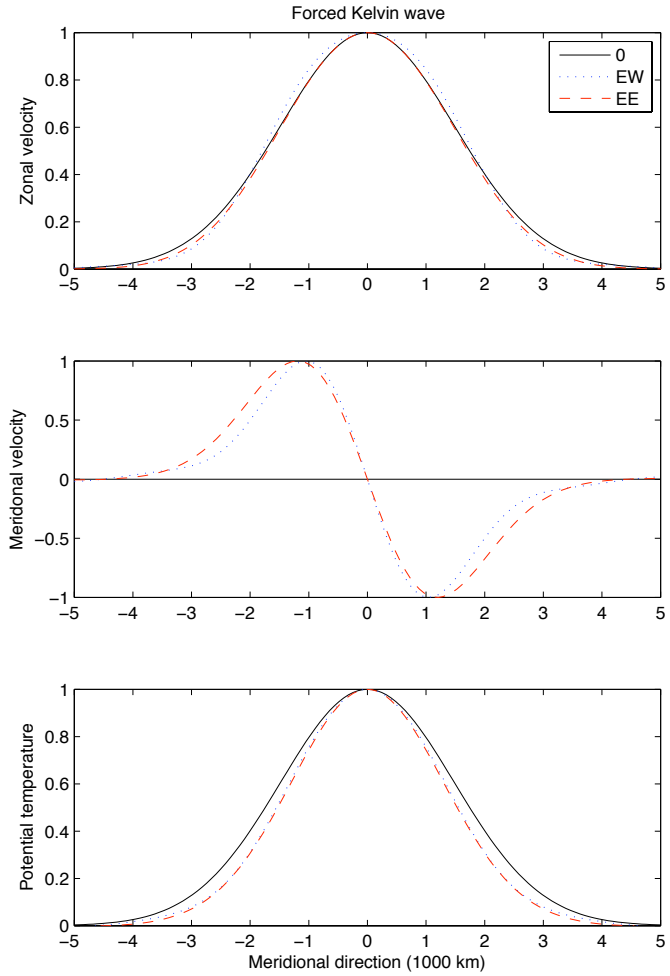

Figure 5.12: Meridional structure of Kelvin wave with $k = 5$ in sheared zonal flow obtained by projected primitive equations; no wind (solid lines), westerly shear (dotted lines) and easterly shear (dashed lines).

more trapped, Figure 5.14.

- Rossby waves

  Rossby waves are believed to modify the tropical-extra tropical energy transport by being less trapped, [43, 33]. However, in this imposed background barotropic shear, the Rossby waves in EE are more trapped but the $M = 1$ and $M = 3$ Rossby waves become unstable in the presence of EW.

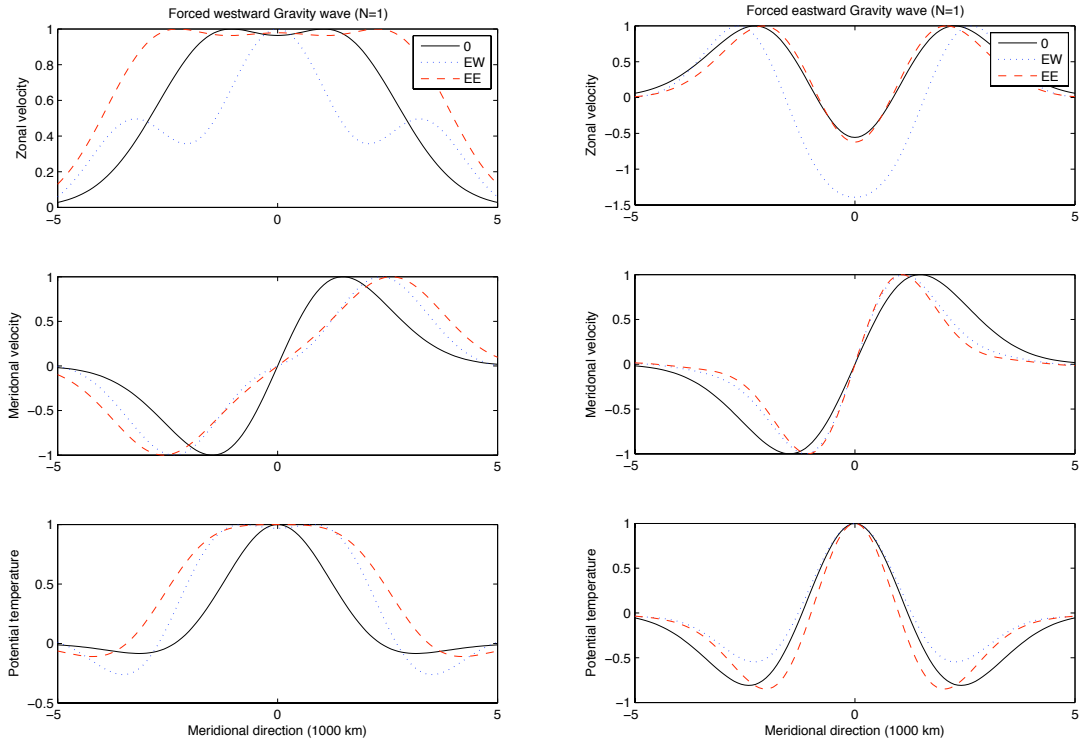

Figure 5.13: Meridional structure of westward gravity wave (left panel) and eastward gravity wave (right panel) for $k = 5$ and $M = 1$ in sheared zonal flow obtained by projected primitive equations; no wind (solid lines), westerly shear (dotted lines) and easterly shear (dashed lines).

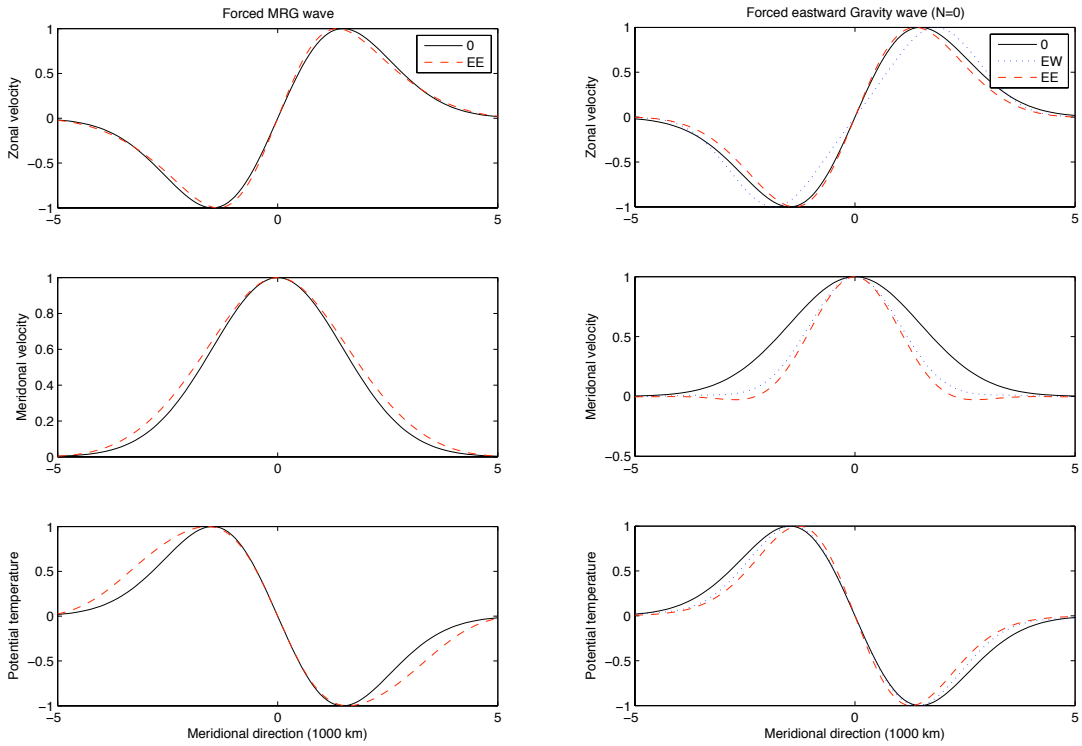

Figure 5.14: Meridional structure of westward MRG wave (left panel) and $M = 0$ eastward gravity wave (right panel) for $k = 5$ in sheared zonal flow obtained by projected primitive equations; no wind (solid lines), westerly shear (dotted lines) and easterly shear (dashed lines).

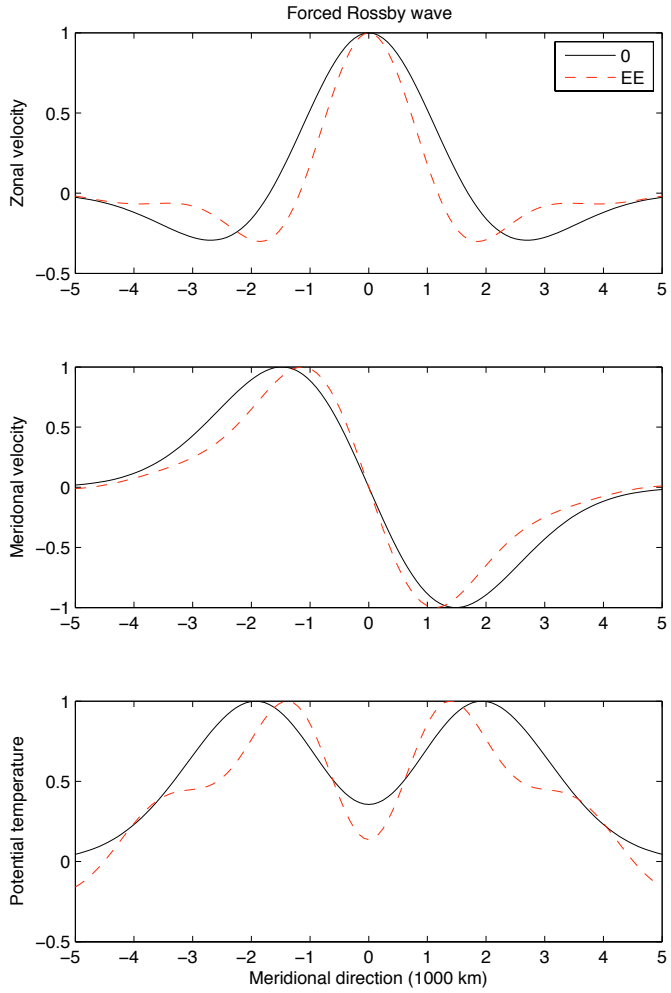

Figure 5.15: Meridional structure of Rossby wave for $k = 5$ in sheared zonal flow obtained by projected primitive equations; no wind (solid lines) and easterly shear (dashed lines).

5.1.4 Comparison with the results in Zhang and Webster

Here, we compare the results we obtained through the linear theory with the one obtained in [43]. Recall that the systems solved here is barotropic-first baroclinic interacting system but the one used in [43] are shallow water equations of Matsuno (2.31). The second difference is the methodology. In [43], the wave solutions are projected onto the first few free equatorially trapped waves of Matsuno. However, in this dissertation, we use the more generalized projection scheme where the variables are projected onto the parabolic cylinder functions. Fist we discuss the difference in frequencies and then the meridional structure of the advected waves.

The first important difference is that in EW background shear, some Rossby waves for both symmetric and anti-symmetric waves and the anti-symmetric westward MRG waves become unstable whereas in [43] all the waves are shown to be stable. The second difference is that most of the stable Rossby waves in both EE and EW propagate in a different direction, including the Doppler shift, compared to their shear-free cases, i.e. the waves move eastward. On the other hand, in [43], all the Rossby waves moves westward however most of the Rossby waves slow down. Finally, for $M = 0$ eastward gravity waves (eastward MRG) the small wavenumbers have smaller eigenfrequencies than their shear-free counterparts while in [43] they all have larger frequencies independent of wavenumbers.

In addition to the frequencies, there are some differences in the meridional structure of the equatorial waves of these two studies. One of the significant difference is that the Kelvin waves in the shear environment have meridional velocities. In [43], it is claimed that the meridional structure of Kelvin waves are unaffected by the shears. Moreover, in the presence of the barotropic shear, the stable Rossby waves become more trapped around the equator though in [43] the Rossby waves become less trapped in the shear environment.

5.2 Dynamical interactions between equatorial waves and the barotropic shear

In order to capture the dynamical effect of the barotropic mode on the equatorial waves associated with the first baroclinic mode, we evolve System (3.26) in time

by using the second order central scheme of Nessyahu and Tadmor (1990) for non-homogeneous conservation laws. Since A is a constant matrix we rewrite System (3.26) as a balanced law

$$\frac{\partial \tilde{W}}{\partial t} + \frac{\partial}{\partial x}(A\tilde{W}) = -(B+C)\tilde{W}. \tag{5.4}$$

5.2.1 Equatorial waves in easterly background

- Kelvin waves

  We use the second order central scheme in (3.18)-(3.19) for system (3.26) with a $k = 4$ Kelvin wave as initial data in the EE shear background and we evolve it in time for 100 days. The interaction between the Kelvin wave and the barotrpic shear deforms the Kelvin wave and moreover consistent with the linear analysis, it induces a weak meridional velocity, Figure 5.16. Nonetheless, a similar result is presented in [3] for a Kelvin wave evolving in a non-homogeneous background where a narrow moist region is separated from the dry environment by stationary precipitation fronts that are parallel to the equator, mimicking the intertropical convergence zone (ITCZ).

  We recall that, this meridional velocity produces significant convergence which reinforces horizontal convergence. In Figure 5.17, the time series of relative meridional wind (left panels) and relative meridional convergence (right panel) are plotted. It shows nine periods of the Kelvin wave over the period of 100 days.

  The time series of the total energy of the Kelvin wave and the relative contribution of each component u, v and θ to the total energy, rescaled by the total energy, are shown in (5.18) and (5.19), respectively. The time series of the total energy indicates that the period of the Kelvin wave increases from almost 9 days and 6 hours to 11 days and 2 hours. This implies that the shear-forced Kevin wave has a smaller frequency compared to the shear-free case which is seen in linear analysis. Moreover, the energy contribution of the meridional velocity is on average 2 percent of the total energy, which is weak compared to the contributions from u and θ.

  We plot the contour of the meridional average of the zonal velocity between $[0, 5000\text{km}]$ in the x-t domain for the period [0-25] days in Figure 5.20. Such

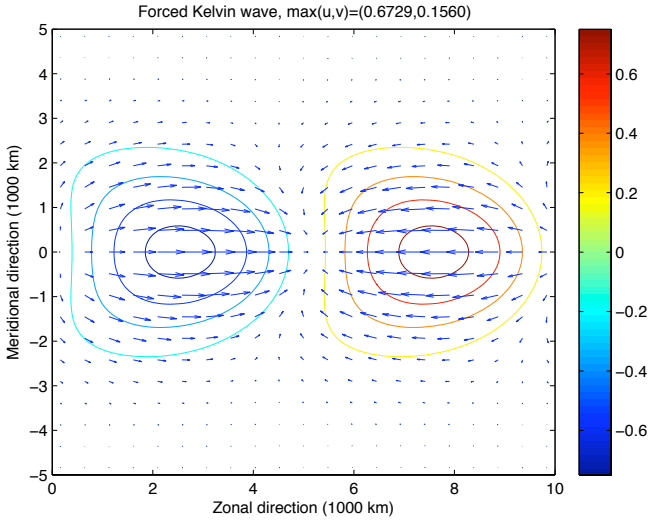

Figure 5.16: Kelvin wave with $k = 4$ in EE after 30 days, contours of the potential temperature and the flow (arrows)

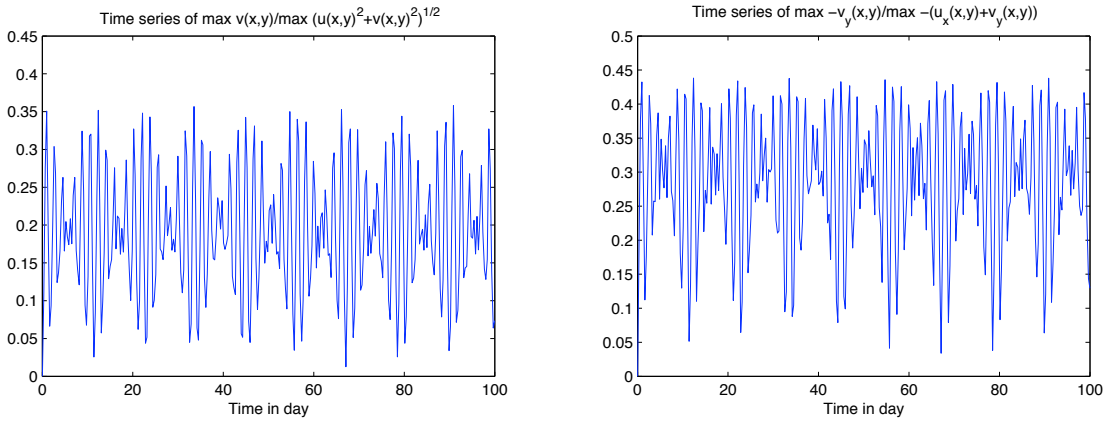

Figure 5.17: Time series of the relative meridional wind (left) and relative meridional convergence (right)of the Kelvin wave $k = 4$.

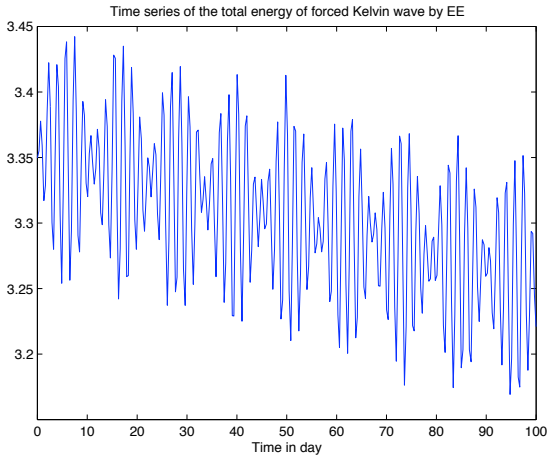

Figure 5.18: Time series of the total energy of the Kelvin wave with $k = 4$ in EE.

contour plots are known as Hovmöller diagrams in the atmospheric science community which are used to reveal wave-like components in the underlying solutions. Throughout this dissertation, for Hovmoller diagrams, we applied the meridionally averaged zonal velocity, i.e.,

$$\bar{u}(x,t) = \frac{1}{Y_0}\int_0^{Y_0} u(x,y,t)dy \tag{5.5}$$

in continuous form or

$$\bar{u}(x,t) = \frac{1}{N}\sum_{j=1}^{N} u(x,y_j,t) \tag{5.6}$$

for the discrete form, where N is the number of grid points in y direction on interval $[0, Y_0]$, where $Y_0 = 5000$ km. Figure 5.20 interestingly reveals that the shear-Kelvin wave interaction excites westward going waves. We plot their power spectrum in the frequency-wavenumber domain for the meridionally averaged solutions in Figure 5.21 which shows three distinct strong peaks: $(k, \omega) = (4, 42), (4, 103)$ and (-4,11). The power spectrum which is the complex modulus of the Fourier transform of the numerical solution from the physical space-time (x, t) domain into the wavenumber-frequency (k, ω) domain is a very popular tool in the study of atmospheric wave dynamics to reveal the persistence of waves in the numerical solutions and or observations [41, 11]. To identify each wave, we filter out different waves one-by-one by using a cut-off

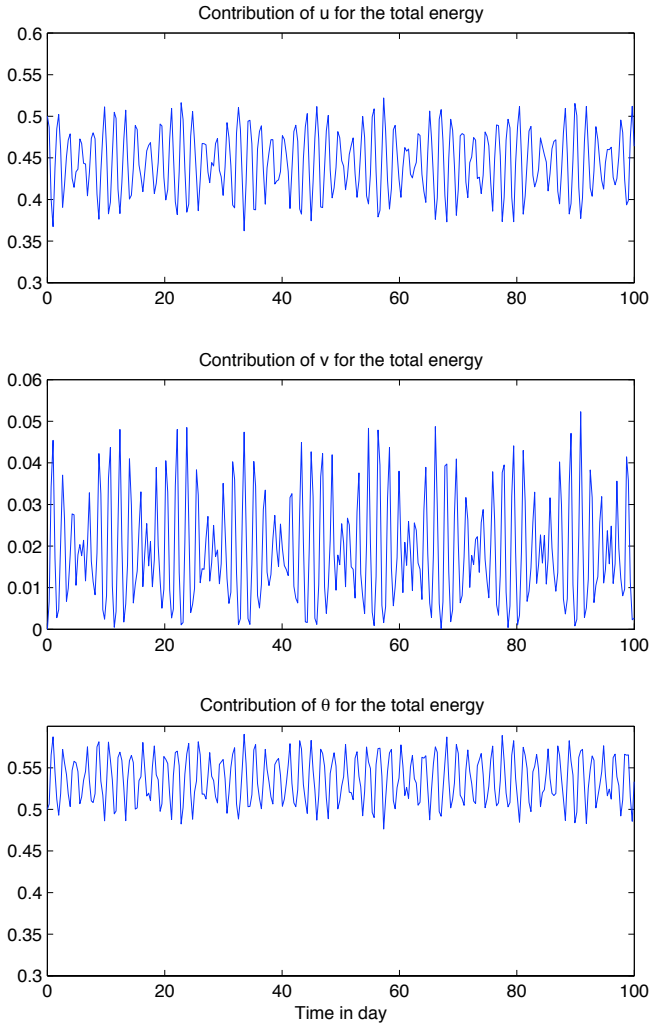

Figure 5.19: Time series of relative contribution of u (top panel), v middle panel and θ bottom panel to the total energy of the Kelvin wave with $k = 4$ in EE.

filter, in the Fourier space, centred around each one of the corresponding spectral peaks, along each meridional level and then Fourier transform back to the physical space. The most significant excited waves are a Rossby wave, eastward and westward gravity waves of weaker strength but their phase speeds and wave structures despite some quantitative differences, resemble those of the dry waves in Figure 5.23. Note that the shear-forced symmetric Kelvin wave with $k = 4$ excites two other symmetric equatorial waves with the same wavenumber. The relative contribution of each one of the waves to the total energy is shown in

Table 5.1, which shows that most of the total energy, 97%, is contributed from the Kelvin wave.

Wave	Kelvin	eastward gravity	Rossby
Relative energy	97.92	0.97	0.62

Table 5.1: Contribution of the Kelvin wave, the eastward gravity wave and the Rossby wave excited by the shear-forced Kelvin wave to the total energy at time $t = 30$ days.

We show snapshots of the contours of the potential temperature and the flow for the filtered Kelvin wave in Figure 5.22, the eastward gravity wave and the excited Rossby wave in Figure 5.23 at $t = 30$ days which is the local maximum of the relative velocity and the relative meridional convergence.

- Rossby wave

  Rossby waves are a subject of great scientific interest as they are believed to play a central role in the tropical-extratropical energy exchange. An example of these studies is the work by Biello and Majda in [2] where they developed a simplified asymptotic equations describing the resonant non-linear interaction of equatorial Rossby waves with barotropic Rossby waves which projects significantly to the midlatitude in the presence of arbitrary vertical and meridional shear mean flow. The results for interaction between the Rossby waves and the prescribed barotropic shear are shown in chapter 6. We demonstrate that the Galerkin projection scheme is not convergent for this interaction and the results are highly dependent on number of modes used for the Galerkin projection. Moreover, in the shear environment, the Rossby wave excites a Kevin wave, with the same non-Kelvin properties as seen above, a westward gravity wave and a $M = 3$ Rossby wave and their structures are presented in Figure 6.14. Here, we present the meridional structure of components of filtered Rossby wave in Figure 5.24 which clearly shows that shear-Rossby wave interaction makes the Rossby wave more trapped around the equator. This trapping is consistent with the solutions obtained by the f-wave algorithm in Figure 6.4.

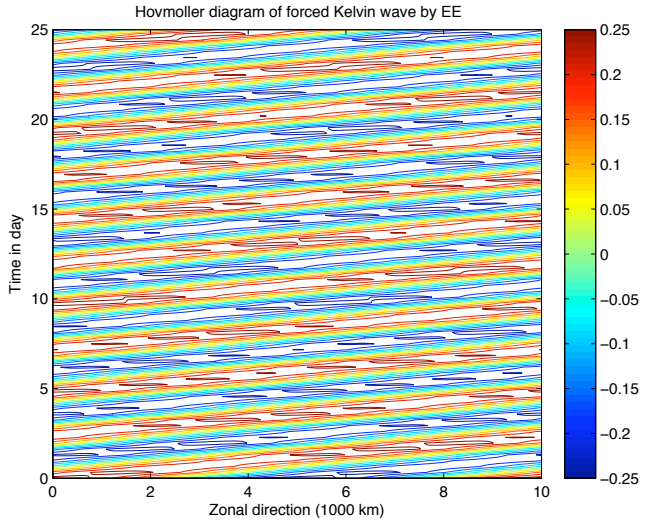

Figure 5.20: Hovmoller diagram of the Kelvin wave with $k = 4$ in EE for [0-25] days.

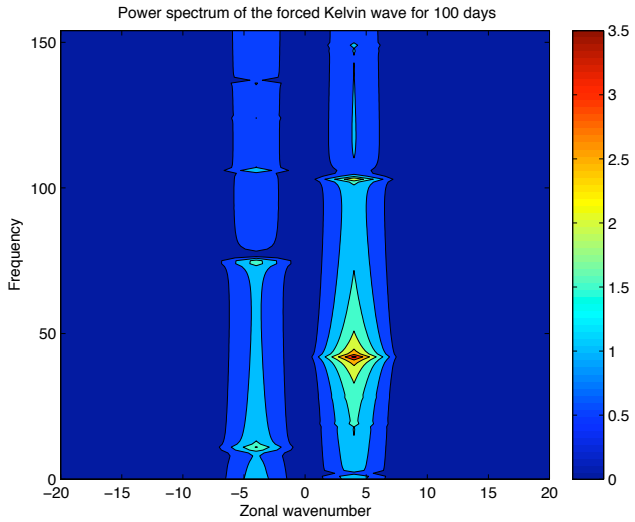

Figure 5.21: Power spectrum in wavenumber-frequency obtained from the Kelvin wave $k = 4$ by EE.

- Eastward MRG

  Here, we study the interaction between the easterly shear and an eastward MRG, $M = 0$ eastward gravity, as an anti-symmetric equatorial wave. We show the time series of the total energy over 50 day period in Figure 5.25 with uniform osculations of about 2 days period, high frequency, and slightly decaying on

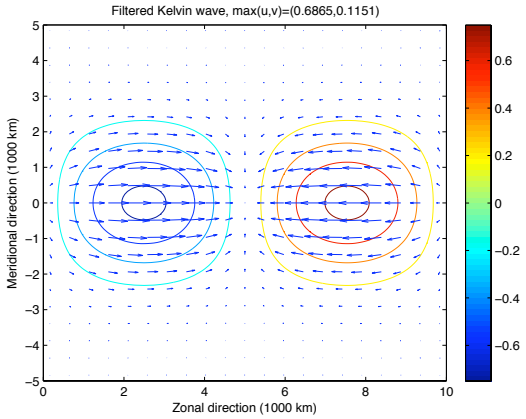

Figure 5.22: Filtered Kelvin wave at t =30 days, contours of the potential temperature and the flow (arrows).

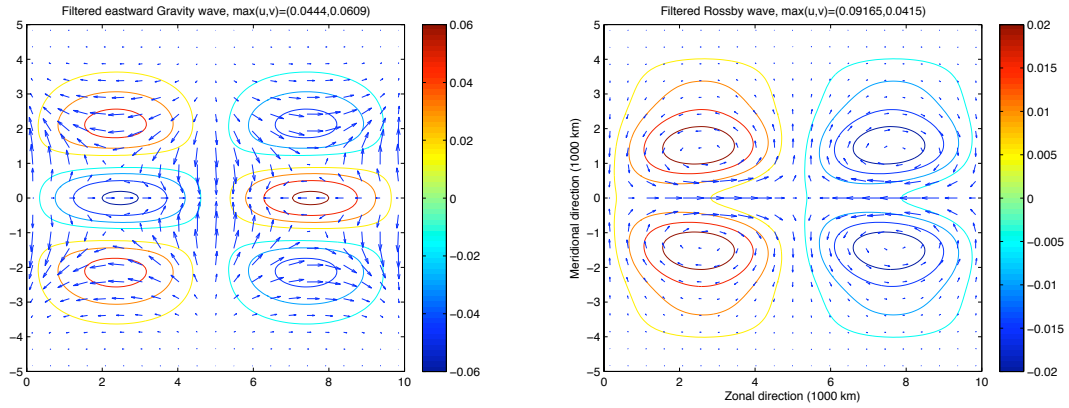

Figure 5.23: Excited eastward gravity (left panel) and excited Rossby wave at t =30 days, contours of the potential temperature and the flow (arrows).

average which might be a consequence of numerical diffusion. Note that these small oscillations of about 6 % of the total energy, might be considered to be spurious due to the artifact of the Galerkin scheme in which the energy is trapped in the spectral space, though this case is also tested with the f-wave algorithm. This yields smaller oscillations of about 1% but the energy time series is decaying more, (result is not shown here). This results from the fact that the f-wave algorithm is dissipative and Dirichlet boundary condition assumption in the meridional direction.

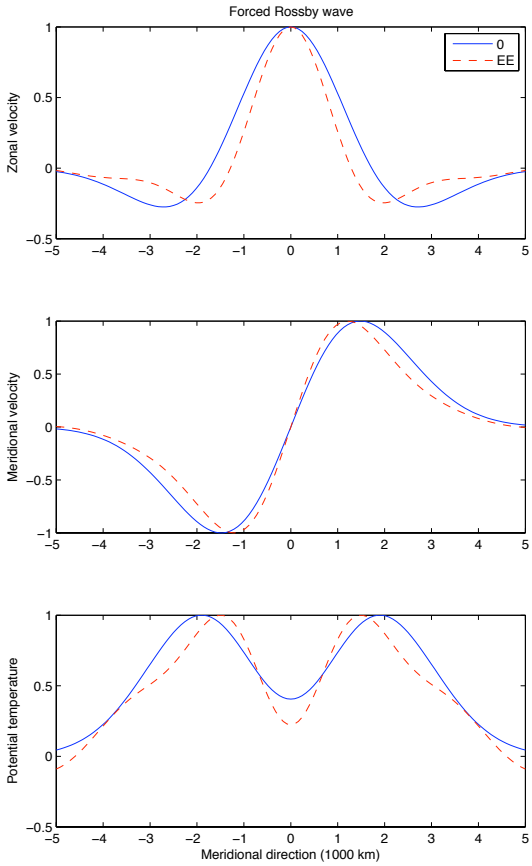

Figure 5.24: Meridional structures of shear-free symmetric Rossby waves with $M = 1$ and Rossby waves by EE, zonal velocity (top panel), meridional velocities (middle panel) and potential temperatures (bottom panel).

In order to characterize the shear-forced wave interaction, we analyse the power spectrum, Figure 5.26, of the solution over 100 days. It suggests that the wave-shear interaction weakly excites other anti-symmetric equatorial waves, an eastward gravity with $M = 2$, a Rossby wave with $M = 2$ and a westward gravity wave but no westward MRG wave. We present the structure of the most significant peaks, namely, the $M = 0$ eastward gravity wave, an excited $M = 2$ eastward gravity, and an excited Rossby wave with $M = 2$ at 30 days, in Figures 5.27 and 5.28. Their relative contributions to the total energy are 97.9%, 2.9% and 0.9%, respectively. These $M = 0$ eastward gravity waves become more trapped around the equator which is consistent with the results of the linear theory.

- Westward MRG wave

  We finish this section by looking at the dynamics of the MRG waves in the shear environment. In linear theory developed in [21] for free equatorial waves, the frequencies of westward MRG waves are asymptotically shown to be equivalent to Rossby waves. On the other hand, we showed that the Rossby waves are highly affected by the easterly shear. So, it is appealing to check the properties of the westward MRG waves and compare the results.

  First, we look at the time series of the total energy, Figure 5.29, which unlike the case of the Rossby wave which depicts large scale oscillations of about $50 - 60\%$ has small oscillations of about 7%. The power spectrum of the shear-forced MRG, Figure 5.30, implies excitation the $M = 2$ Rossby wave and few westward and eastward equatorial gravity waves of weaker strength. Among those, the significant peaks are the $M = 2$ westward gravity and excited $M = 0$ eastward gravity wave. The structures of these waves along with the filtered MRG wave are shown in Figure 5.31 and 5.32.

5.2.2 Equatorial waves in westerly background

We showed by the linear analysis that in the presence of the westerly background, the Rossby waves with $M = 1$ and 3 for symmetric waves and MRG waves and the $M = 2$ Rossby waves for the anti-symmetric waves become unstable. If we evolve any

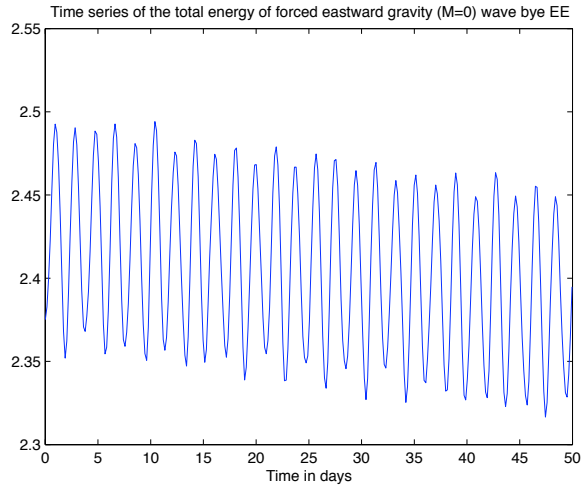

Figure 5.25: Time series of the total energy of the $M = 0$ eastward gravity wave with $k = 4$ in EE.

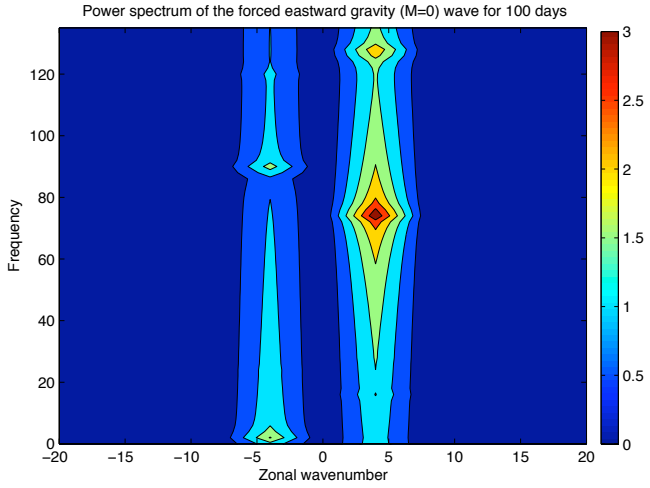

Figure 5.26: Power spectrum in wavenumber-frequency obtained from the $M = 0$ eastward gravity wave $k = 4$ by EE.

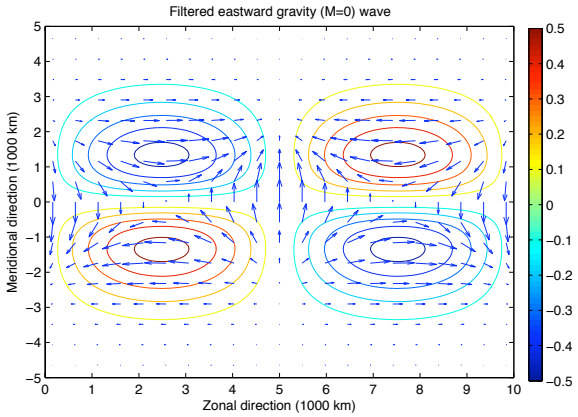

Figure 5.27: Filtered $M = 0$ eastward gravity wave $k = 4$ by EE at t =30 days, contours of the potential temperature and the flow (arrows).

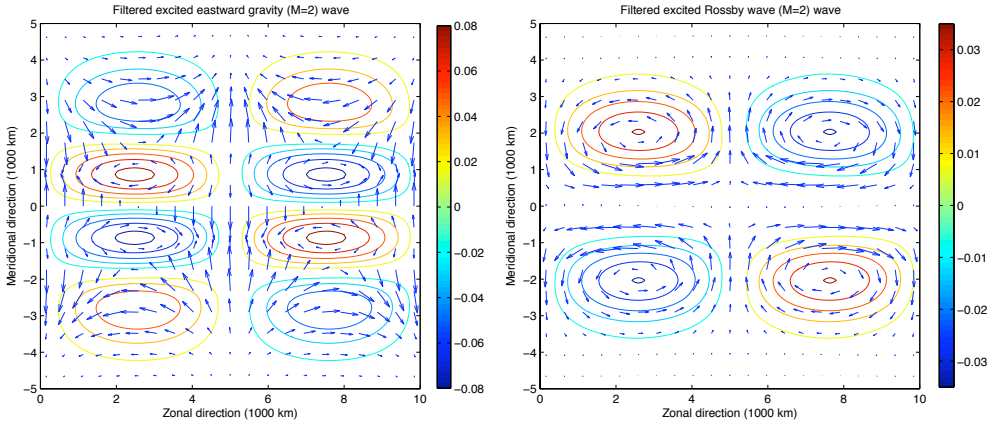

Figure 5.28: Excited eastward $M = 2$ gravity (left panel) and excited $M = 2$ Rossby wave with at t =30 days, contours of the potential temperature and the flow (arrows).

of the symmetric (anti-symmetric) in time, the solution excites the other symmetric (anti-symmetric) waves including at least one of the unstable ones. Therefore over the time, the solution will eventually become unstable because of the excited unstable waves.

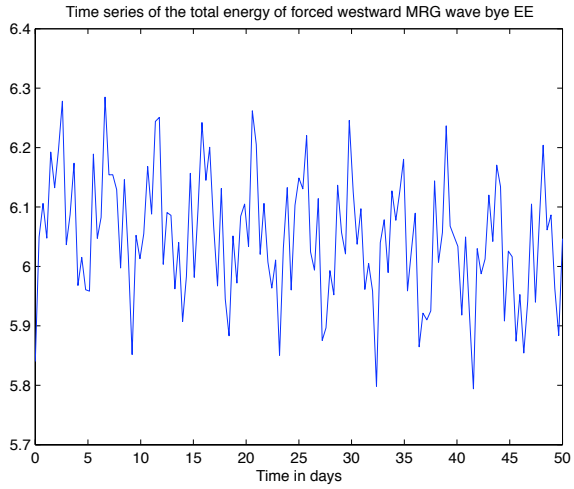

Figure 5.29: Time series of the total energy of the westward MRG wave with $k = 4$ in EE.

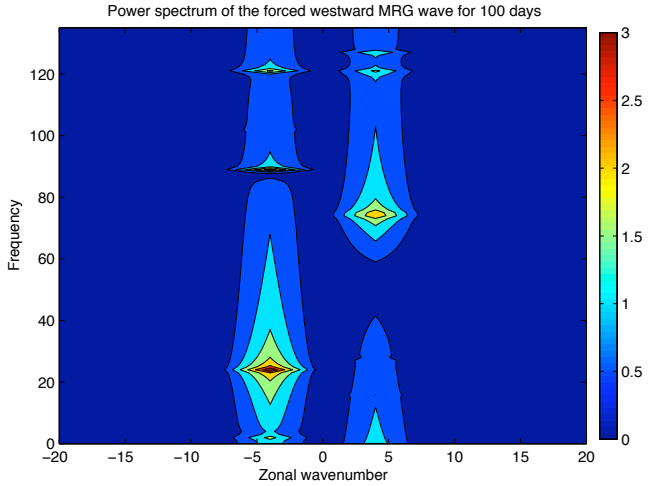

Figure 5.30: Power spectrum in wavenumber-frequency obtained from the westward MRG wave $k = 4$ forced by EE.

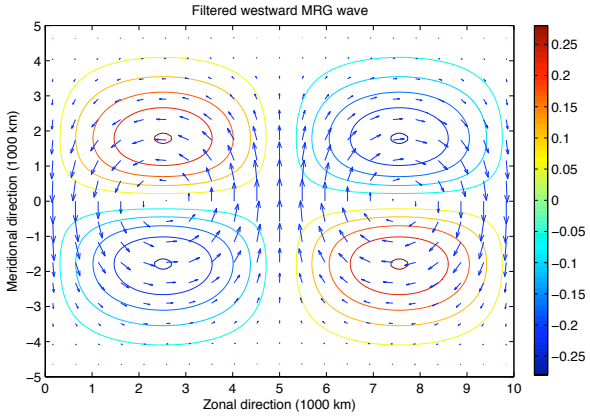

Figure 5.31: Filtered westward MRG wave $k = 4$ forced by EE at t =30 days, contours of the potential temperature and the flow (arrows).

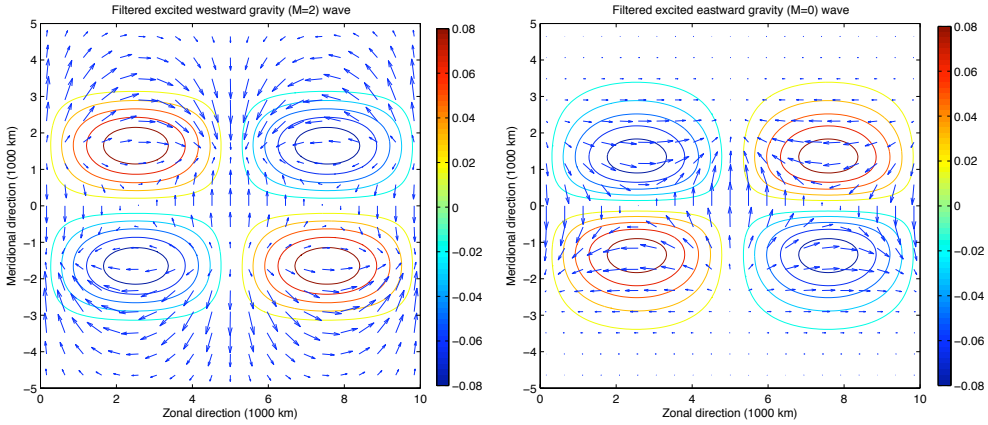

Figure 5.32: Excited $M = 2$ westward gravity (left panel) and excited $M = 0$ eastward gravity wave at t =30 days, contours of the potential temperature and the flow (arrows).

5.3 Kelvin waves in an asymmetric shear

We show that in the shear environment, a symmetric Kelvin wave excites a meridional velocity which consequently induces convergence and divergence regions at the equator. This is due to the fact that the shear is symmetric in meridional direction. However, observations show that these convergence/divergence regions are sometimes off the equator around $5 - 10$ degrees North, [29, 34], depending on the seasons. A plausible explanation for that might be the effect of an asymmetric shear, [25], which may shift the background potential vorticity. To study this circumstance, we consider the asymmetric barotropic shear whose meridional structure is shown in Figure 5.33: the easterly shear considered above but shifted to 750 km north of the equator. A possible justification for a shifted, not symmetric, background shear might be the off-equatorial location of the intertropical convergence zone (ITCZ). The ITCZ is characterized by a region of increased convection, cloudiness, and precipitation which are particularly dependent on the convectively coupled equatorial waves. The location of the ITCZ varies throughout the year but it remains near the equator.

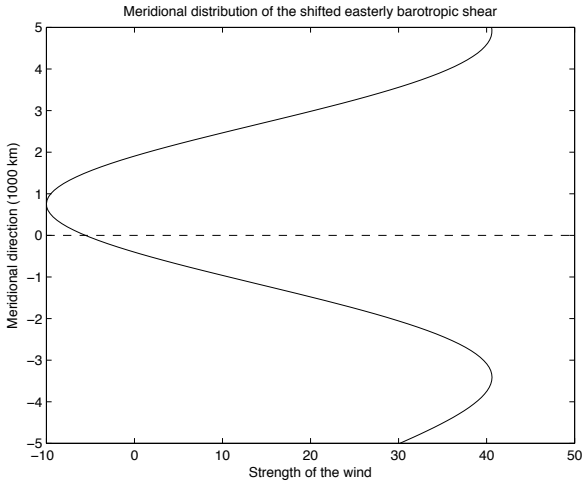

Figure 5.33: Structure of the asymmetric shear; shift the easterly shear to 750 km north of the equator.

We initialize the advected shallow water equations (2.28) with a Kelvin wave with $k = 4$ and integrate over 100 days, using the f-wave algorithm. The f-wave algorithm is chosen because, as demonstrated in the next chapter, it has a better behaviour and the results are more physical. It is important to note that the Galerkin projection is

used to be able to do the linear theory analysis of the advected waves. We present snapshots of the contours of the potential temperature and the flow for filtered Kelvin wave which clearly shows the convergence/divergence regions at around 1500 km north of the equator. Moreover, this interaction excites asymmetric Rossby wave and interestingly an eastward shifted MRG which is an anti-symmetric wave in the shear-free case with much weaker strength. Note that the center of these waves is moved North and the waves have strong gyres in the Northern hemisphere and much weaker gyres in the Southern hemisphere.

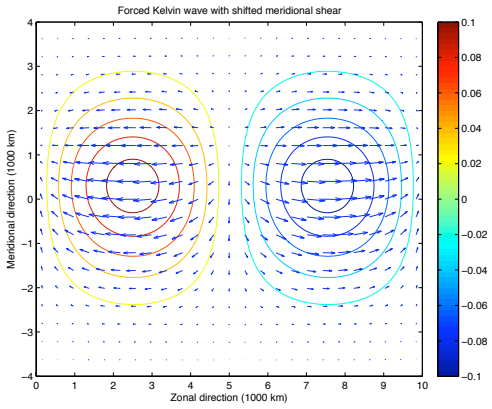

Figure 5.34: Contours of potential temperature and horizontal flow for Kelvin wave with $k = 4$ in the asymmetric shear background.

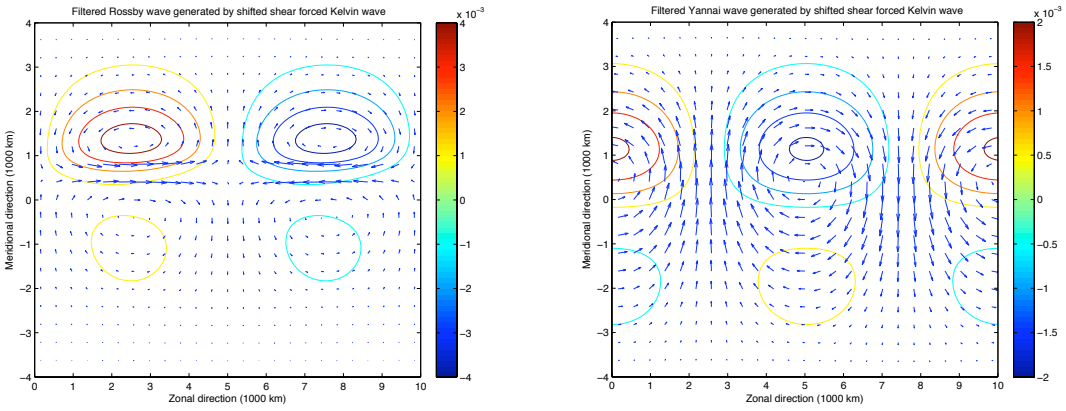

Figure 5.35: Excited asymmetric Rossby wave (left panel) and excited asymmetric MRG wave at t =30 days, contours of the potential temperature and the flow (arrows).

5.4 Summary

We studied the equatorially trapped waves and their properties in the imposed barotropic background shears. Through the linear theory, we demonstrated that the frequencies of most of the shear-forced eastward waves are increased while they are decreased for the shear-forced westward waves. We showed that westward mixed Rossby-gravity (MRG) waves and some Rossby waves become unstable in the presence of the westerly shear. These unstable waves are believed to initiate the convection in the tropics. Furthermore, we examine the trapping of the equatorial waves which can modify the interaction between the equatorial waves and the extra-tropical waves and energy exchange between these regions. We displayed that the eastward equatorial waves become slightly more trapped along the equator for both shears while except for the Rossby waves, the westward equatorial waves are less trapped around the equator. An interesting and specific result of the linear theory is shear-Kelvin wave interaction which induces a non-zero meridional wind. This weak meridional velocity creates meridional convergence/divergence of the flow at the equator.

Moreover, we evolved the system in time to understand the dynamics between the shears and the equatorial waves. We emphasized the excitation of symmetric (anti-symmetric) equatorial waves with the same wavelength, wavenumber, through interactions of another symmetric (anti-symmetric) equatorial waves and symmetric backgrounds. These waves possess the same properties as obtained from linear theory. Finally, we extend the interactions between the equatorial waves with a symmetric shear to present a Kelvin wave and an asymmetric shear interaction which presents the shifted convergence/divergence regions off the equator, consistent with observations. In addition, the asymmetric shear-Kelvin wave interaction excites other symmetric and interestingly anti-symmetric waves with their gyres shifted off the equator. This interaction shows the possibility of excitation of symmetric (anti-symmetric) equatorial waves through the interaction of anti-symmetric (symmetric) waves in an asymmetric shear environment.

Chapter 6

An equatorial wave test case for climate models

Recent trends in the design of climate model dynamic cores involve the use of high order methods to approximate the governing equations [20, 35], borrowed from the applied mathematics literature [19, 27]. In the early days, when the first spectral codes (based on spherical harmonics) were the state-of-the-art, climate models were tested on a statistical basis as to whether under some specific (initial and boundary) conditions they could reproduce well known climate patterns [8] with some statistical significance. These early modellers were not bothering with the point-by-point convergence which is obviously a sensible choice given the impossibility to represent the very wide range of scales involved in the climate system. In fact, a high dimensional dynamical system such as a climate model would always involve a wide range of spatio-temporal scales especially when integrated for long enough time. However, the new generation of climate modellers tend to rely on validation tests that are fully deterministic in order to highlight the high-order convergence and other scalability features of their models, in the spirit of applied mathematics [10, 26, 32], requiring the resolution of all scales of interest. While such tests are very important they do not provide clues about the behaviour of those methods when under-resolved scales are involved.

In this chapter, we propose to illustrate the interaction between the imposed easterly barotropic shear flow and an equatorial Rossby wave as a test case for climate models. Although this is a simple case of dry dynamics, it develops a systematic

turbulent-like cascade of energy toward small scales when integrated for a long time. We present and compare the performance of two of the numerical methods, f-wave and the Galerkin method, to capture this interaction and its dynamics. These methods handle these complex dynamics very differently. The f-wave algorithm has an intrinsic dissipation mechanism that damps energy at small scale but the Galerkin projection does not have a dissipation mechanism. However, the Galerkin projection yields a solution that highly depends on the number of modes used for the projection method. Therefore, the interaction of a prescribed background flow and equatorial waves may constitute a new family of test cases for the validation of climate models which are somewhat in between the rigorous point-by-point convergence testing [10] borrowed from applied mathematics and the statistical validation traditionally used in the climate community [8].

6.1 The f-wave method

In this section, we demonstrate the performance of the f-wave algorithm. We initialize the System (2.28) with a $k = 4$ Rossby wave; the structure of this input solution is shown in Figure 6.1. To test the behaviour of the method under grid refinement, we consider two different grids, 63×63 and 125×125 which correspond to 160 km and 80 km resolution, respectively. We assume homogeneous Dirichlet boundary condition on the North-South boundaries, $u, v, \theta|_{y=\pm Y} = 0$.

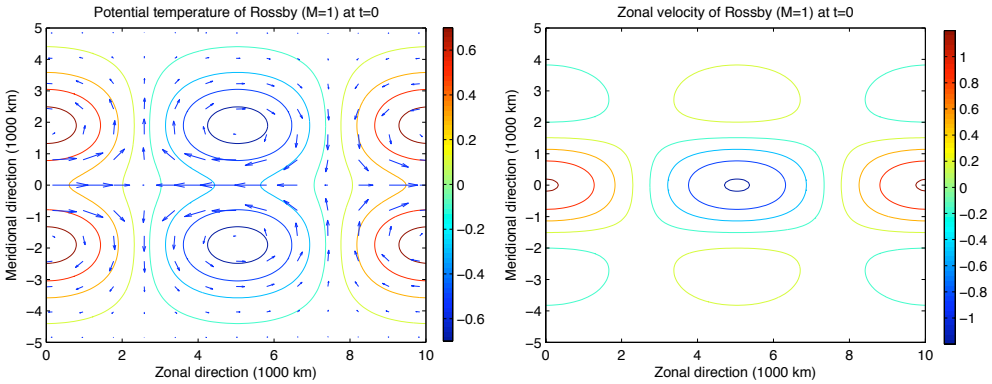

Figure 6.1: The structure of the $M = 1$ Rossby wave used as initial data for the equatorial shallow water system with a background barotropic shear. Contours of potential temperature and velocity profile (left) and contours of zonal velocity (right).

We evolve the system in time for 160 days and show the time series of the total energy, formulated by (2.29), in Figure 6.2 for the two different grids. This figure shows a significant energy loss, around 65% and 53% over a short time period around 35 to 40 days for the 63×63 and 125×125 simulations, respectively. However, this energy loss is beyond the numerical dissipation. After that, the total energy dissipation slows down and saturates to more or less a constant value. This significant energy loss is beyond the numerical dissipation and it is grid independent. The contribution of each flow component to the total energy is shown in Figure 6.3. The energy carried by the meridional velocity and potential temperature decreases abruptly during the first few iterations while the energy associated with the zonal velocity increases, making a rapid redistribution of the energy between these three components, perhaps due the term $-v\frac{\partial \bar{u}}{\partial y}$ on the left hand side of the zonal velocity equation in (3.1). Notice that the time at which the total energy curves in Figure 6.2 ramp down correspond roughly to the time at which the plots in Figure 6.3 start developing rapid oscillations. Note that such oscillations are not present in Figure 6.2 due to some sort of compensation between the three components, u, v and θ. Therefore, these oscillations are not due to numerical instability but rather they may have a genuine physical meaning, as we will see below.

In Figure 6.4, we plot snapshots of the zonal velocity of the solution at three different times: before the energy loss, in the middle of the energy loss, and after the solutions reach the final stage, for the two grids. These times are marked in the plot associated with the total energy in Figure 6.2. Compared to the initial solution in Figure 6.1, these plots demonstrate that in the background barotropic shear, the wave solution quickly deviates from the initial Rossby wave and develops small-scale oscillations implying an energy cascade towards the small scales in the y-direction. Since the f-wave method is dissipative, as are all monotone and/or TVD preserving schemes, it damps the small scale waves whose wavelengths are comparable to the grid scale. After this intense energy cascade, which ends roughly at time $t = 30$ days for 63×63 grid and time $t = 50$ days for the 125×125 grid, we obtain relatively smooth large-scale solutions with much weaker energy compared to the initial set up. Note that the gradual energy decay of the final stage is due to numerical dissipation which is grid dependent and much sharper for the coarse grid. The successive snapshots in Figure 6.4 suggest that the solutions remain trapped in the vicinity of equator and away from the boundary throughout the integration time period. This rules out the possibility

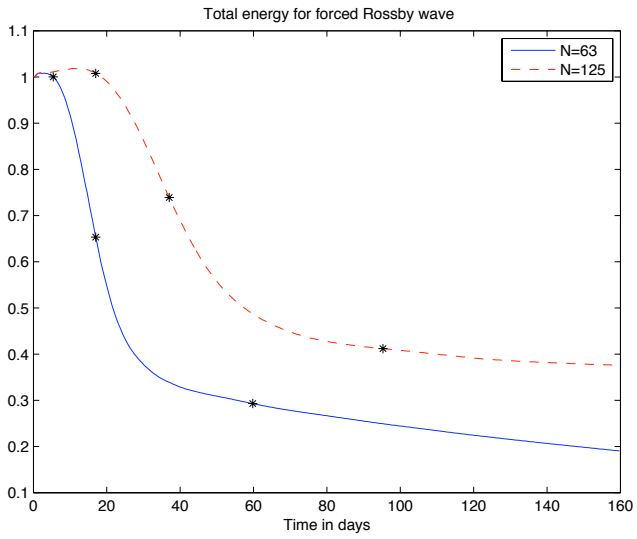

Figure 6.2: Time series of the total energy of the Rossby wave with $k = 4$ in the shear background. The symbols on top of the two energy curves mark the times at the snapshots in Figure 6.4 are taking.

of energy leakage through the meridional walls. Obviously, the main driver for the energy sink/source in the system is the barotropic shear, i.e, energy being transferred to or pumped from the barotropic flow. However, it is not clear at this point how the barotropic-baroclinic energy exchange term contributes to the energy loss shown in Figure 6.2 because our computations show that this term is actually much larger than the actual energy loss and is negative from the beginning of this simulation while the energy tendency is slightly increasing. This clearly suggests that small-scale features are being excited since the beginning of the simulation as can be seen in Figure 6.3.

The difference in timing at which energy is dissipated between the coarse and fine grids could be explained by the fact that the energy cascade reaches relatively quickly the grid scale in the coarse grid, making the time at which the abrupt dissipation occurs a monotonic function of the grid size, the finer the grid is, the longer it takes to dissipate energy. Although from Figure 6.2, it is clear that the energies are very different and considerable amount of energy is dissipated, the structures of the two final stage solutions on the bottom panels of Figure 6.4 look similar in terms of their large scale wave components as demonstrated next.

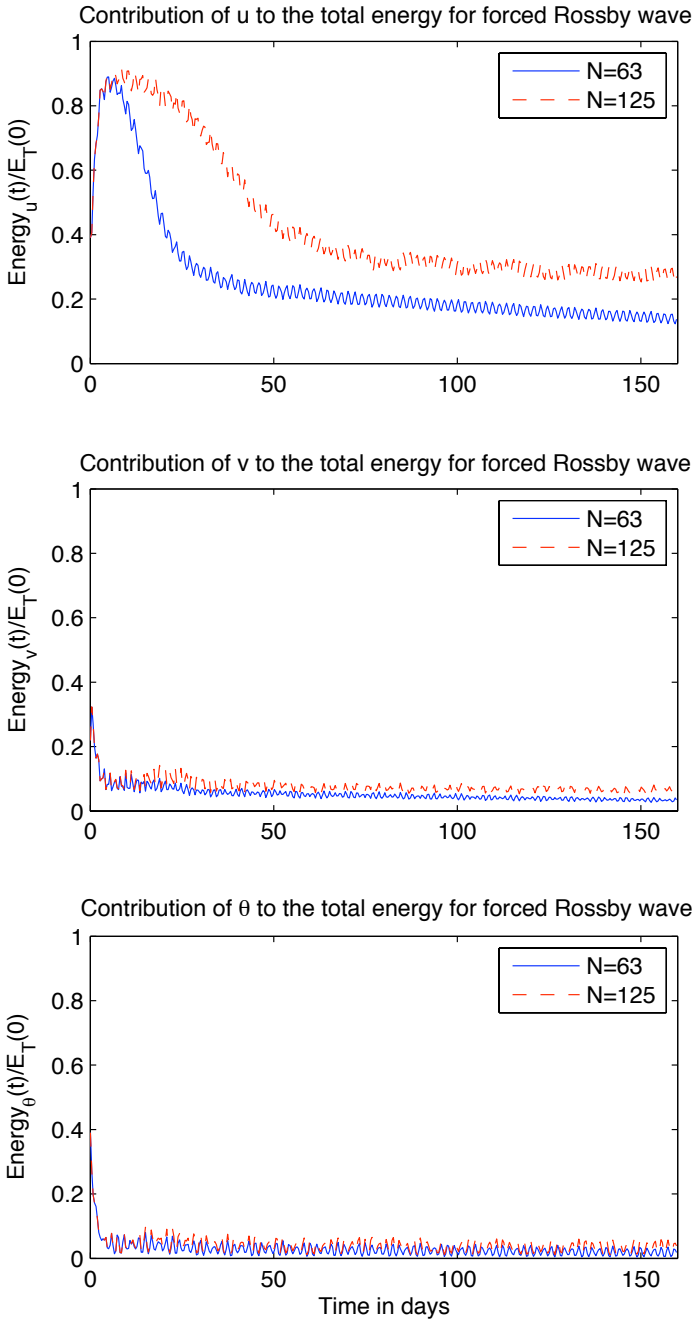

Figure 6.3: Time series of contribution of each component to the total energy of the Rossby wave with $k = 4$ in the shear background.

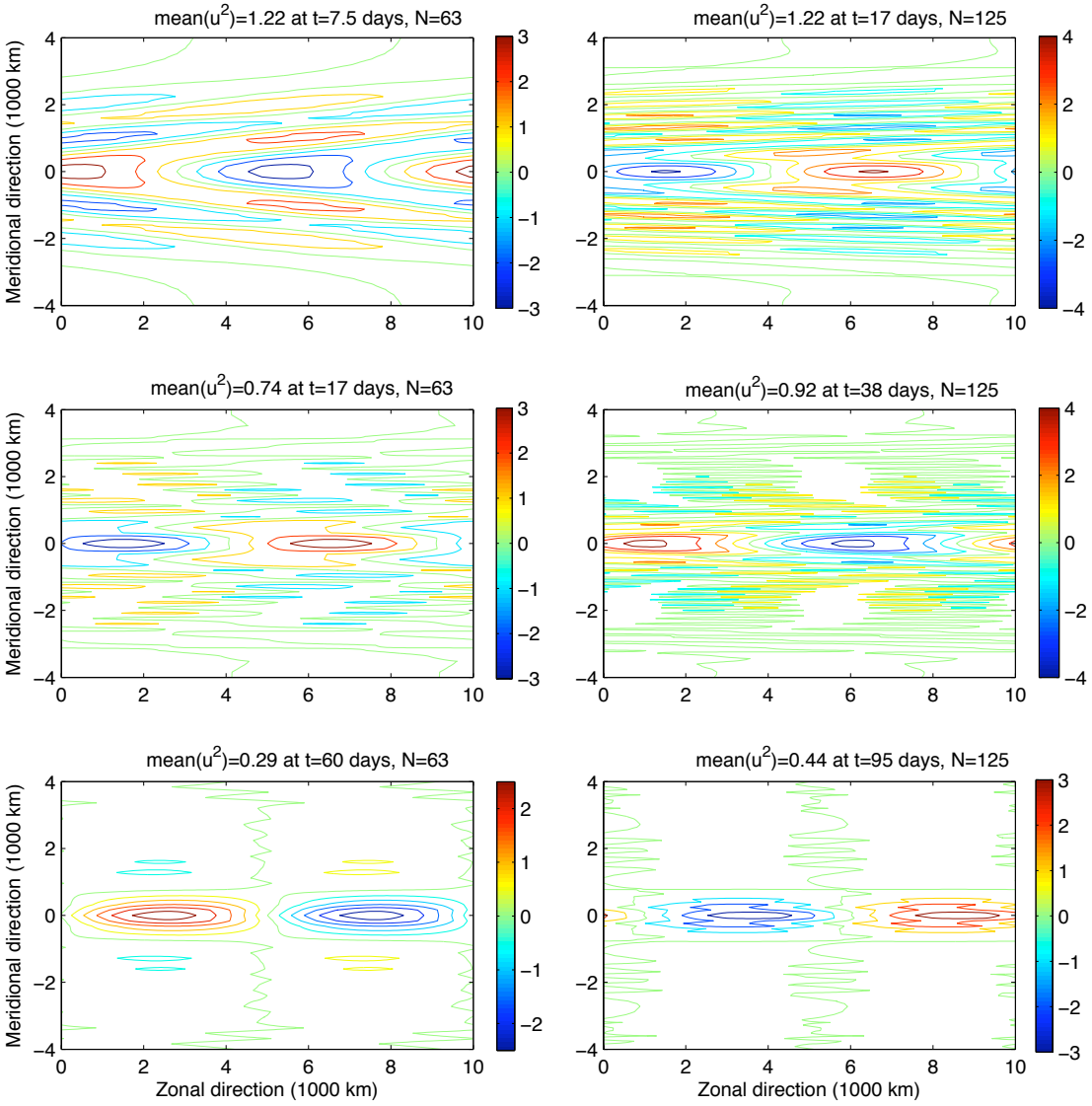

Figure 6.4: Contours of u for Rossby wave with $k = 4$ in the shear background using $N = 63$ (left panels) and $N = 125$ (right panels); at beginning of energy decay (top panels), in the energy decay period (middle panels) and after the energy decay (bottom panels). The exact times at which these plots are taking are marked on the energy plots in Figure 6.2.

To make a physically meaningful comparison of the two numerical solutions in terms of the large scale waves, which are more relevant for practical purposes in terms of the interactions of the wave and the background shear, we plot their Hovmöller diagrams in Figure 6.5. These Hovmöller diagrams are shown for the period of statistically steady state beginning right after the abrupt energy drop phase. This figure suggests that in addition to a westward streak corresponding to the persistence of the initial Rossby wave, two other streaks representing "newly excited" waves emerge as a result of the interaction of the background shear with the Rossby wave. In order to take a close look at the different waves, we plot in Figure 6.6 the power spectrum over the time period 50 to 150 days, corresponding to the Hovmöller plots in Figure 6.5. We distinguish three strong spectral peaks and a weak one which corresponds to an eastward moving wave with high frequency in on both panels.

The structures of the filtered waves associated with the strong peaks are shown in Figure 6.7. By comparing these structures with the free equatorial waves shown in Figure 2.2, we conclude the strong peaks are correspond to the original Rossby, a Kelvin and a $M = 1$ westward inertia-gravity waves. Moreover, the weak peaks of the eastward high frequency waves are associated with $M = 1$ eastward gravity waves, their structures are not shown. Recall that the symmetric Rossby wave is our initial condition while the other three waves are the results of the interaction of this Rossby wave and the backward shear. Note that the symmetric Rossby wave with $k = 4$ in a symmetric shear background excites two other symmetric equatorial waves with the same wavenumber. Since Kelvin waves and westward inertia-gravity waves play an important role in the dynamics of organized tropical convection [41, 11], this finding may provide a plausible mechanism for the genesis of these equatorial waves. The most important feature to notice here is that not only we obtain the same waves in both simulations but the two sets of plots in Figure 6.7, represented by each column, are very similar both qualitatively and quantitatively, their wave strengths, in the statistical sense. This provides somewhat a physically meaningful measure under which the f-wave method seems to converge. As we will see below, the Galerkin method does not have this property.

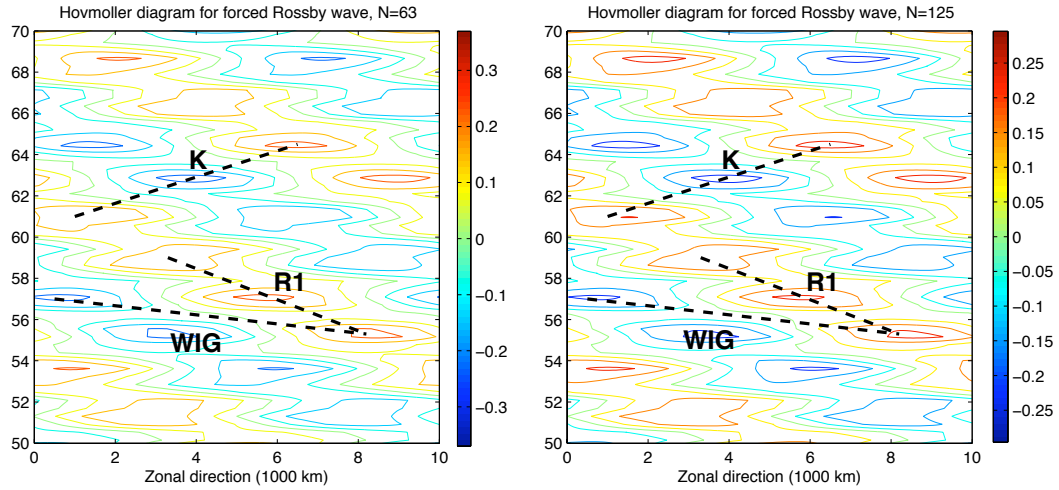

Figure 6.5: Hovmöller diagram of the Rossby wave in easterly shear background over the steady period [50-150] days for different grids; N=63 (left panel) and N=125 (right panel).

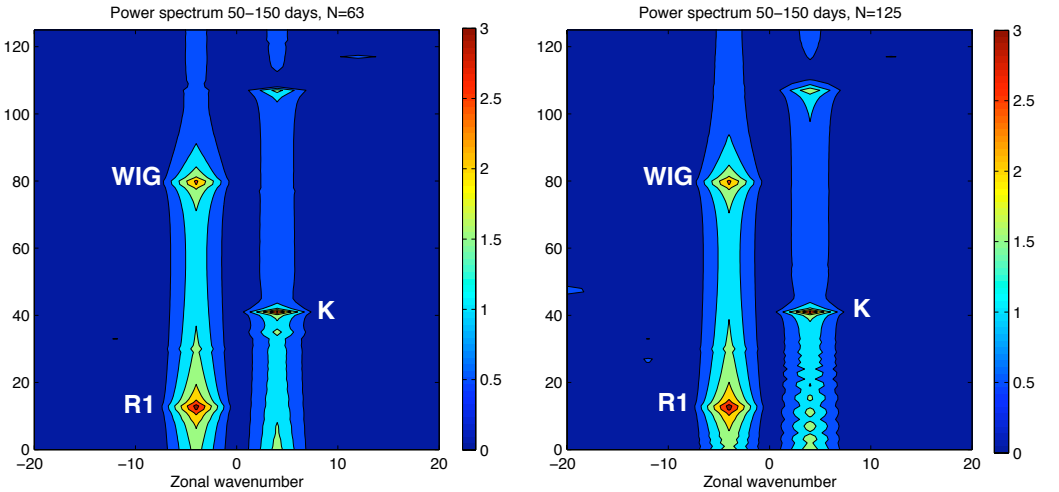

Figure 6.6: Power spectrum of the Rossby wave in easterly shear background over the steady period [50-150] days for different grids; N=63 (left panel) and N=125 (right panel).

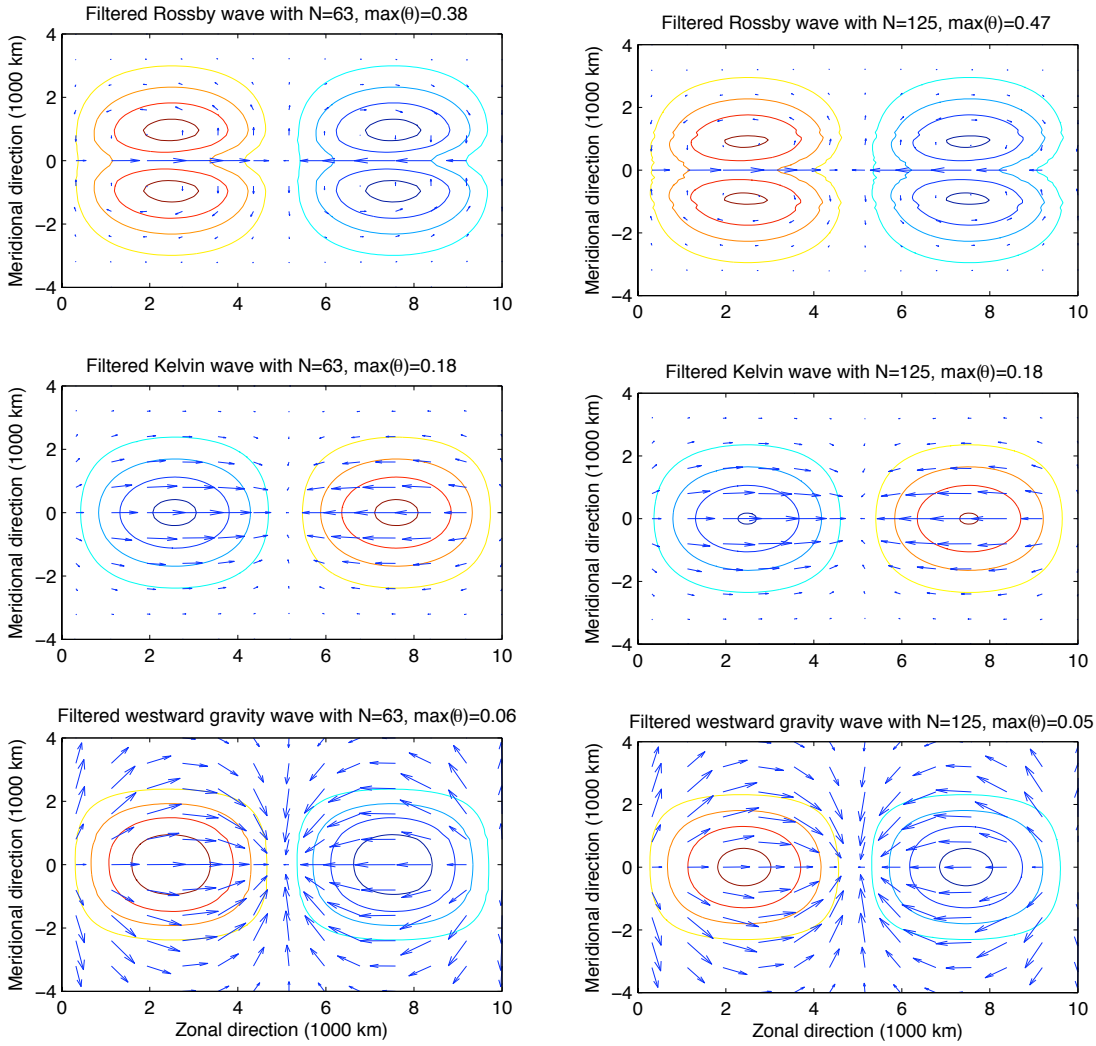

Figure 6.7: Contours of θ and arrows of the flow for Rossby wave with $k = 4$ in the shear background using $N = 63$ (left panel) at time $t = 100$ days and $N = 125$ (right panel) at time $t = 120$ days.

6.2 The Galerkin projection

In this section, we present the results of the Galerkin projection method in the meridional direction combined with the NT central scheme to evolve the projected System (2.28) in time. The same Rossby wave is used here as the initial condition as in the case of the f-wave method. Similarly, we perform two simulations corresponding to two different numbers of meridional levels (or equivalently basis functions) for the Galerkin projection, one with $N = 9$ and one with $N = 15$. We also use a fairly high number of grid points for the central scheme in the zonal direction to dissociate the dependence of the results from the NT scheme.

The results are shown below in Figures 6.8 to 6.14. First, we look at the time series for the total energy. Within the first few days, 4 days or so, the two energy curves corresponding to the two numbers of meridional modes coincide perfectly but after that, the time series diverge from each other. Unlike the energy plots in Figure 6.2, corresponding to the f-wave simulation, where the overall behaviour is fairly the same with the two curves settling down to a more or less constant energy state, the two Galerkin simulations show strong variability in energy with quasi-periodic oscillations, with a period highly dependent on the number of Galerkin modes. This is a clear indication that the two simulations have reached very different wave dynamics after the first few days and thus the Galerkin projection method may not converge, as the number of basis functions increases, even in the wave-statistical sense described above.

The Galerkin method does not have an intrinsic energy dissipation mechanism at small scales and indeed it conserves energy in the absence of external forcing [23]. As the energy cascades towards small scales, it is automatically reflected back toward large scale and keeps bouncing back and forth which is consistent with the quasi-periodic oscillations in Figure 6.8. Notice that the finer simulation (N=15) has a longer period than the coarser one (N=9) because the energy has a much longer 'distance' (in terms of number of modes or waves) to travel in the (meridional) wavenumber domain.

Despite the large oscillations of about 50-60% in the total energy, after the transient-adjustment period, the energy seems to be conserved on averaged which is reminiscent of the fact that the projection method does not dissipate energy by itself. To gain more insight into the energy transfer across meridional scales, we compare the merid-

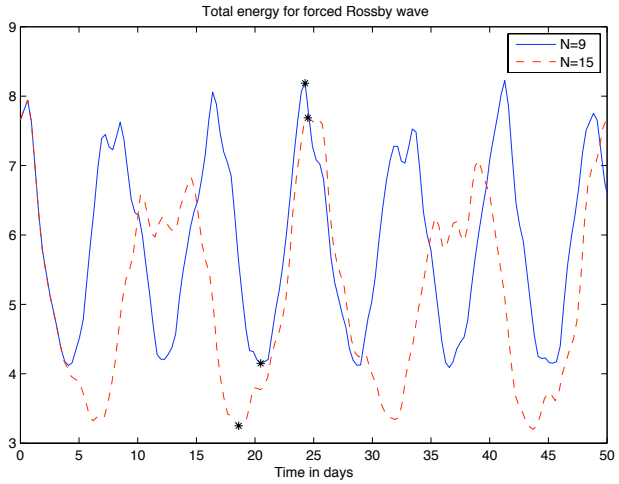

Figure 6.8: Time series of the total energy of the Rossby wave with $k = 4$ in the shear background using different number of modes in meridional direction.

ional modes of a free Rossby wave, Figure 6.9, with the meridional modes of the Rossby wave in the shear environment at a peak and a trough of the energy time series, shown in Figure 6.8 for the two simulations, in Figure 6.10. This comparison suggests that the Rossby-shear interaction project onto small-scale waves with higher meridional modes. Moreover, Figure 6.10 displays that for both simulations, small scale waves are excited at the local minima while large scale waves seem to carry most of the energy at the local maxima. To interpret the sudden cascade of energy at the beginning of the interaction, we show the meridional modes of the product terms of the background shear and the 'Rossby wave' in (2.28), $\bar{u}(y)u_x$, $\bar{u}(y)v_x$, $\bar{u}(y)\theta_x$ and $v\bar{u}_y(y)$ in Figure 6.11. These products are heavily projected onto higher meridional modes, small scale waves, from the beginning of the interaction which accounts for the excitation of small scale waves.

Therefore we conclude from Figures 6.8, 6.11 and 6.10 that right at the beginning of the simulations, the Rossby wave loses some of its energy quickly through a forward energy cascade to small scale, large meridional index, waves just like in the case of the f-wave simulations presented in the previous section. However, since the Galerkin method does not have a mechanism to automatically damp energy at the grid scale, the cascaded energy accumulates for a while at small scales and then ultimately bounces back towards the large scales through a backward cascade resulting

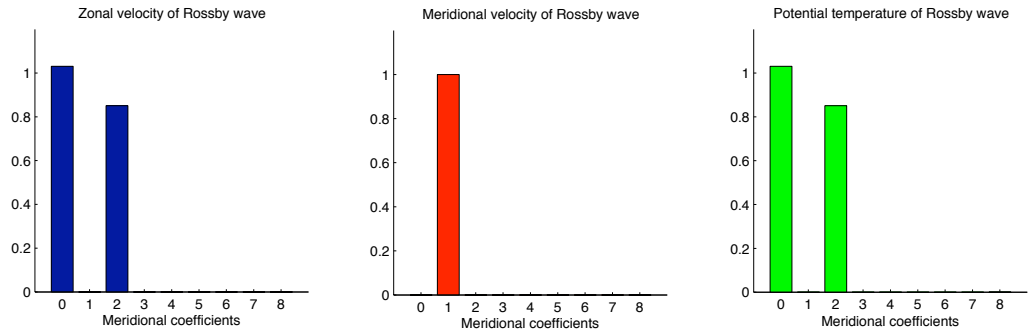

Figure 6.9: Meridional coefficients of the free Rossby wave for $N = 9$

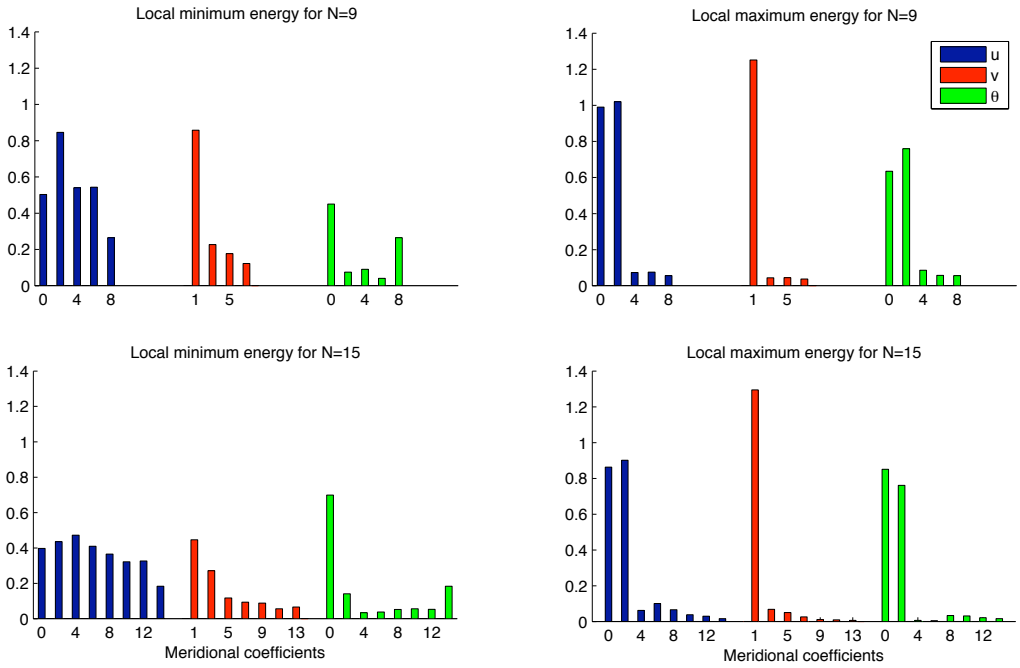

Figure 6.10: Meridional coefficients at the local minimums (left panels) and local maximum (right panels) for $N = 9$ top panels and $N = 15$ bottom panels.

in the energy oscillations seen in Figure 6.8 between higher modes (small scale waves) and lower modes (large scale waves), as anticipated above.

The length of the interval through which energy bounces back and fourth depends on the number of modes used in the Galerkin truncation. Thus, the period of the total energy oscillations and the solution itself depend heavily on the number of modes.

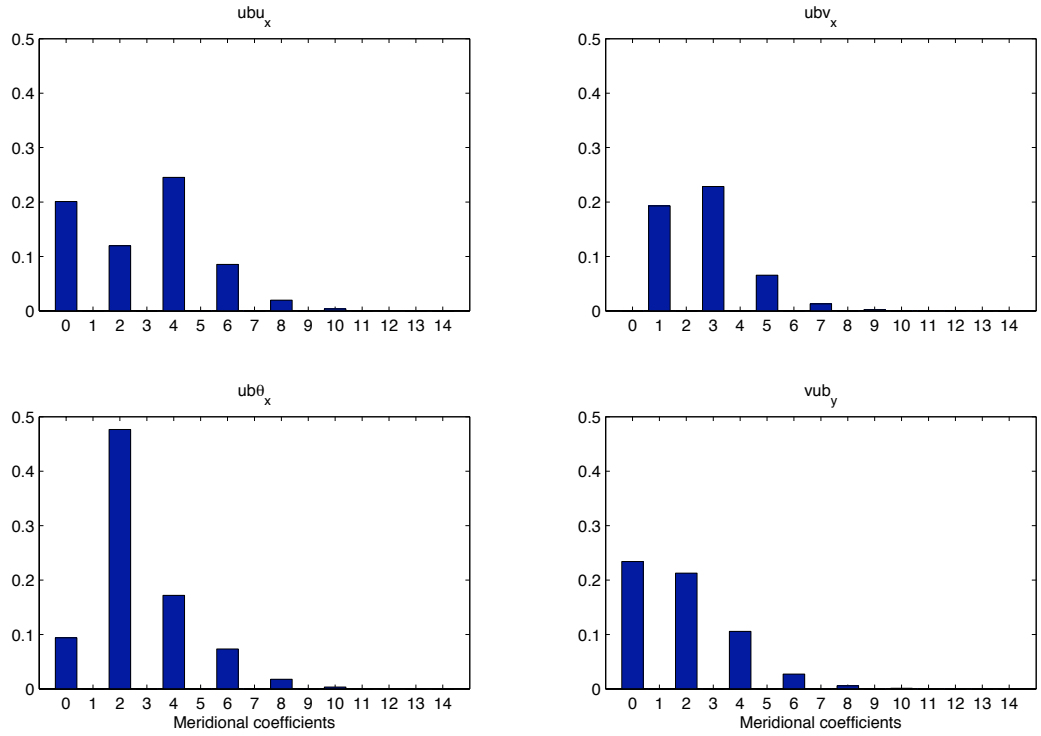

Figure 6.11: Meridional coefficients of the projection of terms $\bar{u}(y)u_x$ (top left panel), $\bar{u}(y)v_x$ (top right panel), $\bar{u}(y)\theta_x$ (bottom left panel) and $v\bar{u}_y(y)$ (right bottom panel) for $N = 15$.

These results show that the scheme is not convergent in the statistical sense. To confirm that we plot the Hovmöller diagrams for the two Galerkin projection simulations in Figure 6.12. We first compare the Hovmöller diagrams for 100 day period which are shown in the bottom panels. Clearly, there is a slow wave travelling eastward for $N = 9$ and westward for $N = 15$ which verify the claim that the scheme does not converge. However, if we zoom in over 20 day period, top panels, the original Rossby wave, a faster eastward-moving and finally a faster westward-moving waves can be seen on both panels and their corresponding streaks are highlighted by the dashed lines.

In Figure 6.13, we plot the associated power spectrum which reveals common peaks. These peaks correspond to the original large-scale Rossby, an excited Kelvin wave and an inertia-gravity wave with $M = 1$ by comparing the structure of these filter

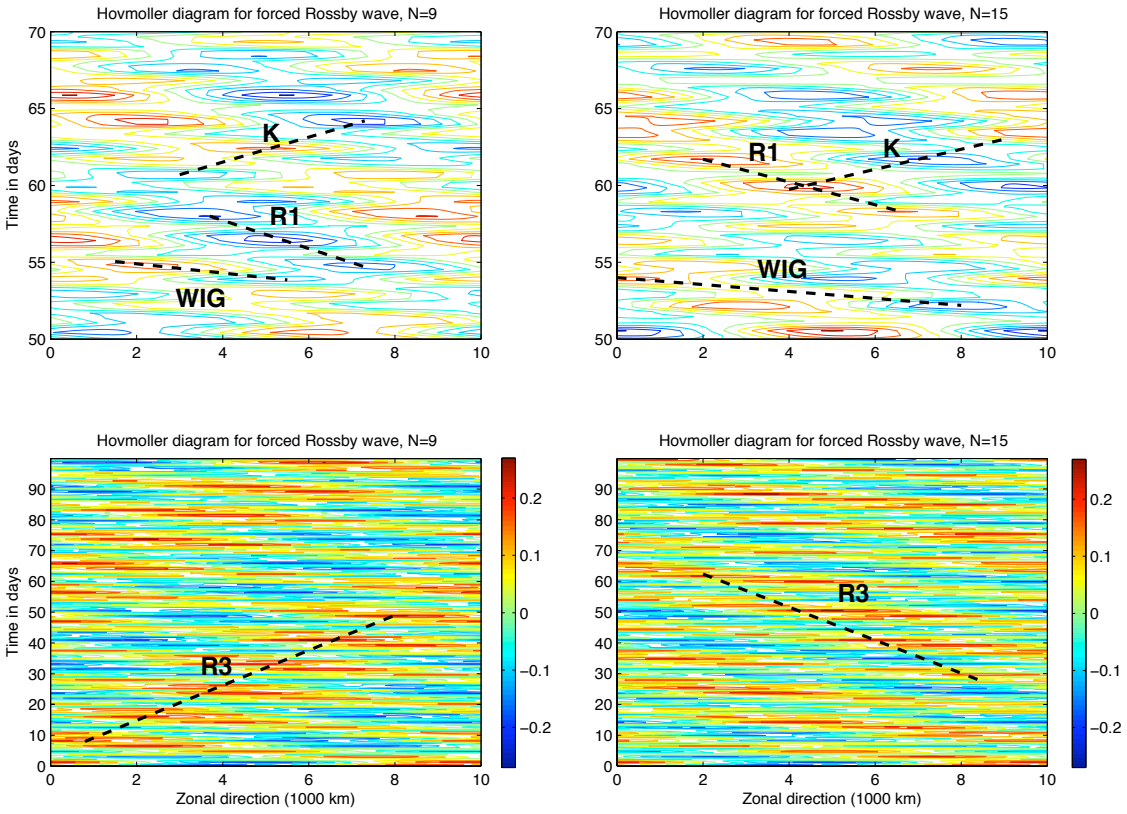

Figure 6.12: Hovmöller diagram of the Rossby wave in the easterly shear background over period of 20 days (top panels) and 100 days (bottom panels) for $N = 9$ (left panels) and $N = 15$ (right panels); Note that $M = 3$ Rossby wave moves eastward for $N = 9$ and moves westward for $N = 15$.

waves, Figure 6.14, with the shear-free equatorial waves, Figure 2.2. There are other fairly strong peaks corresponding to different higher index $M \geq 3$ symmetric Rossby modes that are on either one of the panels. However, $M = 3$ Rossby wave peaks appear on the bottom right of the $N = 9$ panel but on the bottom left of the $N = 15$ which correspond to the slow eastward moving wave for $N = 9$ and slow westward moving wave for $N = 15$ seen in the Hovmöller diagram for 100 day period. The other Rossby waves with ($M \geq 5$), although weaker, that appear on the bottom right portion of the panel, i.e, moving eastward. Note that these results are consistent with the results obtained by linear theory in Chapter 5. This suggests that the energy that accumulates at "small scales" actually ride on different sets of high index

Rossby waves, depending on the resolution (number of modes used) of the Galerkin truncation method.

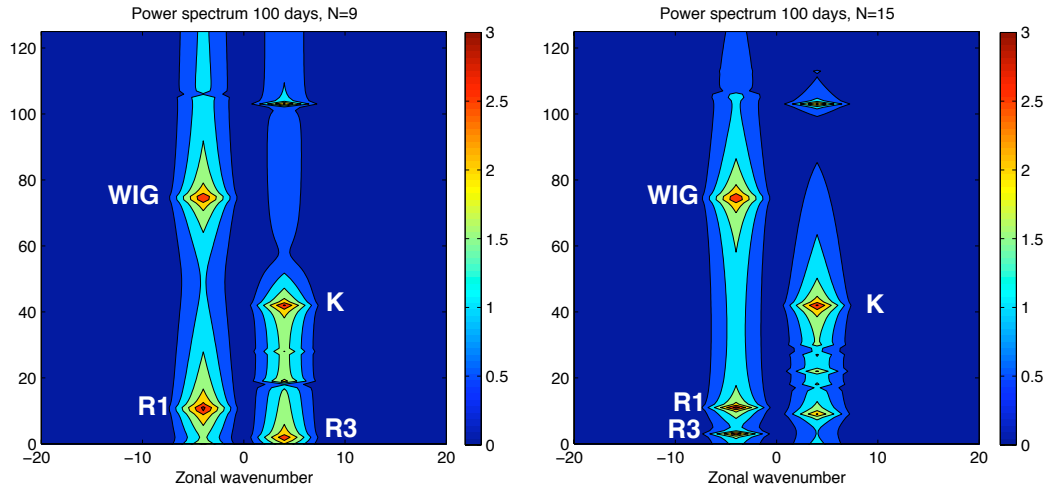

Figure 6.13: Power spectrum of the Rossby wave in the easterly shear background over period of 100 days for $N = 9$ (left panel) and $N = 15$ (right panel).

In Figure 6.14, we present the structure of $M = 1$ Rossby wave and the three most significant equatorial waves (Kelvin, westward gravity, and $M = 3$ Rossby) excited through the interactions of this Rossby wave and the background shear at $t = 30$ days, between a maximum and a minimum energy level for both $N = 9$ and $N = 5$ simulations. Note that the Rossby waves and the excited Kelvin wave become more trapped around the equator but the westward inertia-gravity wave becomes less trapped in the shear background. Moreover, the excited Kelvin wave has the weak meridional velocity which exhibits convergence/divergence region at the equator. It is important to recall that the three main large-scale waves that remained after the abrupt energy loss in the f-wave simulation are also present here for both the $N = 9$ and $N = 15$ simulations. Nevertheless, the two Galerkin simulations have some extra-waves of high meridional index and also $M = 3$ Rossby wave moves eastward for the $N = 9$ simulation and westward for the $N = 15$ simulation.

In table 6.1, we show the strength of the main peaks of Figure 6.13 for both $N = 9$ and $N = 15$. It shows that the two common excited waves, Kelvin and westward gravity, carry a small portion of energy in both cases but $M = 3$ Rossby waves which

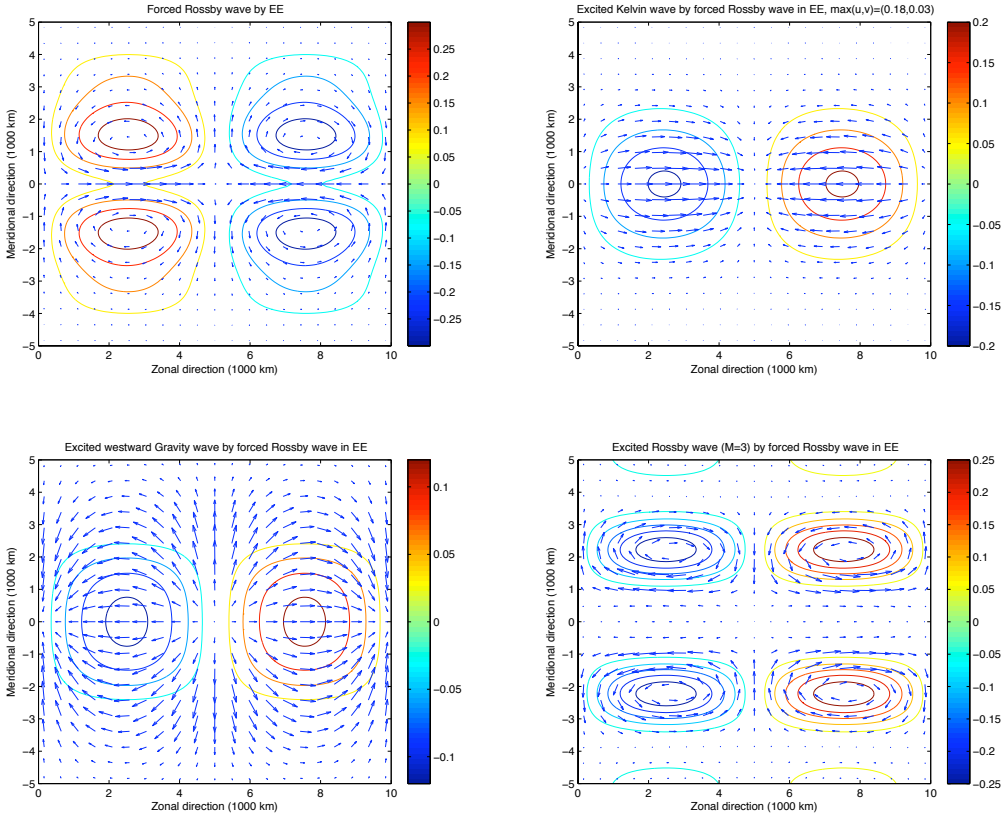

Figure 6.14: $M = 1$ Rossby wave in the shear environment (top-left), excited Kelvin wave (top-right), excited westward gravity wave (bottom-left) and excited $M = 3$ Rossby wave at t =30 days; contours of the potential temperature and the flow (arrows).

Wave	$M = 1$ Rossby wave	$M = 3$ Rossby	Kelvin	westward gravity
N=9	70.87	16.35	3.92	3.24
N=15	69.02	17.06	4.31	3.73

Table 6.1: Contribution of $M = 1$ Rossby wave, and excited westward gravity wave, Kelvin wave and $M = 3$ Rossby wave excited by $M = 1$ Rossby wave in the background shear to the total energy at time $t = 30$ days.

are highly dependent on the number of projection modes account for a significant amount of energy.

6.3 Summary

In this chapter, the interaction of an equatorially trapped Rossby wave and the easterly background shear is considered. We studied and compared the performance of a Galerkin projection method and the f-wave algorithm to capture the dynamics. A rapid cascade of energy of the Rossby wave toward excitation of small scales waves is an interesting feature of this interaction despite the simplicity of the model. Such complex interactions of equatorial waves may provide an interesting test bed for climate model dynamical cores, especially those based on high order approximation which may require artificial viscosity in order to prevent artificial backward cascades of energy.

These two numerical methods handle this cascade very differently. The f-wave algorithm dissipates energy as it approaches the grid scale and results in an enormous energy loss before the solution settles down into a more or less grid-independent smooth solution. However, the f-wave algorithm converges under grid refinement, i.e., the total energy time series cascades and then saturates to different but a steady state depending on resolution. In addition, the interaction between $M = 1$ Rossby and background shear excites the same equatorial waves, Kelvin wave and westward gravity waves with the same frequencies and same wave structures.

However, the Galerkin projection method exhibits strong oscillations in its energy time series as a manifestation of transport of energy back and forth between the small scales and large scales. Without an intrinsic dissipation mechanism at the grid

scale for the Galerkin method, the cascaded energy accumulates at the small scales and then bounces back into the large scales. Both the period of energy oscillations and the nature of the solution in terms of its wave components are highly dependent on the number of projection modes used for the Galerkin method. Moreover, in addition to a Kelvin wave and westward gravity wave, a $M = 3$ Rossby wave with significant contribution to the total energy is excited which moves in different directions, eastward for $N = 9$ and westward for $N = 15$. This suggests that the Galerkin method does not converge for this interaction and should not be used for across scale dynamics. The Galerkin method would converge eventually if we add an artificial viscosity to the original system to damp the small-scale waves but this is not the goal of this study.

Chapter 7

Summary and conclusion

7.1 Summary

In this PhD dissertation, we discussed the interactions between the equatorially trapped waves associated with the first baroclinic mode and barotropic, vertically averaged, background flows in the context of a simplified model. We considered two background shears: one characterized by equatorial easterlies and one by equatorial westerlies, mimicking the jet stream at 200 mb in winter over the western and the eastern Pacific oceans, respectively [43]. We solved this system by using state of the art numerics to capture any deviations of the flow fields from the initially set equatorially trapped wave. We considered three numerical schemes for this system of balanced law: two finite volume methods, F-wave algorithm and the central scheme of Nessyahu and Tadmor, and a Galerkin-truncation based method.

To address the physical impact of the interactions between the equatorial waves and the background flow, we used the Galerkin projection which facilitates the study of these interactions through both linear theory and time integrations. Through linear analysis, we looked at the properties of the equatorial waves such as their frequencies, directions of propagation, trappings and finally their stabilities in the imposed shear backgrounds. For both prescribed shears in general, the frequencies of most of the eastward waves increase while for westward waves, they decrease. We showed that in the presence of the westerly shear, westward mixed Rossby-gravity (MRG) waves and some Rossby waves become unstable and possess complex frequencies, which suggests that they might contribute to the genesis of organized convection. In the sheared en-

vironment, the eastward equatorial waves become slightly more trapped while the westward equatorial waves besides the Rossby waves, especially the westward gravity waves, are less trapped along the equator for both shears.

In order to capture the dynamical evolution of the waves in the presence of these shears, we integrated the system over time. First, we studied a Kelvin wave, then a Rossby wave, an eastward gravity wave with ($M = 0$) and finally a westward MRG in the easterly background shear. One of the significant outcomes of this work is the properties of the equatorial Kelvin waves, which play an important role in the organized convection in tropics, in the shear environment. Unlike their uncoupled free analogues, Kelvin waves in nature are observed to have a weak but non-zero meridional velocity [41]. We showed that the interaction of a Kelvin wave with this barotropic shear induces a non-zero meridional wind. Nevertheless, it provides a significant equator-ward contribution to the mass convergence in the regions of upward motion that enhances moist convection, in the context of convectively coupled waves. While the strength of the meridional wind increases with increasing zonal wavenumber (of the Kelvin wave) and/or strength of the background shear, the induced meridional convergence stays relatively the same regardless of the wavenumber, shown in [5]. However, the frequency of the oscillations in the maximum meridional wind and meridional convergence seems to amplify significantly with the wavenumber. Moreover, this shear-Kelvin interaction weakly excites other symmetric equatorial waves such as a $M = 1$ Rossby wave and an eastward gravity wave which more or less have the same properties as obtained in the linear theory.

Furthermore, we studied an equatorial Rossby wave response to this shear environment. Like the Kelvin waves, the shear-Rossby wave interaction excites other symmetric equatorial waves of the same wavenumber, a Kelvin wave, a westward gravity wave and a $M = 3$ Rossby wave. We also investigated the interaction between an eastward gravity wave ($M = 0$) and a westward MRG as examples of anti-symmetric waves. These interactions generate other anti-symmetric equatorial waves such as Rossby waves, westward and eastward gravity waves with the properties consistent with the linear theory. Finally, the westerly shear is hypothesized to be the initiation of the organized convection because in the presence of the westerly shear both symmetric and anti-symmetric waves become unstable. This is due to the excitation of at least one unstable wave through these interactions which makes the original wave

and the excited ones unstable and abruptly growing after few iterations.

Finally, we studied the interaction between a Kelvin wave and an asymmetric shear to demonstrate a possible explanation for observed off-equatorial convergence/divergence of the flow and consequently mass. This interaction excites other symmetric as well as anti-symmetric equatorial waves but the center of the waves are shifted. Among those, a Rossby wave with $M = 1$ and a westward MRG wave are significant and their asymmetric structures are presented where their stronger gyres are located in the Northern Hemisphere and the weaker ones are in the Southern Hemisphere.

Beside that, we proposed a test case for climate models dynamical cores which involve the use of high order methods to approximate the governing equations. This test case is the interaction between equatorially trapped Rossby waves and a prescribed easterly barotropic shear which rapidly cascades the Rossby waves' energy toward small-scale equatorial waves despite the simplicity and linear character of the system.

7.2 Conclusion

It is essential to understand the interactions between equatorially trapped waves and extratropical waves in order to improve climate and weather prediction models. One approach to study these complex dynamics is developing simplified or idealized models which capture the main features of the dynamics. One of the factor which highly can affect the equatorial waves is the background state. Here, we studied a model for the barotropic shear-first baroclinic equatorial waves interactions. For the prescribed barotropic shears considered here, we only assumed meridionally varying zonal wind. However, this simplified model illustrates the complexity of the dynamics and the effect of the extra-tropics on the tropical dynamics by different processes.

The extra-tropical wind affects the zonal transport of energy in the tropics by influencing the phase speeds and the propagation directions of the equatorial waves. We showed that the frequencies of all these waves and the propagation directions of Rossby waves change in the presence of a shear, especially for higher wavenumbers. We also showed that the advected equatorial waves by the westerly shear become unstable and grow in time. This can enforce and stimulate the tropical convection in the convergence regions of the waves. We showed that stable Rossby wave-shear

interaction excites other waves and in particular a Kelvin wave which is recognized as the one equatorial wave that carries a significant amount of precipitation from organized convection at the synoptic scale. The advected Kelvin waves by the shear and also the excited Kelvin waves both have the non-zero meridional velocity. This meridional velocity leads to convergence and/or divergence regions which are shown to play an important role for convection [41]. Finally, the barotropic shear may induce energy exchange between the tropics and the extra-tropics by modifying the trapping of these equatorial waves in the shear backgrounds. We showed that the westward gravity waves become highly less trapped in the presence of the shear and somewhat also true for the westward MRG waves.

Another important result of practical interest in this work is the performance of numerical schemes to capture the dynamics of the equatorial waves. For example, we showed that the central scheme should be avoided for the advection of tracers that possess a complex structure in the direction perpendicular to the advection direction for long runs, as done in climate simulations. A practical example of these phenomena is moisture or liquid water fields associated with a convectively coupled equatorial wave, which propagate along and are trapped in the vicinity of the equator.We conclude that climate models should be carefully validated against equatorial waves dynamics using simple test cases such as the Rossby-shear interaction example, considered here is chapter 6 and the advection of tracers associated with the Kelvin waves such as moisture to ensure that their structure is not distorted by the numerical scheme as it is the case here for the central scheme.

We will extend this study by considering a background shear including both a barotropic and a first baroclinic background wind in a future work. In this fashion, as shown in the equations (2.32), the different roles of the barotropic and the barotropic components on the equatorial waves can be studied separately. Note that by using shallow water equations of Matsuno (2.31), these effects are considered to be alike. The preliminary results (not shown here) suggest that by including the baroclinic component of the background shear, the Rossby waves become less trapped. This gives consistent results with the ones obtained in Zhang and Webster's [43], who suggested that the less-trapped Rossby waves can modify the energy exchange between the tropics and the midlatitudes. In order to derive a more realistic background shear, we may consider a meridional velocity for the background shear as well. We expect a

mericional velocity to affect the trapping and the features of these equatorial waves. The two phenomena which can be build into the model which have meridional velocity and influence the equatorial waves are the Hardly cell circulation and monsoon circulations.

Bibliography

[1] D. Bale, R. Leveque, S. Mitran, and J. Rossmanith. A wave propagation method for conservation laws and balance laws with spatially varying flux functions. *SIAM J. Sci. Comput. 24*, pages 955–978, 2002.

[2] J. A. Biello and A. J. Majda. The effect of meridional and vertical shear on the interaction of equatorial baroclinic and barotropic rossby waves. *Studies in Applied Mathematics*, 112:341–390, 2004.

[3] J. Dias and O. Pauluis. Convectively coupled waves propagating along an equatorial itcz. *J. Atmos. Sci.*, 66:2237–2255, 2009.

[4] D. R. Durran. *Numerical methods for wave equations in geophysical fluid dynamics*. Springer, New York, 1999.

[5] J. Ferguson, B. Khouider, and M. Namazi. Two-way interactions between equatorially-trapped waves and the barotropic flow. *Chinese Annals of Mathematics, Series B 30:5*, pages 2943–2975, 2009.

[6] D. Frierson, A. Majda, and O. Pauluis. Dynamics of precipitation fronts in the tropical atmosphere. *Comm. Math. Sciences*, 2(4):591–626, 2004.

[7] A. Gill. *Atmosphere-ocean dynamics*. Academic Press, New York, 1982.

[8] I. M. Held and M. J. Suarez. A proposal for the intercomparison of the dynamical cores of atmospheric general circulation models. *Bull. Amer. Meteor. Soc., 75(10)*, pages 1825–1830, 1994.

[9] J. R. Holton. *An Introduction to Dynamic Meteorology*. Academic Press, 2004.

[10] C. Jablonowski and D. L. Williamson. A baroclinic instability test case for atmospheric model dynamical cores. *Quart. J. Roy. Met. Soc.*, pages 2943–2975, 2006.

[11] B. Khouider, A. St Cyr, A. Majda, and J. Tribbia. MJO and convectively coupled waves in a coarse resolution GCM using a simple multicloud parameterization. *J. Atmos. Sci. (submitted)*, 2010.

[12] B. Khouider and A. Majda. A non-oscillatory balanced scheme for an idealized tropical climate model. part I: Algorithm and validation. *Theoretical and Computational Fluid dynamics*, 19:331–354, 2005.

[13] B. Khouider and A. Majda. A non-oscillatory balanced scheme for an idealized tropical climate model. part II: Nonlinear interactions and effects of moisture. *Theoretical and Computational Fluid dynamics*, 19:355–375, 2005.

[14] B. Khouider and A. Majda. Multicloud convective parametrizations with crude vertical structure. *Theor. Comput. Fluid Dyn.*, 20:351–375, 2006.

[15] B. Khouider and A. Majda. A simple multicloud parametrization for convectively coupled tropical waves. part I: Linear analysis. *J. Atmos. Sci.*, 63:1308–1323, 2006.

[16] B. Khouider and A. Majda. A simple multicloud parametrization for convectively coupled tropical waves. part II: Nonlinear simulations. *J. Atmos. Sci.*, 64:381–400, 2007.

[17] B. Khouider and A. Majda. Equatorial convectively coupled waves in a simple multicloud model. *J. Atmos. Sci.*, 65:3376–3397, 2008.

[18] R. Leveque. Balancing source terms and flux gradients in high-order Godunov methods: The quasi-steady wave-propagation algorithm. *J. Comput. Phys. 146*, pages 346–365, 1998.

[19] R. LeVeque. *Finite volume methods for hyperbolic problems*. Cambridge University Press, United Kingdom, 2002.

[20] R. Nairb M. Levya and H. Tufoc. High-order Galerkin methods for scalable global atmospheric models. *Computers and Geosciences*, 33:1022–1035, 2007.

[21] A. Majda. *Introduction to PDEs and Waves for the Atmosphere and Ocean*. American Math Society, 2003.

[22] A. Majda and J. Biello. The nonlinear interaction of barotropic and equatorial baroclinic Rossby waves. *J. Atmos. Sci.*, 60:1809–1821, 2003.

[23] A. Majda and B. Khouider. A numerical strategy for efficient modeling of equatorial waves. *Proc. Nat. Acad. Sci.*, 98(4):1341–1346, 2001.

[24] T. Matsuno. Quasi-geostrophic motions in the equatorial area. *J. Met. Jap.*, 44:25–41, 1966.

[25] J. Molinari, K. Lombardo, and D. Vollaro. Tropical cyclogenesis within an equatorial rossby wave packet. *J. Atmos. Sci.*, 64:1301–1317, 2007.

[26] R. D. Nair and C. Jablonowski. Moving vortices on the sphere: A test case for horizontal advection problems. *Mon. Wea. Rev . 136*, pages 699–711, 2008.

[27] H. Nessyahu and E. Tadmor. Non-oscillatory central differencing for hyperbolic conservation laws. *J. Comput. Phys.*, 87:408–463, 1990.

[28] J. Pedlosky. *Geophysical Fluid Dynamics*. 2nd ed., Springer-Verlag, New York, 1987.

[29] P. Roundy. Analysis of convectively coupled Kelvin waves in the indian ocean MJO. *J. Atmos. Sci.*, 65:1342–1359, 2008.

[30] V. Romano S. F. Liotta and G. Russo. Central scheme for balance laws of relaxation. *SIAM J. Numer. Anal.*, 38(4):1337–1356, 2000.

[31] V. Romano S. Liotta and G. Russo. Central schemes for systems of balance laws. In *Hyperbolic Problems: Theory, Numerics, Applications, Proceedings of the 7th Int'l conference*.

[32] A. St-Cyr, C. Jablonowski, J. M. Dennis, H. M. Tufo, and S. J. Thomas. A comparison of two shallow water models with non-conforming adaptive grids. *Mon. Wea. Rev .136*, pages 1898–1922, 2008.

[33] K. H. Straub and G. N. Kiladis. Extratropical forcing of convectively coupled Kelvin waves during austral winter. *J. Atmos. Sci. 60*, pages 526–543, 2003.

[34] K. H. Straub and G. N. Kiladis. The observed structure of convectively coupled Kelvin waves: Comparison with simple models of coupled wave instability. *J. Atmos. Sci. 60*, pages 1655–1668, 2003.

[35] M. Taylor, J. Tribbia, and M. Iskandarani. The spectral element method for the shallow water equations on the sphere. *Journal of Computational Physics .130*, pages 92–108, 1997.

[36] B. Wang and X. Xie. Low-frequency equatorial waves in vertically sheared zonal flow. part I: Stable waves. *J. Atmos. Sci.*, 53:449–467, 1996.

[37] P. Webster. Response of the tropical atmosphere to local steady forcing. *Mon. Wea. Rev.*, 100:518–541, 1972.

[38] P. Webster. Seasonality of atmospheric response to sea-surface temperature anomalies. *J. Atmos. Sci.*, 39:29–40, 1982.

[39] P. Webster and H. R. Chang. Energy accumulation and emanation regions at low latitudes: Impacts of a zonally varying basic state. *J. Atmos. Sci.*, 45:803–829, 1988.

[40] P. Webster and J. R. Holton. Wave propagation through a zonally varying basic flow: The influences of mid-latitude forcing in the equatorial regions. *J. Atmos. Sci.*, 39:722–733, 1982.

[41] M. Wheeler and G. Kiladis. Convectively coupled equatorial waves: Analysis of clouds and temperature in the wavenumber–frequency domain. *J. Atmos. Sci.*, 56:374–399, 1999.

[42] M. Wheeler, G. N. Kiladis, and P. J. Webster. Large-scale dynamical fields associated with convectively coupled equatorial waves. *J. Atmos. Sci.*, 57:613–640, 2000.

[43] C. Zhang and P. Webster. Effect of zonal flow on equatorially trapped waves. *J. Atmos. Sci*, 46(24):3632–3652, 1989.

[44] C. Zhang and P. Webster. Laterally forced equatorial waves in mean zonal flows. part I: Stationary transient forcing. *J. Atmos. Sci*, 49:585–607, 1992.